Title
Studies of the Cosmos Using Spiderweb Absorber Transition Edge Sensor

Author
Westbrook, Benjamin

Publication Date
2014

Peer reviewed|Thesis/dissertation

Studies of the Cosmos Using Spiderweb Absorber Transition Edge Sensor Bolometers

By

Benjamin G. Westbrook

A dissertation submitted in partial satisfaction of the

requirements for the degree of

Doctor of Philosophy

in

Physics

in the

Graduate Division

of the

University of California, Berkeley

Committee in charge:

Professor Adrian T. Lee, Chair
Professor William Holzapfel
Professor Bernard Sadoulet

Fall 2014

Studies of the Cosmos Using Spiderweb Absorber Transition Edge Sensor Bolometers

Abstract

Studies of the Cosmos Using Spiderweb Absorber Transition Edge Sensor Bolometers

by

Benjamin G. Westbrook

Doctor of Philosophy in Physics

University of California, Berkeley

Professor Adrian T. Lee, Chair

Transition edge sensor (TES) bolometer technology has been at the core of advancements in experimental cosmic microwave background (CMB) science for the past few decades. Theoretical and experimental work has built a robust model of the universe. Despite tremendous progress, there are several key pieces of experimental evidence missing to complete our understanding of the universe. This dissertation covers the work done by Benjamin Grey Westbrook at the University of California Berkeley between 2007 and 2014. It is centered around the use of spider-web absorber transition edge sensor (SWATES) bolometers to study the cosmos by the Atcama Pathfinder Experiment - Sunyaev Zel'dolvich (APEX-SZ) and the E and B Experiment (EBEX). Both of which help complete our model of the universe in complimentary ways.

APEX-SZ is a ground-based experiment that made observations of galaxy clusters via the Sunyaev-Zel'dovich Effect from the Chajnantor Plateau in Northern Chile from 2005 to 2010. It observed galaxy clusters at 150 GHz with 300 SWATES detectors with a resolution of $\sim 1'$. Galaxy clusters are the largest gravitationally bound objects in the present day universe and are excellent for studying the properties of the universe. The primary goal of APEX-SZ was to understand the complex physics of galaxy clusters. By understanding their composition, number density, and evolution we can better our understanding of the evolution of the universe into its present state.

EBEX is a balloon-borne experiment that made observations of the CMB and cosmic foreground during a science flight from the Long Duration Balloon (LDB) facility outside of McMurdo Station, Antarctica over the 2012-2013 austral summer. It made observations of 6000 square degrees of sky using 872, 436, and 256 SWATES bolometers at 150, 250, and 410 GHz detectors (respectively) with $\sim 8'$ resolution

over the course of a 12 day science flight. It's scientific goals include the measurement of B-mode polarization pattern of the CMB over the range of angular scales required to study cosmic inflation and the distortion of CMB polarization by gravitational wells. In additionm it's high frequency bands and sub-orbital platform were engineered to study the polarization of dust in the cosmic foreground. Analysis of the EBEX dataset is ongoing and initial results are presented in the conclusion of this thesis.

Dedications

This thesis is dedicated to all of the people who have helped me throughout my life. I feel lucky to have had so many opportunities and to achieve what I have.

Victoria: My fiancée (and soon to be wife), Victoria, has been by my side through the thick and thin of my Ph,D. studies. Having her by my side has made the process bearable during the times when I felt over worked and stressed. Her constant and ongoing support has been essential to the completion of this thesis. I love you baby!

Family: You have always been there for me. I would not be in this position, without the guidance of my parents Duff and Susie. You raised me to be a responsible, caring, and ever-curious person. I also am happy that Cecily and Lee have become part of my family and am thankful for their love and support. My big brother Zac has provided me with an ever-changing role model of what it takes to be a good citizen and even better person. My family has always provided me with their undying acceptance of every pursuit I have followed.

Friends: Throughout my 11 years in the Bay Area, I have met extraordinary people who have provided me with a solid foundation to launch my career from. These friends have steadfastly provided me with distraction and good times when I needed it most. Nate, you have been there since the beginning. Mike and Ben thanks for all of the wild times and reminding me on how to keep life fun and interesting. I have particularly fond memories of being a 'beer man' with Punit and Stephen and as first year graduate student at UC Berkeley.

You all have helped me earn this Ph,D and I have a tremendous depth of gratitdude.

This one is for all of us!

Acknowledgements

The work in this thesis would not been possible without the professional and academic support of so many. I have done my best to acknowledge all of those that have played a part in my growth as a scientist and I apologize for not being able to include everyone in this acknowledgement.

Professors: I would like to begin by thanking my high school physics teacher, Dr. John Suding, for sparking my interest in pursuing physics. The physics class I took senior year in high school has stuck with me for over a decade. I would like to thank Professor Thomas B$'$ottger for turning my dreams of becoming a physicist a reality. Without his close guidance, friendship, and mentorship as an undergraduate advisor at USF, my career would have taken a different direction. I will always be grateful for my time at USF.

Dr. Adrian Lee has been my academic advisor from the time I started at Berkeley. Under his guidance, I have grown into the confident, capable, and competent scientist that I am today. I have countless memories of Adrian offering his full support of my pursuits and am very thankful to have had him as my advisor. Adrian has shown me what it takes to be both a compentent scientist and good human being through his ever optimistic outlook and hard work. Additionally, I would like to thank Dr. Shaul Hanany, Dr. Matt Dobbs, and Dr. Amber Miller for their steadfast leadership of the EBEX project and their guidance I received throughout the project. My deployment to Antarctica for the EBEX launch will always be a lasting memory for me. I thank all three of you for everything you did to make it a reality. I would also like to acknowledge Dr. Paul Richards and Dr. William Holzapfel for their rolls as additional advisors to my work. Both of them have made countless contributions to the field and I feel honored to have worked under their supervision during such an exciting time for experimental cosmology.

Lab Members: The graduate students, post-docs, and undergrads in the lab at Berkeley have been invaluable to my education. So much of what I have learned has come directly from the many talented students and post-docs in the group. Much of my expertise is a direct result of the many training sessions, academic discussions, and impromptu conversations in the office. I would like to thank Dan Schwan, Jared Mehl, and Martin Lueker for providing me with my first experience of being a real scientist while preparing for and deploying to Chile for APEX-SZ observations. In addition to this, I would like to give particular thanks to Kam Arnold, Erik Shirokoff, Xiaofan Meng, and Aritoki Suzuki for the guidance and training I received in micro-fabrication.

I also want to thank the other students, many of whom I did not directly work with, for creating a positive office environment and making day to day life pleasant as a graduate student. Bryan Steinbach, Liz George, Nicholas Harrington, Erin Qualy,

Mike Meyers, and Zigmund Kermish all helped me along my journey.

Collaborators: There are also many graduate students, post-docs, and professors outside of UC Berkeley who have been instrumental to the completion of my Ph,D. work. Amy Bender and James Kennedy were excellent co-workers and mentors during my first years as a graduate student. Their guidance during my deployments to Chile provided the foundation for the rest of my academic career. Professors Nils Halverson and Cathy Horellou also played a central role in my growth as a scientist.

There are countless people within the EBEX collaboration who deserve recognition as my thesis would not have been possible without their hard work and dedication. I worked most closely with the "bolo monkeys" (Kate Raach, Kevin MacDermid, and François Aubin) and we have nothing but the fondest memories of tuning bolometers and participating in fabrication feed back telephone calls. There are many others as well, Chappy, Joy, Seth, and Michelle, from Columbia all commandeering the gondola for EBEX during flight and were especially fun to deploy to Antarctica with. Thanks to the others at University of Minnesota, Asad Aboobaker, Jeff Klein, Kyle Zillic, Chaoyun Bao, Michael Milligan, and Bikram Chandra for working so hard on EBEX. Finally, thanks to Gregory Tucker, Andrei Korotkov, and Kyle Helson from Brown.

Agencies and Others: In addition to my direct collaborators I would like to thank the crew of the APEX observatory who helped us with our observations year in and year out. I have many memories of the Sequitor control room where I worked all three shifts (baker, regular, and prostitute). The successful flight by EBEX would not have been possible without the support of the talented crew at the Columbia Space Science Balloon Facility who helped with the multiple experiment integrations at Palestine, TX and the official launch in the austral summer of 2012-23. The staff of the Marvell Nanofabrication Facility have always been a valuable support system for the fabrication of the EBEX focal plane.

I acknowledge the monetary support for the APEX-SZ and EBEX projects: National Science Foundation grants AST-0138348 & AST-0709497 and LBNL grant DE-AC02-05CH11231 APEX-SZ and NASA detector development grants (NNG06GJ08G).

This work is a quintessential example of 'standing on the shoulders of giants.'

Contents

List of Figures

List of Tables

Chapter 1

Introduction

Cosmology is the study of the universe from its first moments of existence to its present day form and beyond. We can learn a tremendous amount about our past and future by observing and measuring the properties of the vast array of objects and structures of the universe. For the past three decades, cosmologists have made tremendous advances in our understanding of the cosmos through studies of the Cosmic Microwave Background (CMB), supernovae (SN), large scale structure (LSS) of the universe, and many other fields of research [2, 5, 63]. Characterization of the CMB is especially advanced due to the hard work of many different collaborations including full sky surveys done by Wilkinson Anisotropy Probe (WMAP) and PLANCK [5, 32], balloon-borne telescope missions [36, 40, 44, 71], and ground based observations [4, 8, 74, 77, 82]. Careful analysis of experimental data and theoretical models led to the development of ΛCDM (Dark Energy, Cold Dark Matter) Cosmology, which is currently the leading model for our universe. This model describes an isotropic and homogeneous universe composed of roughly ∼70% Dark Energy, ∼25% Dark Matter, and ∼5% baryonic ('ordinary') matter that is approximately 13.7 billion years old which underwent a rapid expansion during its first moments of existence [2, 5, 45, 63].

Development and refinement of ΛCDM cosmology requires studying a widely varying group of cosmological objects which emit light over the entire electromagnetic spectrum. The CMB is of particular interest to cosmology as it provides an image of the very young universe and contains relics created at even earlier times [27, 45]. For the past decade the use of transition-edge sensor (TES) bolometers has become the preferred method of characterizing the CMB due to their excellent noise performance and the ability to fabricate thousands of them on single silicon wafers in a micro-fabrication facility.

This dissertation focuses on the use of particular type of TES bolometer called a Spiderweb Absorber Transition Edge Sensor (SATES) Bolometer deployed by the APEX-SZ and EBEX experiments [71, 77, 89]. The work presented in this thesis is outlined as follows:

– Chapter 1: An overview of the scientific motivation for the work in this thesis.

Chapter 2: An introduction and review of bolometers and their suitability for studying the Cosmic Microwave Background and cosmic foreground.
- Chapter 3: An overview of the fabrication of Spiderweb Absorber Transition Edge Sensors used by the APEX-SZ and EBEX experiments.
- Chapter 4: An overview of APEX-SZ Experiment.
- Chapter 5: An overview of EBEX Experiment.
- Chapter 6: An overview of the EBEX data set and initial data analysis.
- Chapter 7: An appendix providing more details on several sub-topics.

1.1 A Brief History of the Universe

It is useful to give an overview of the history of the universe as that history explains the origin of the cosmological objects we wish to study. Table 1.1 outlines the several of the major epochs and events in the universe's history.

Table 1.1: A brief summary of the major epochs in the evolution of the universe.

Epoch	**Time After Big Bang**	**Description**
Big Bang	0	The 'dawn of time'
Grand Unification	$\sim 10^{-34}$ s	Grand Unification of Forces [13], some particles come into existence
Inflation	$\sim 10^{-34}$-10^{-32} s	Inflation occurs, rapid expansion of space-time, universe cools rapidly [45]
Baryogenisis (Quark, Hadron, Lepton Epochs)	∼1-10 s	First Baryons are created [52]. Matter/anti-matter symmetry breaks [46]. Particles continue to evolve and decay into their present day abundances.
Photon Epoch	∼10s-3.8e5 yrs	Photons dominate the energy of the universe. Temperatures exceed the binding energy of hydrogen. The charged baryons are tightly coupled to the photons in a primordial plasma [42].
Recombination	∼3.8e5 yrs	The universe cools to ∼3000K, allowing electrons and protons to recombine and form neutral hydrogen, decoupling the baryons from the photons, which continue to free stream through the rest of the universe's history [14, 91].

Matter Dominated Epoch	∼3.8e5 yrs-8.0e9 yrs	Matter dominates the energy density of the universe. Large Scale Structure (LSS) begins to form via non-linear growth of initial density perturbations [56].
Modern Day Universe	∼8e9 yrs-13.8e9	LSS continues to evolve. Dark energy begins to overtake matter as the dominate form of energy in the universe [56]. Expansion rate of universe begins to acceleration [63].

1.1.1 Overview of the Mathematical Framework for Cosmology

The FRW metric, which is the mathematical framework of cosmology, is a set of General Relativity equations which describe the space-time of the universe in terms of a parameter called the scale factor. The scale factor describes the relative growth (and/or contraction) of a characteristic length a time, t, to the same length at some other time t_0 due to changes in the space-time metric. Starting with Einstein's field equations and making the assumptions that space-time is homogeneous and isotropic one arrives at the Friedmann equations; two differential equations that describe how the scale factor evolves as a function of the energy density in the universe and time [19]. The Friedmann Equations are given in Equation 1.1.

$$\left(\frac{\dot{a}}{a}\right)^2 = \frac{8\pi G}{3}\rho(t) - \frac{kc^2}{a^2} + \frac{\Lambda}{3} \tag{1.1a}$$

$$\left(\frac{\ddot{a}}{a}\right)^2 = \frac{-4\pi G}{3}\left[\rho(t) + \frac{3p(t)}{c^2}\right] + \frac{\Lambda}{3} \tag{1.1b}$$

In the above equations, $\rho(t)$ is the energy density of the universe as a function of time (which can be split into multiple components like matter and radiation), $p(t)$ is the pressure from each of the components of the universe as a function of time, Λ is a parameter which describes dark energy (an energy with a negative pressure), k describes the curvature of the space, and c and G are the speed of light and Newton's gravitational constant, respectively. The first Friedmann equation can be re-written in a form that only depends on time, and present day values of energy density and is shown in Equation 1.2.

$$\left(\frac{\dot{a}}{a}\right)^2 = \left(\frac{H}{H_0}\right)^2 = \Omega_\Lambda + \Omega_\mathrm{k} a^{-2} + \Omega_\mathrm{m} a^{-3} + \Omega_\mathrm{r} a^{-4} \tag{1.2}$$

In the above equation, each of the Ω_i factors represents the ratio of given type of energy density to the present day critical density of the universe. That is $\Omega_i \equiv \rho_{\rm i}/\rho_{\rm crit}$.[1] The critical density, $\rho_{\rm crit}$, is 'critical' because it describes an unstable equilibrium point (i.e. a critical point) between an open-geometry universe a closed-geometry universe. If the total density exceeds the critical density, the Friedmann equations describes space-time as having positive (closed) curvature and will ultimately have enough gravitational energy to pull all of the matter in the universe back to a single point, sometimes called a 'Big Crunch.' If the total density is less than the critical density, space will have negative (open) curvature and will expand (and continue to expand at faster and faster rates) until the universe is so spread out that nothing can be in causal contact with anything else, which is often called a 'Big Rip.' The third possibility is that the total density is exactly equal to the critical density. In this case, space-time will be described as having flat curvature and will not undergo a Big Crunch or a Big Rip. In this scenario, the universe will asymptotically approach a finite size and remain as so for the remainder of the universe's existence. An interesting feature of the curvature of space time as described by the Friedmann equations is that if the universe is closed/open/flat at any given point in time, it must remain so for the life of the universe. Thus, a closed/positive universe can never become either a open/negative or flat spaced universe.

The density parameters in Equation 1.2 are labeled k, m, r, and Λ which correspond to curvature, matter (including dark matter), radiation, and dark energy densities, respectively. When the all of the Ω's are summed, it equals the total energy density of the universe divided by the critical density. By construct, we require the sum of all Ω's be equal to one by including a curvature energy density Ω_k. A non-zero value of Ω_k implies a departure from a flat universe. If we set a=1 for present day, and using this construction Equation 1.1b becomes Equation 1.3.

$$\Omega_{\rm m} + \Omega_{\rm r} + \Omega_\Lambda = 1 - \Omega_{\rm k} \tag{1.3}$$

As Equations 1.2 and 1.3 suggest, a measurement of the present day curvature and relative energy densities of the components of the universe will predict the evolution of the scale factor over time. Current data suggests that the scale factor, a, growing and accelerating with time, implying that the universe will eventually be dominated by Dark Energy (Ω_Λ) [63].

1.2 Inflation

Cosmic inflation, or simply inflation, is a powerful theory that compliments the Big Bang Model of the universe and completes the ΛCDM cosmological model. Gener-

[1]The present day critical density is approximately 1 hydrogen atom per cubic meter. The scale factor, a, is chosen to be equal to unity at t=0 (present day) and becomes smaller as one moves back in time ($t < 0$) when the universe was smaller.

ically speaking, inflation refers to a period of rapid expansion (factor of $\geq 10^{28}$ in radius) of the very early universe ($\text{age}_{\text{universe}} < 10^{-32}$ s). Inflation provides a single explanation to four outstanding 'problems' with a simple Big Bang Model: the flatness problem, the horizon problem, the magnetic monopole problem, and the origin of Large Scale Structure.

In standard Big Bang cosmology, the universe started out in a hot dense state and then expanded over time into what we call the modern universe. The Big Bang model (combined with the Standard Model of particle physics) is very successful and accurately predicts/describes many of the most fundamental things about our universe including light element abundance (H, He, and Li), matter/anti-matter asymmetry, the Hubble Flow, and the existence of the CMB. The standard Big Bang model requires an additional 'event' to explain why the present day universe is geometrically flat, isothermal on scales of the observable universe, void of magnetic monopoles, and full of complex large scale structure.

1.2.1 The Flatness Problem

Many studies of the temperature anisotropies of the CMB have concluded that the universe we live in is very nearly flat [5, 32]. The reason that this is considered a problem, is that a flat universe is an unstable equilibrium point of the Friedmann equations. Due to the nature of the equations, this result tells us that the universe has been (very nearly) flat for most of its existence. If at about $t_{\text{universe}} = 1$ ns the universe's curvature deviated from flat by just 1 part in 10^{24} it would have significantly deviated from flat today as shown in Figure 1.1. There are two possible explanations: the universe was simply fined tuned to be flat and that is just the way it is or the universe was made to appear flat through some other mechanism. The latter option is more attractive as it does not require anything to be 'fine tuned' to a perfectly flat value, but rather relies on a mechanism (e.g. inflation) to drive the curvature of the universe towards zero curvature.

Inflation solves the flatness problem in the following way. It allows the universe to have any curvature before inflation occurs. During inflation the expansion is so immense that it stretches space so much that curvature is no longer detectable to an observer in the modern day universe. A useful analogy comes from considering the surface of a balloon with an infinite expansion capacity. When the balloon is only inflated to a radius of a ~ 1 m the curvature of the surface is clearly detectable to the naked eye. However, if the radius of the balloon was expanded by a factor 10^{68} we would only be able to observe a small fraction of the surface of the balloon and its radius of curvature would be come so big that it was would be *undetectable* despite the fact that the balloon has a non-zero global curvature. This means that regardless of initial shape (closed, like a balloon or open like a saddle), the flatness on the scale of the observable universe will be very nearly equal to one. Additionally, after

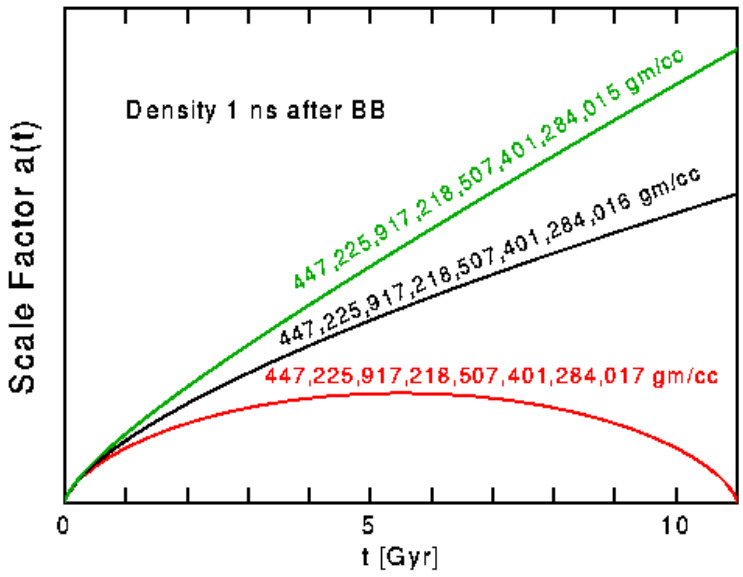

Figure 1.1: A plot illustrating the 'fine tuning' problem with observing a flat universe in the present day. If the density of the universe were to deviate from flat by just 1 part in 10^{24} 1 ns after the big bang, the curvature of the present day universe would have deviated significantly from a flat geometry, which would be in direct tension with experimental data.

inflation occurs, the universe can remain at the unstable equilibrium long enough for the universe to evolve into its present state.

1.2.2 The Horizon Problem

The existence of the Cosmic Microwave Background (CMB) is a prediction of the Big Bang model. The CMB is cold bath of photon; a leftover relic of the primordial universe's fluid state. One of its most remarkable attributes is its isotropy and homogeneity; on scales of 300 Mpc or greater the universe appears to be the same in all directions and that it has the same temperature everywhere.

We know that the universe is ∼13.8 billion years old and that the CMB was emitted when it was about 400 thousand years old. At the surface of last scattering, CMB photons could only interact with other CMB photons that were within 400 thousand light years of one another. As a consequence, we should only expect thermal equilibrium on this size scale and smaller. However, the CMB has a red-shift of ∼1100, which allows one to compute the size of the universe at this redshift. The observable universe has a radius of 13.8 billion light years. At the surface of last scattering, the size of the universe will be a factor of $\sim 1/z$ smaller (∼13.8 million

light years)[2].

The mismatch between the size of the universe and the size of the causal horizon at the surface of last scattering is a problem for the Big Bang model of the universe. If this model were correct, the universe would need at least 13.8 million years to come into thermal equilibrium at the time of last scattering, but it only had 380,00 years. Simply stated, photons on opposite sides of the causal horizon do not have sufficient time to come into thermal equilibrium. There are two explanations for this: this is an unlikely random coincidence, or the CMB (on scales of the size of the observable universe) started in, and has always been in thermal equilibrium.

Inflation solves this problem, by allowing for the super-luminal expansion of space time. The theory states that before inflation begins, the universe could have started in any, random, non-homogeneous, non-isotropic state. Any given 'patch' within a radius of the speed of light times the age of the universe has enough time to thermally equilibrate. Inflation then expands space-time super-luminally, which can stretch a very small patch, which was already in thermal equilibrium, to a length scale larger than the observable universe. Since inflation is happening to space itself, it does not disturb the thermal equilibrium of any patch as the entire universe expands. The entire universe may not be uniform and/or isotropic, but contains patches (each of which is larger than our observable universe) that are homogeneous and isotropic.

1.2.3 The Magnetic Monopole Problem

A prediction of the Standard Model of Particle physics is the existence of magnetic monopoles. However, many experiments have failed to find the existence of a single magnetic monopole. In a standard Big Bang model, we would expect a non-zero number of magnetic monopoles in our present day universe. The Big Bang model does accurately describe matter/anti-matter asymmetry, light element abundance (Hydrogen, Helium, and Lithium), and the presence of a Cosmic Neutrino back ground, but does not explain the absence of magnetic monopoles.

Inflation solves the problem of absent monopoles by allowing the generation of magnetic monopoles to occur before the period of inflation when the energy density of the universe was sufficiently high. As the universe expands the production of magnetic monopoles falls off quickly and ends before inflation begins. Thus there is a fixed number of magnetic monopoles created during this period. The number of density of these monopoles falls to 1 per observable universe after the volume of the universe expands by a factor of 10^{28}.

[2]Recall that $a \approx z^{-1}$, for $z >> 1$)

1.2.4 The Origin of Large Scale Structure

Inflation also provides a robust explanation for the origin of the large scale structure (e.g. cosmic filaments, galaxy clusters) in the universe. Quantum perturbations generated during inflation create energy density fluctuations in the very early universe which provides seeds for the growth of large scale structure (cold over-dense regions) and cosmic voids (hot under dense regions).

1.2.5 Slow Roll Inflation

The exact mechanism that drove inflation is poorly understood and is studied extensively by theoretical cosmologists. The simplest class of inflation models refer to 'slow-roll' inflation. These models assert that during inflation there was a quasi-stable scalar inflation field ϕ, which dominated the energy density of the universe. This allows us to re-write one the Friedmann Equations as shown in Equation 1.4.

$$\begin{aligned} H^2 &= \frac{1}{3M_{\rm pl}^2}\Big(\frac{\dot{\phi}^2}{2}V(\phi)\Big) \\ \text{where, } M_{\rm pl} &= \sqrt{1/8\pi G} \end{aligned} \tag{1.4}$$

The quasi-stable nature of the inflation field is shown in Figure 1.2. The field is allowed to move, but does so slowly enough that the approximations in Equation 1.5 are valid. In other words the potential energy of inflation is much larger than its kinetic energy.

$$\ddot{\phi},\ \dot{\phi}^2 = 0 \tag{1.5}$$

When studying slow-roll inflations cosmology typically define two inflation parameters ϵ and η, which are shown in Equations 1.6 and 1.7.

$$\epsilon = \frac{M_{\rm pl}^2}{2}\Big(\frac{V'(\phi)}{V(\phi)}\Big)^2 \tag{1.6}$$

$$\eta = M_{\rm pl}^2\Big(\frac{V''(\phi)}{V(\phi)}\Big)^2 \tag{1.7}$$

When ϵ, η are $<< 1$, the slow roll conditions are met and Equation 1.4 can be solved to show that the scale factor grows exponentially in a 'slow-roll' scenario: $a(t) \propto e^{Ht}$. In addition providing the mechanism for inflation the slow-roll approximation also provides a solid theoretical frame work to understand perturbations introduced by quantum fluctuations in the early universe, which are discussed in

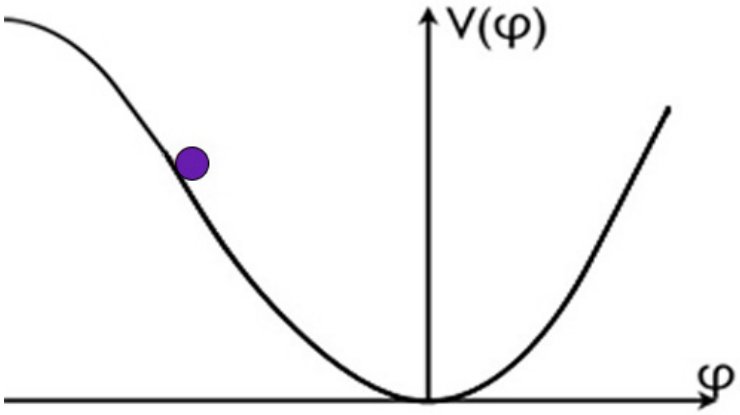

Figure 1.2: A schematic drawing of the potential of a slow-roll inflationary field. During inflation the field sat at a local, meta-stable equilibrium point. Eventually the field falls out of the false ground state by slowly-rolling to the true ground state point. While sitting in the meta-stable state this field has a negative pressure, which drives inflation. When it falls into the true vacuum state it releases a tremendous amount of energy by decaying into all of the particles we observe today.

greater detail below. The spectrum of perturbations is typically given as a power law like in Equation 1.8.

$$\begin{aligned} P_{\text{scalar}} &= P\text{s}, \text{k}^* \frac{k}{k^*}^{n_\text{s}} \\ P_{\text{tensor}} &= P\text{t}, \text{k}^* \frac{k}{k^*}^{n_\text{t}} \\ \text{Slow Roll: } n_\text{s} &= 1 + (2\eta - 6\epsilon) \end{aligned} \tag{1.8}$$

A generic prediction of slow-roll inflation is a non-zero, but small deviation from a flat spectrum (i.e. $n_\text{s} < 1$), which has been measured to be ∼5% smaller than 1 [5].

1.3 Cosmic Microwave Background

The Cosmic Microwave Background (CMB) provides an image of what the universe looked like just ∼380,000 (z∼1100) years after the big bang. At that time, the universe was about 3000K and was nearly homogeneous. However several effects due to the physics of the early universe introduce small variations in the temperature and polarization of the CMB. For example, oscillations of the primordial plasma

create temperature anisotropies and quantum fluctuations embedded in space-time by inflation create polarization anisotropies in the CMB. The scale, magnitude, and statistical properties of these fluctuations contain a wealth of information about the early universe. Measuring these fluctuations is an experimental challenge because the present day CMB has been red-shifted to 2.725 K and the anisotropies exist at a $1{:}10^5$ and $1{:}10^7$ for temperature and polarization anisotropies respectively. This means that the signals we are attempting to measure are 100s of nK to 10s of μK in magnitude.

1.3.1 Power Spectra

From the point of view of CMB observations, experimentalists can measure 3 basic characteristics of CMB radiation: its frequency spectrum (intensity as function of Frequency $I(\nu) \sim f(\nu)$), its temperature at a given location ($T(\hat{n})$) and its polarization at given location ($P(\hat{n})$). Most of modern CMB science is predicated on studying the deviations from perfect isotropy and homogeneity across the sky. We implement a power-spectrum analysis of the data in order to understand how these deviations are distributed across the sky. The magnitude and angular scale of these deviations depends directly on the initial conditions of the universe and provides a powerful probe of the very early universe.

Frequency Spectrum

The frequency spectrum of the CMB was first measured by Penzias and Wilson at Bell labs in the 1960s [62]. FIRAS on the COBE satellite followed up on these measurements and found that the CMB is almost a perfect blackbody as shown in Figure 1.3 [22]. This data is averaged over the full sky and does not contain any information about the spatial distribution of CMB temperature. However, we expect to see tiny deviations from a perfect black body from inflation (and experimental evidence) so it becomes necessary to measure the temperature and polarization of the CMB at each point on the celestial sphere (or some fraction thereof).[3]

Temperature and Polarization Maps

For typical CMB experiments the temperature and/or polarization is mapped at each point on the sky ($\hat{n} \equiv f(\theta, \phi)$). Since we are generally interested in deviations of temperatures from the nearly uniform background, it is common to report the temperature/polarization deviations as a function of location on the sky (e.g. for temperature $\Theta(\hat{n}) = (T(\hat{n}) - \langle T \rangle)/\langle T \rangle$).

A map of the entire sky from the PLANCK Collaboration is shown in Figure 1.4. Each pixel in the map represents an absolute value of temperature. The average value of the map is 2.725K and the deviations (anisotropies) are about 200μK in

[3] $\hat{n}$ is a vector denoting a unique pointing direction (ϕ, θ) on the sky.

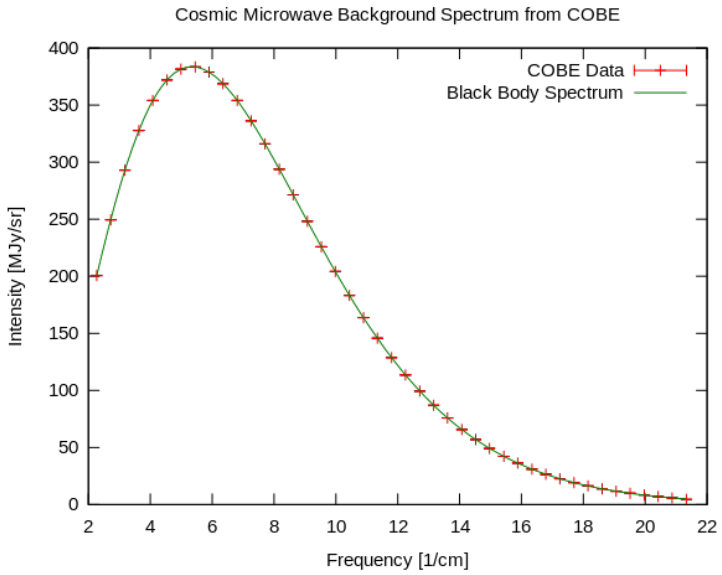

Figure 1.3: A spectral measurement of CMB radiation from the FIRAS instrument mounted on the COBE satellite. The data match the theoretical spectra of a perfect PLANCK body at 2.725K to exquisite precision.

amplitude.

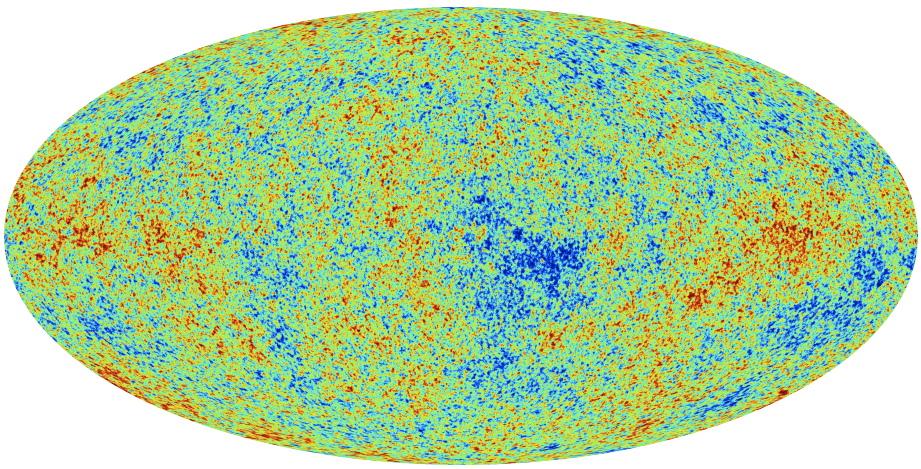

Figure 1.4: A temperature map of the entire sky from the PLANCK Collaboration. The map noise in the map is 6 μK_{CMB} at 143 GHz with a resolution of $7'$.

Since the data are mapped onto a 2D projection of the celestial sphere (as shown

in Figure 1.4), it is a natural choice to decompose the resulting sky map into a set of orthogonal spherical harmonics (Equation 1.9):

$$Y_{\ell m} = \sqrt{\frac{2\ell+1}{4\pi}\frac{(\ell-m)!}{(\ell+m)!}} P_\ell^m(cos\theta)e^{im\phi} \tag{1.9}$$

where P_ℓ^m are the Legendre Polynomials and $0 < \ell < \infty$ and $-\ell < m < \ell$. Thus for each point on the sky we can rewrite the temperature deviation ($\Theta(\hat{n})$) as as the weighted sum of all spherical harmonics as shown in Equation 1.10.

$$\Theta(\hat{n}) = \sum_{\ell=0}^{\ell=\infty} \sum_{m=-\ell}^{\ell} a_{\ell m} Y_{\ell m}(\hat{n}) \tag{1.10}$$

where,

$$a_{\ell m} = \int_{\theta=-\pi}^{\pi} \int_{\phi=0}^{2\pi} \Theta(\hat{n}) Y_{\ell m}^*(\hat{n}) d\Omega \tag{1.11}$$

This 2D map can be converted into a *power spectrum* of the fluctuations ($\Theta(\hat{n})$) as the inner product of the spherical harmonics coefficient as shown in Equation 1.12.

$$\langle a_{\ell m} a^*_{\ell' m'} \rangle = \delta_{\ell\ell'}\delta_{mm'} C_\ell \tag{1.12}$$

which can be re-written with C_l on the left hand side as shown in 1.13.

$$C_\ell = \frac{1}{2\ell+1} \sum \langle |a_{\ell m}|^2 \rangle \tag{1.13}$$

In practice however, we want to express the physical map of temperatures on the sky, $\Theta(\hat{n})$, as a power spectrum of multipole moments. Expressing temperature anisotropies in this manner, tells us information about the angular scales which have the most and least amount of correlation. To do this we express the correlation of two points on the sky as function of C_ℓ as shown in Equation 1.14

$$\psi_{\Theta\Theta} = \langle \Theta(\hat{n})\Theta(\hat{n}') \rangle = \frac{1}{4\pi} \sum_{\ell=0}^{\infty} (2\ell+1) C_\ell P_\ell cos\theta \tag{1.14}$$

where $cos\theta = \hat{n} \cdot \hat{n}$. Equation 1.14 relates a well defined observable, the correlations of temperature on two points of the sky, with a power spectrum coefficient C_ℓ. Thus we can estimate the power spectrum of any on-sky observable distribution in terms of its weighted angular power, C_ℓ. Each value of C_ℓ is proportional

to a Legendre polynomial of order ℓ, which fixes its angular scale on the sky (e.g. $\ell = 2 \sim 180^\circ$ and $\ell = 3 \sim 120^\circ$). **The magnitude of C_ℓ tells us how much correlation there is of an observable at given angular scale on the sky. By comparing the angular scales that have the most (least) correlation, we can understand the physics of the mechanism that originally created the anisotropies.**

Cosmic Variance

Care must be taken when using Equations 1.12, 1.13, and 1.14 because they are statistical averages over ensembles of spherical harmonics. However, given a multipole moment ℓ, there are only (m $= 2\ell + 1$) modes, which puts a fundamental statistical limit on our ability to estimate any given C_ℓ. This limit is given as $\Delta C_\ell = \sqrt{\frac{2}{2\ell+1}}$. In other words we can only sample as many modes are available to us, a limitation is referred to as 'sample' or 'cosmic' variance. In the case of the monopole ($\ell = 0$), we can sample only a single mode! For sufficiently high-ℓ values sample variance is not a dominate source of error when estimating a power spectrum.

1.3.2 Temperature Anisotropies

The temperature of the CMB has been measured to exquisite precision over a wide range of angular scales by many different experiments. By applying a power spectrum analysis to the temperature we understand in great detail how the temperature anisotropies are distributed across the sky. Figure 1.5 is a plot of the measured C_ℓ's from data compared to model of the primordial plasma seeded by quantum perturbations during inflation.

The power spectrum shown in Figure 1.5 has many features which are well studied by the cosmology community. For simplicity, this work thesis only discusses the acoustic peaks to illustrate how the location of those peaks directly probe the very early universe and secondary anisotropies introduced by the Sunyaev-Zel'dolvich Effect.

Acoustic Peaks of the Temperature Power Spectrum

Recalling that the amplitude of the C_ℓ's in Figure 1.5 represent the amount of temperature correlation we expect at a given angular scale (i.e. multipole moment ℓ), we are quickly drawn to the excess of power at $\ell \sim 100$ (or 2°). This peak is often referred to as the first acoustic peak as it created by the acoustic oscillation of the primordial plasma. The initial perturbations created by inflation are expected to be nearly scale invariant. That is, there is no preferred 'size' (angular extent) of these perturbations, which would suggest that the temperature power spectrum of the CMB be nearly flat. However, the evolution of these perturbations in the primordial plasma gives rise to the acoustic peaks we observe today. Taking the power spectrum

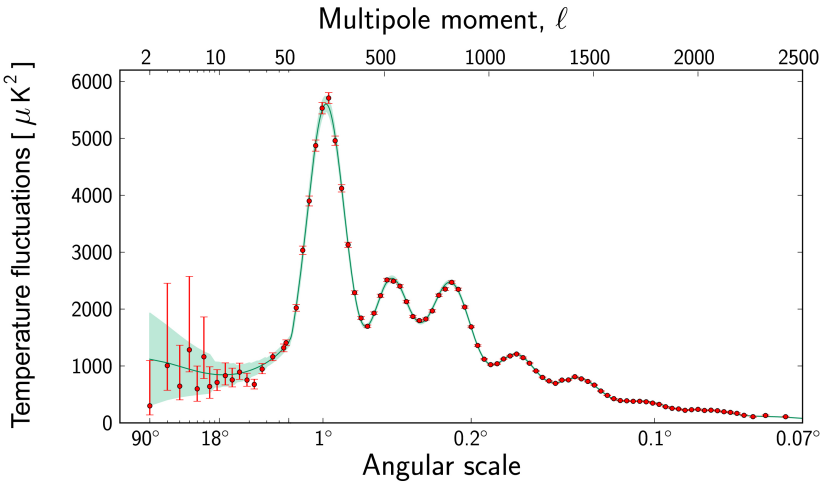

Figure 1.5: A temperature difference power spectrum for the entire sky from the PLANCK Collaboration. The data from Figure 1.4 are converted into the red points shown in the plot. The green line is a to the data by a six parameter model. The amplitude of the C_ℓ's are estimated within a histogram-bin of ℓ-values to decrease sample variance, which is indicated by the green band most visible below $\ell \sim 50$.

at face value we see that this evolution caused the temperature correlations to peak at 2° up until the surface of last scattering.

Simple physical arguments about the primordial plasma (tightly coupled photons and baryons) explain how this happens. If we consider some perturbation with a given physical size (i.e. one of the modes of the initial perturbation), we would observe regularly spaced cold over-dense regions in between hot, under-dense regions. However the very early universe still obeys basic physics (i.e. gravity and a ideal gas pressure). Cold over-dense regions will begin to collapse in to even colder and denser regions under the influence of gravity. As the over-dense region collapses it will begin to heat up as the gas begins to virialize. Eventually the pressure inside of this over dense region will increase beyond the negative pressure from gravity causing the region to expand (and cool again), setting up the basic mechanism for acoustic oscillations. Over-dense regions collapse and heat up, while under-dense regions expand and cool. However, if we invoke the surface of last scattering at an arbitrary time we may 'catch' or 'freeze' the perturbation in a random phase, meaning it may be at maximum expansion, maximum compression, or somewhere in between.

At the surface of last scattering we see a snapshot of one these oscillations at

a pseudo-random phase. The reason we call it a pseudo-random phase is that we know the surface of last scattering occurred about 400,000 years after the big bang. Therefore, means we know exactly how much time these perturbations had to evolved before they were 'cemented' in the CMB at the surface of last scattering. However, the period of these oscillations depends on their characteristic size, which is distributed almost uniformly. We expect these phases of each mode at the surface of last scattering to by pseudo-randomly distributed. For the peak at 2°, we can deduce that this particular perturbation mode was at the peak of its evolution during its first oscillation at the time that CMB photons began to free stream. Conversely, we can deduce that the first through represents a perturbation mode that was able to evolve to its peak (once) and back to its minimum before (once) CMB photons started to free stream. These peaks are said to be the result of Baryonic Acoustic Oscillation (BAO). We don't see any peaks larger than 2 degrees (below $\ell \sim 100$), because these modes were larger than the acoustical horizon and did not have time to evolve. The amplitude of subsequent peaks is expected to be damped out by diffusion of hot regions into cold regions, which is a stronger effect at smaller and smaller scales through a process known as Silk Damping [20].

Secondary Anisotropies and the Sunyaev-Zel'dolvich Effect

The CMB photons must travel through most of the observable universe before they are detected by our telescopes. Although the cross-section is low, the CMB photons can be altered by interactions with intervening matter. The interaction of CMB photons with galaxy clusters is particularly interesting because it provides a unique probe of both the CMB and galaxy clusters themselves. When CMB photons pass through galaxy clusters, about 1% of the photons will inverse-Compton scatter off the hot electrons trapped in the core of the gravitational well of the cluster. This is called the Sunyaev-Zel'dolvich Effect [80]. This scattering will distort the spectral shape of the CMB since about 1% of the photons are scattered to a higher frequency and will create a detectable 'deficit' of photons at the location of the cluster at 150 GHz. This will also cause a slight shift in the temperature power spectrum of the CMB as it introduces a tiny cold spot at the location of each cluster and thus effects the correlation between points on the map. However, the effect on the power spectrum is limited to small angular scales (high-ℓ) due to the typical angular extent of galaxy clusters [23, 69].

1.3.3 Polarization Anisotropies

A quadrupole distribution of hot and cold spots centered on an electron will polarize CMB photons via Thompson Scattering. Thompson scattering of CMB photons by a single electrons from two orthogonal directions is shown in Figure 1.6.

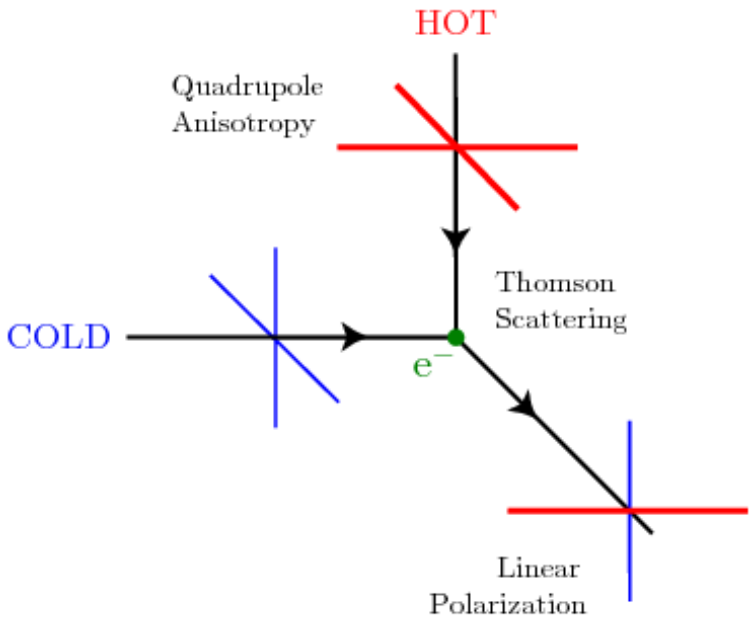

Figure 1.6: A diagram explaining how quadrapole anisotropies induced by inflation in the primordial plasma can polarize CMB photons. If we consider a cold spot shining on an electron from the left (blue) and a hot photon shining on a electron from the top (red) we see that the scattered light will have a net polarization. The electric field from the cold spot will cause the electron to vibrate in the vertical direction and re-radiate polarized light along that direction (i.e. Thompson Scattering). Similarly the electric field of the photons coming form the hot spot will cause the electron to vibrate left and right causing to re-radiate polarized light that is orthogonal to the polarized light coming from the cold spot. Since there is more intensity coming from the hot spot than the cold spot the scattered radiation will be partially polarized. The polarization fraction of CMB anisotropies is expected to be 1-10%.

This means that any quadrapole temperature anisotropies present at the time of the surface of last scattering will produce a linear polarization at the location of the anisotropy. The linear polarization we actually observe will depend on the orientation of the quadrupole relative to the line of sight. **Thus if we measure the linear polarization of each point on the sky $P(\hat{n})$ we are mapping a projection of the quadrupole anisotropies on the celestial sphere.** Furthermore, since these quadrupole anisotropies are distributed across the sky we expect that the sky will contain a specific polarization pattern or signature. This signature depends strongly on the physical mechanisms that created the anisotropies. Quadrupole anisotropies

can be produced by three basic types of perturbations to the space-time metric: scalar, vorticity, and tensor, which are discussed in more detail below.

E and B Modes

The polarization of the CMB is a vector field with $P(\hat{n})$ a magnitude and orientation at each location on the sky. This vector field can be decomposed into two orthogonal modes that we usually refer to as E-modes and B-modes. They are distinguished by their behavior under the divergence and curl operators on the field. E-modes are curl-less ($\nabla X E = 0$) while the B-mode are divergence-less ($\nabla \dot{B} = 0$), which is analogous to electric (E) and magnetic (B) fields in electro-magnetism.

In addition to the clean mathematical separation of these components, there is a physically meaningful reason to study these modes separately since the three types of perturbations (scalar, vector, tensor) all probe different physics. Although each of these perturbations can create an quadrupole and thus induce linear polarization at the time of last scattering, we expect a negligible contribution to the CMB's polarization from vector perturbations, because they are predicted to be highly suppressed by inflation [45].

Scalar Perturbation Produce Only E-Modes

Due to the symmetric nature of scalar perturbations, they can only create an E-mode polarization pattern on the sky when viewed from an observatory like earth. When we look for polarization created by scalar perturbations we are looking for azimuthally symmetric perturbations like the one shown in Figure 1.7

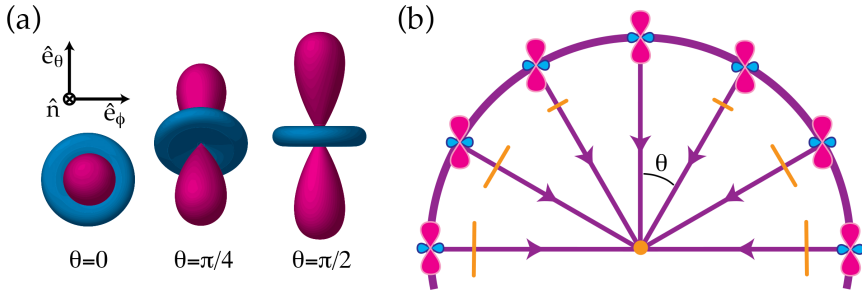

Figure 1.7: A scalar perturbation creating a symmetric quadrapole anisotropy that would polarize the light along the direction of the cold (red) lobes. The polarization we detect from this anisotropy depends on the orientation of the cold lobes relative the line of sight, BUT NOT the azimuthal orientation of the anisotropy. This means that any polarization observed from this type of anisotropy will be either exactly perpendicular or parallel to the line of sight implying that this pattern is rotationally symmetric (i.e. is an E-mode).

Tensor Perturbations Produce Both E and B-Modes

Due to the asymmetric nature, tensor perturbations will produce both E and B-mode polarization pattern on the sky. A rotation of a tensor perturbation in azimuth can change the orientation of the incoming radiation. If these perturbations are distributed randomly across the sky, we expect that roughly half of the time they will have E-mode orientation and the other half of the time the would have a B-mode orientation, which does not have rotational symmetry. **Gravity waves produced by inflation will induce tensor perturbations into the space-time metric and are the only known source of primordial B-mode polarization in the CMB. Therefore measurement of primordial B-modes is direct experimental evidence for inflation.**

E to B Mode Mixing

In the previous sections we discussed how primordial perturbations create E and B mode patterns on the sky. However, there is a secondary effect that changes what polarization pattern we actually measure here on earth. CMB photons must traverse the universe before being absorbed and sensed by our detectors. It is predicted (and measured) that the gravitational lensing of CMB photons can mix E modes into B-modes, which will peak at the angular scale that has the greatest ability to gravitational lens the CMB photons.

1.3.4 E-mode Polarization Power Spectra

Up to this point we have established how the presence of quadrupole anisotropies (both azimuthally symmetric/asymmetric) at the surface of last scattering produce E and B mode polarization patterns on the sky. Since the polarization of the CMB is an observable at each point on the sky we can compute its auto-correlated polarization power spectra just like we did for temperature data. The amplitude and location of any peaks in this power spectrum are direct measures of the physics of the early universe which created these polarization inducing anisotropies.

We know that quantum energy fluctuations, which are amplified by inflation, create a field of scalar perturbations across the sky. We also know that these same scalar perturbations provide the initial conditions for BAO, which implies that the Temperature and E-mode power spectrum should be closely related (since they are sourced by the same physical mechanism). The E-mode power spectrum has been measured by many experiments and it turns out that these two power spectrum are almost perfectly anti-correlated with temperature as shown in Figure 1.8, which is expected from theory.

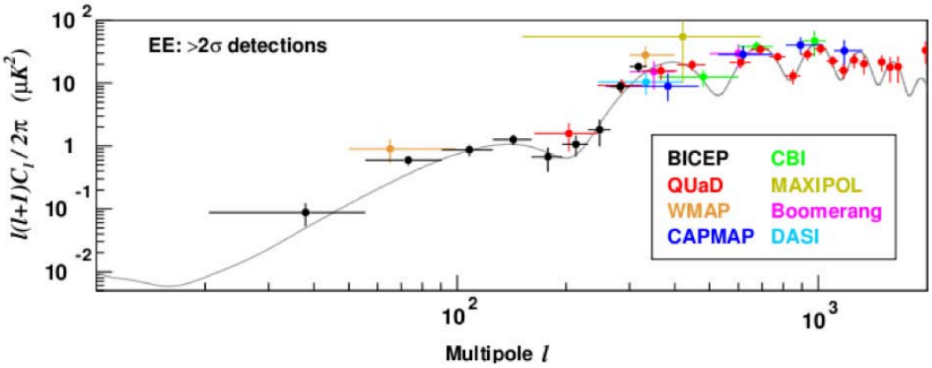

Figure 1.8: Measurements of the EE power spectrum by 8 different experiment (colors) showing excellent agreement with the theory (gray solid line). The peaks and troughs are anti-correlated with the TT peaks and troughs since quadrapole anisotropies created by density perturbations peak and trough when then temperature correlations are at a minimum and maximum respectively.

1.3.5 B-mode Polarization Power Spectra

There are only two mechanisms which produce B-mode polarization in the CMB: gravity waves produced by inflation and gravitational lensing of B-mode by intervening large scale structure. These two effects can also be detected independently since we expect them to peak at different angular scales on the sky.

B-modes at Small Angular Scales

B-mode polarization produced by the lensing of E-modes will peak at angular scales which have the largest amount of gravitational lensing ability. Massive galaxy clusters and cosmic filaments provide the structure required to lens these modes and are typically a few arc minutes in size when viewed form earth. **As such we expect the B-mode signature from gravitational lensing to peak at angular scale similar to the large scale structure of the universe, which is about 2-5′.** Measurement of B-mode polarization at these angular scales effectively maps the distribution of matter along the line of sight over the celestial sphere allowing for the computation of a matter power spectrum. The shape of this matter power spectrum as function of scale provides an experimental probe of the sum of the neutrino masses and their hierarchy as shown in Figure 1.9 [1].

B-modes at Large Angular Scales

Gravity waves that were disturbing space-time at the surface of last scattering will also have a characteristic peak in the power spectrum, but at much larger an-

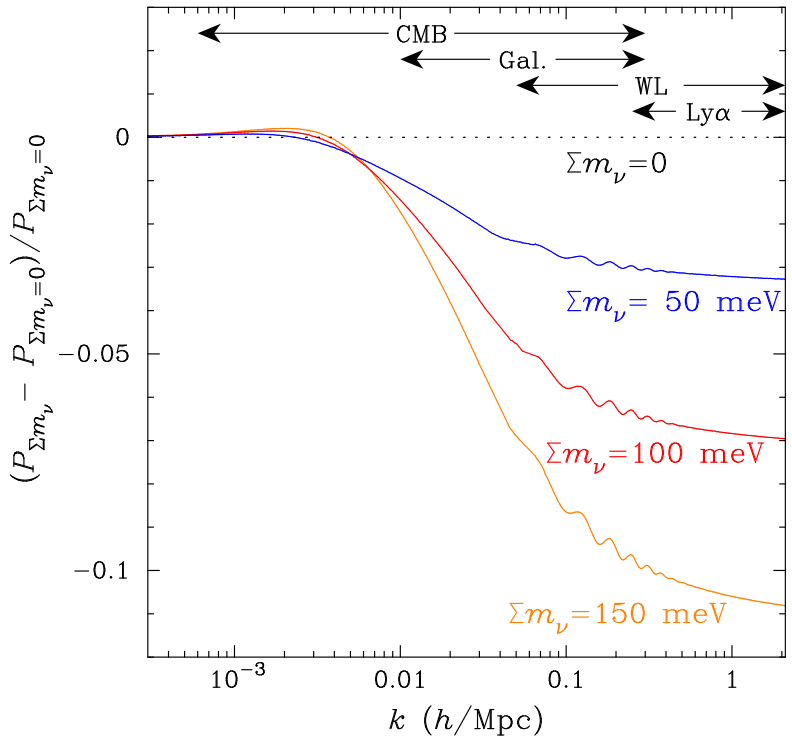

Figure 1.9: A plot of 3 different theoretical matter power spectra normalized to their value at large scale demonstrating the effect of $\sum m_\nu$ on the growth of structure on small scales (large $\vec{k}$). CMB polarization experiments can measure the power spectrum well enough to constrain $\sum m_\nu$, and will provide even tighter constraints when combined with optical LSS experiments such as DESI [1].

gular scales than those induced by gravitational lensing. Gravity waves will peak at an angular size which corresponds to the size of the casual horizon at the time of recombination. Any quadrupole anisotropies created by gravity waves that are larger than the horizon (at recombination) cannot effect the quadrupole signature and will be suppressed in a power spectrum. The gravity waves which produce quadrapole that are much smaller than the horizon will be suppressed by the interaction with the ionized plasma. Thus gravitational modes equal in size to the horizon at recombination will contribute most strongly to the quadrupole anisotropies in the CMB. The overall amplitude of this B-mode signature depends directly on the energy scale of inflation. We parameterize the amplitude with the tensor-to-scalar ratio, which is the amplitude of tenser perturbations compared to scalar perturbations at a given scale (k_0). The relationship between r and the energy scale of inflation is given by

Equation 1.15.

$$r \equiv \frac{P_{\text{tensor}}(k_0)}{P_{\text{scalar}}(k_0)} = 0.008\big(\frac{E_{\text{inflation}}}{10^{16}\text{GeV}}\big)^4 \tag{1.15}$$

We also expect another peak in the B-mode power spectrum at very large angular scales that were created when the universe re-ionized (z $\sim$ 6). This peak corresponds to the larger primordial gravitational waves which have entered the causal horizon at z$\approx$6 and interacted with the newly ionized plasma. The salient features of the B-mode power spectrum are summarized in Figure 1.10.

1.4 State of the Field

Cosmologists have made significant progress in measuring temperature and polarization of the CMB to the precision required to build an accurate model of our universe. The temperature power spectrum has been measured to exquisite precision putting tight constraints on this cosmological model [5, 17, 23]. The first measurements of high-ℓ B-mode signatures were reported by the POLARBEAR and SPTpol experiments [83, 31], and a tantalizing signal measured at the angular scales corresponding to primordial B-modes was published by BICEP2 earlier this year [4]. There is now a strong need to follow up on these results to improve their constraining power on cosmological models and verify their findings.

1.4.1 CMB Temperature Data

The temperature of the CMB has been mapped by over 20 experiments since the 1990s. As of 2014, a plethora of collaborations have published results from these datasets, which have provided constraints on our model of the universe. In particular, all-sky maps made by WMAP and PLANCK (satellites) and high-angular resolution maps made by SPT and ACT (ground-based observatories) provide especially tight constraints.

Combining these data sets allows for a single model to be fit all the way out to the 9th peak on the silk damping tail as shown in Figure 1.11. This model is fit with 6 free parameters ($\Omega_{\text{b}}h^2$ (baryon density fraction), $\Omega_{\text{cdm}}h^2$ (cold dark matter density fraction), $100\theta_{\text{MC}}$ (100 times a physical pivot point), τ (optical depth), n_{s} (spectral index of scalar perturbations), $ln(10^{10}A_s)$ (log power of primordial curvature perturbations), which are used to calculate many others (Ω_Λ (dark energy density frication)), Ω_{matter} (matter density fraction), H_0 (present day value of the Hubble Parameter). CMB temperature data alone provides insight into the most fundamental characteristics of our universe and the nature of inflation as shown in Figure 1.12.

Temperature data constrains the energy content of the universe, the rate of expansion of the universe, and its spatial curvature. In addition, it can constrain inflation

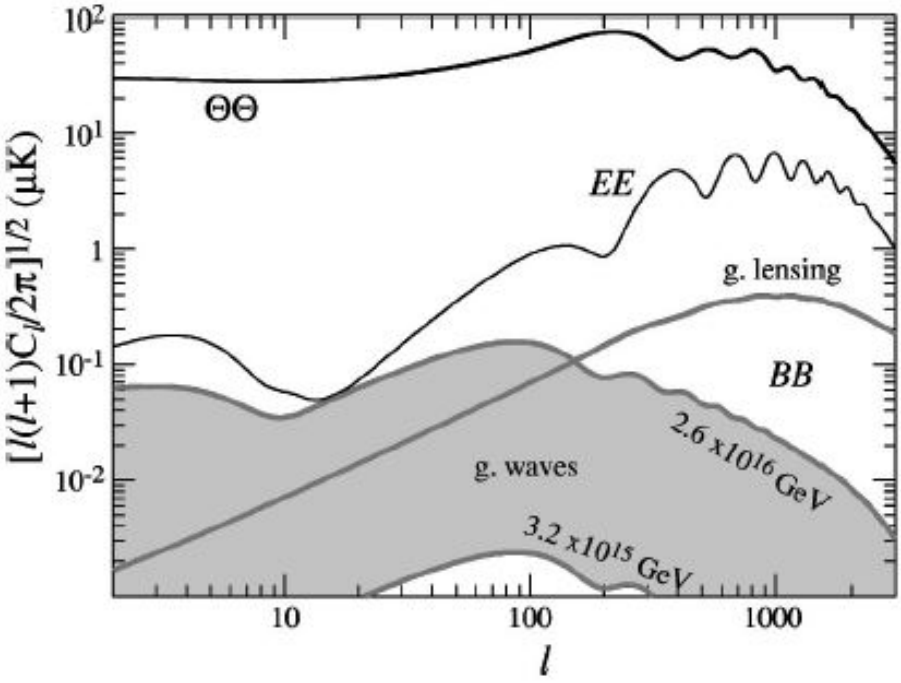

Figure 1.10: Theoretical curves for the temperature (ΘΘ), E-mode (EE), and B-mode (BB) power spectra on a single plot. There are two contributions to the BB power spectrum: those generated during inflation at large angular scales and those created by the lensing of E-mode photons by intervening matter and small angular scales. The amplitude of the B-mode signature from lensing is well predicted from our knowledge of the CMB and the large scale structure of the universe and is only plotted at a single amplitude. The amplitude of the B-mode signature from primordial gravitational waves is unknown and is indicated by the gray band. The shape of the signature is well understood, but its amplitude depends (or determines once measured) the energy scale of inflation. An additional bump in both the EE and BB spectra is seen at $\ell \approx 4$, which is known as the reionization bump.

models through the accurate characterization of the spectral index n_s. Table 1.2 summarizes a subset of the parameters determined from these measurements. A plot showing the parameters spaced ruled out by the PLANCK Collaboration for various inflation models is shown in Figure 1.12.

Cosmological Parameters of ΛCDM from Temperature Data

The data in Figure 1.11 are fit with 6 free parameters to form the black line. The value of the best fit parameters are used to compute a variety of other properties of

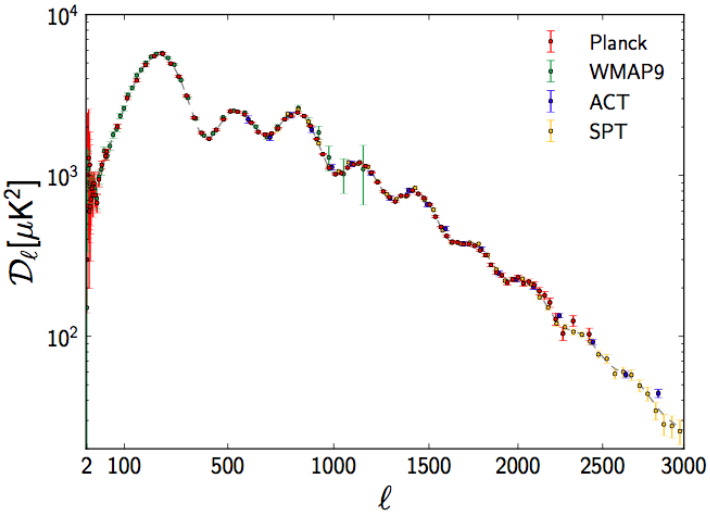

Figure 1.11: Temperature power spectrum with a joint fit to 4 data sets from the PLANCK, WMAP, SPT, and ACT collaborations that cover the full-sky (PLANCK + WMAP) and small angular scales (SPT + ACT) constraining the model fit (dashed gray line) to exquisite precision.

the universe. Once of the most notable parameters is the spectral index of the scalar perturbation power spectrum. A deviation from 1 is strong evidence for inflation which is supported with high precision by temperature data to be $n_s = 9603 \pm 0.0073$. A contour plot in $r - n_s$ including the implications for various inflation models is shown in Figure 1.12

1.4.2 POLARBEAR and SPTpol Measure high-ℓ B-modes

SPTpol first published a result showing a 7.7σ correlation between B-mode polarization induced by lensing and the Cosmic Infrared Background (CIB) [31]. POLARBEAR quickly followed by publishing an auto-correlated detection of B-mode polarization at high angular scales [83]. These measurements provide a robust measure of the mass distribution of cold dark matter and galaxies along the line of sight of the observation from CMB polarization data. Both results are consistent with one another and represent the first measurement of B-mode CMB polarization reported to the community. Figure 1.13 shows the power spectrum reported by the POLARBEAR collaboration.

These high-ℓ B-mode data provide the first detections of non-zero CMB B-mode polarization, but do not yet have the sensitivity to measure the sum of the neutrino masses more precisely than neutrino oscillation experiments. However, follow up on

	PLANCK		PLANCK + Lensing		PLANCK + WP	
Parameter	Best Fit	68% Confidence	Best Fit	68% Confidence	Best Fit	68% Confidence
$\Omega_b h^2$	0.022068	0.02207 ± 0.00033	0.022242	0.02217 ± 0.00033	0.022032	0.02205 ± 0.00028
$\Omega_{cdm} h^2$	0.12029	0.1196 ± 0.0031	0.11805	0.1186 ± 0.0031	0.12038	0.1199 ± 0.0027
$\Omega_{matter,tot}$	0.3175	0.314 ± 0.020	0.3036	0.307 ± 0.019	0.3183	$0.315^{+0.016}_{-0.018}$
Ω_Λ	0.6825	0.686 ± 0.020	0.6964	0.693 ± 0.019	0.6817	$0.685^{+0.018}_{-0.016}$
n_s	0.9624	0.9616 ± 0.0094	0.9675	0.9635 ± 0.0094	0.9619	0.9603 ± 0.0073
H_0	67.11	67.4 ± 1.4	68.14	67.9 ± 1.5	67.04	67.3 ± 1.2
σ_8	0.8344	0.834 ± 0.027	0.8285	0.823 ± 0.018	0.8347	0.829 ± 0.012

Table 1.2: A summary of a subset of cosmological parameters reported by the PLANCK Collaboration in 2013.

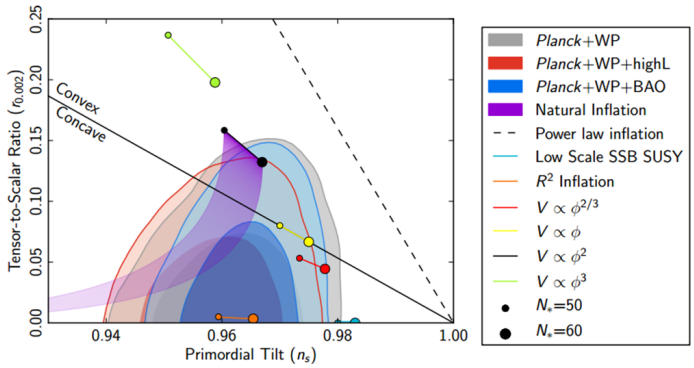

Fig. 1. Marginalized joint 68% and 95% CL regions for n_s and $r_{0.002}$ from *Planck* in combination with other data sets compared to the theoretical predictions of selected inflationary models.

Figure 1.12: A plot from the 2013 PLANCK 1 year data release showing which cosmological models are constrained by data from the PLANCK Collaboration, Weak Lensing Data, and BAO data. The data suggest that r < 0.11 at 95% confidence and that a slow-roll inflation model is still likely.

these measurements will be improved and will soon measure $\sum m_\nu$.

1.4.3 First Hints of Primordial B-modes from BICEP2

In early 2014, the BICEP2 collaboration published their 150 GHz data which suggest an excess of B-mode power at the exact angular scales where primordial B-modes are expected to peak. A robust analysis of their data indicates that there is no significant bias in their findings. The BICEP2 collaboration reported that the

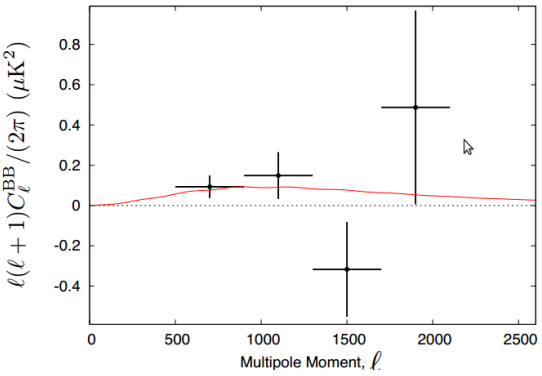

Figure 1.13: A plot the 4 ℓ-bins published by the POLARBEAR collaboration showing an excess of B-mode power at small angular scales.

source of the B-mode polarization was indeed from the primordial gravitational wave background. However, a significant portion of their analysis relies on the accurate modeling of the cosmic foreground in the region of their observations, which was originally chosen because of the low dust intensity at 150 GHz [4, 21, 66]. Figure 1.14 shows the level of B-mode they see in their auto-correlated 150 GHz data with estimates of contributions from the cosmic foreground.

The fits to their data are then used to constrain the value of $r = 0.20 \pm 0.05$, which is summarized in Figure 1.15. A value of $r = 0.2$ was a surprise to many cosmologists as it is in tension with the results from temperature data (see Figure 1.12). Furthermore there was on overall uncertainty in the ability of the BICEP2 collaboration to properly model the cosmic foreground. Thus a series of papers by theorists questioned whether or not the signal could be attributed to dust despite being selected as a low dust region [16, 53]. However, if we can attribute the B-mode polarization in the BICEP2 signal to the CMB, cosmologists have made the first measurements of the B-mode polarization spectrum at both large and small angular scales as shown in Figure 1.16.

1.4.4 Polarization Data at high Galactic Latitudes from PLANCK

In late 2013, the PLANCK collaboration released high galactic latitude polarization data which called the detection of primordial gravitational waves by BICEP2 into question [67]. Prior to the PLANCK Mission, there was very little data on the polarization of dusty cosmic foreground or the emission from synchrotron radiation. As such experimentalists rely on intensity data from experiments like PLANCK, WMAP, and COBE, to find so-called 'quiet regions' of the sky [21, 65, 66]. The mechanisms for polarizing the dust in the cosmic foreground are poorly understood and rely on a variety or processes such spinning dust grains trapped in magnetic

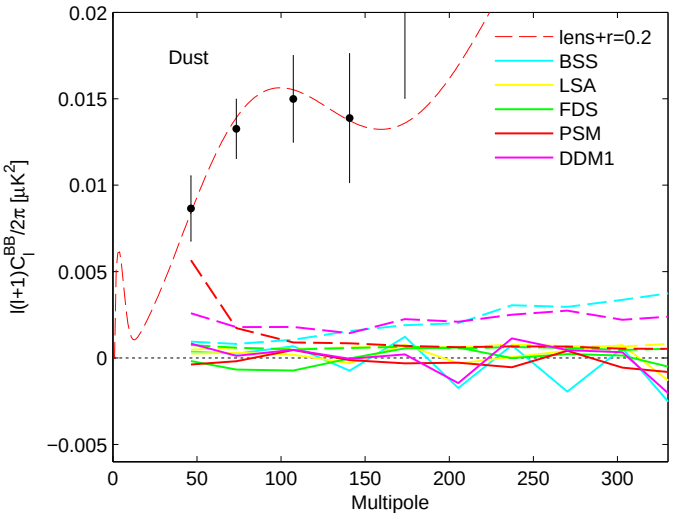

Figure 1.14: A plot from the 2013 BICEP2 paper with a detection showing the detection of a B-mode hump at $\ell \approx 90$ and the estimated levels of polarization contribution from dust using 5 different models. Unfortunately the error on these models is not reported in this figure, which means that the BICEP2 result relies on these models being accurate, an assumption called into question by PLANCK Collaboration data in 2014.

fields. For example, the polarization fraction of dusty radiation depends on the size and composition of its dust grains as well as the overall intensity of the emission which is not constant over the entire cosmic foreground [86].

PLANCK's intermediate results release did not contain any dust polarization data for the BICEP2 region, because they did not have the required signal-to-noise at that time. In the fall of 2014, they released the polarization data at high galactic latitudes. This data suggests that a significant amount of B-mode polarization power at 150 GHz can be attributed to polarized dust emission at 343 GHz. Figure 1.17 over plots the level of B-mode polarization at 150 GHz reported by BICEP2 to be due to gravitational waves with the estimated power spectrum at 150 GHz due to polarized dust emission at 343 GHz.

1.5 Summary

Cosmic Microwave Background cosmology is in an exciting state right now. We have mapped the temperature and E-mode polarization of the CMB to exquisite precision and are on the verge of measuring both the B-mode polarization across a wide variety of scales. The tension between the BICEP2 and PLANCK data sets

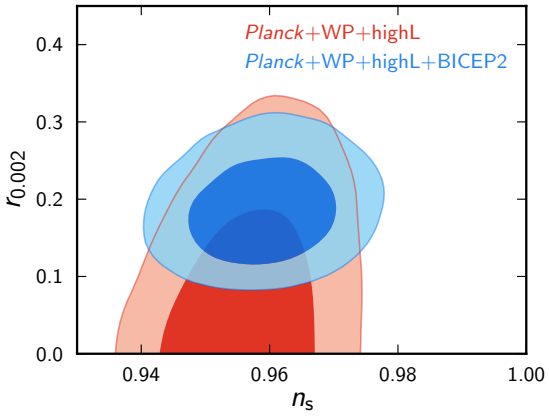

Figure 1.15: A plot from the 2014 BICEP2 paper with a detection of the primordial B-mode polarization constraining the value of r to r = 0.2 ± 0.05. The red contour in this plot is the same as the gray contour in Figure 1.12. The additional BICEP2 significantly improves the constraints. However polarization data from the PLANCK collaboration indicates that the BICEP2 signal may not be entirely due to the primordial gravitational wave background, meaning that the value of r reported by BICEP2 may be artificially high.

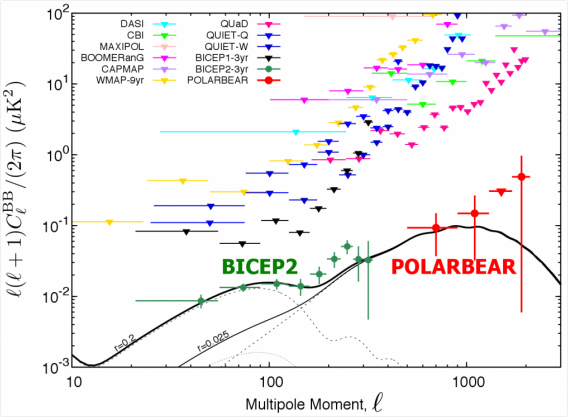

Figure 1.16: The B-mode power spectra data from 12 different experiments. Only BICEP2 has achieved the instrumental sensitivity to measure inflationary B-modes with an amplitude of r=0.2. The POLARBEAR collaboration detected B-modes from gravitational lensing at 97.5% confidence. These initial results are promising but will require rigorous follow up before they can verified.

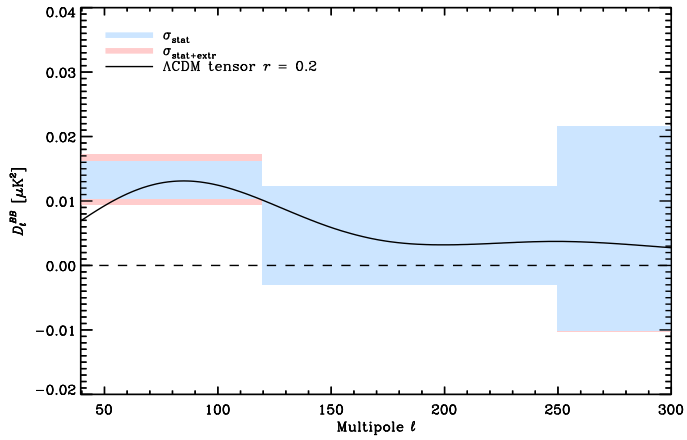

Figure 1.17: The power spectrum reported by the BICEP2 collaboration over-plotted on the estimated signal from polarized dust at 150 GHz as measured by the PLANCK Collaboration.

makes it clear that more work is to be done in understand the polarization of the cosmic foreground which will be essential to recovering the fundamental science from CMB data. In the next few years many experiments will continue to make precision measurements of polarization of the CMB and the Cosmic Foreground. It is likely that the coming decade will unveil the basic nature of inflation and the growth of large scale structure, which has implication for GUT scale physics and physics beyond the standard model.

Chapter 2

Bolometer Theory and General Design Requirements

2.1 Introduction

Most modern CMB experiments make observations of the CMB and other astronomical sources with highly sensitive detectors operated in cryogenic receivers, which are coupled to the cosmos via radio telescopes. There are two leading classes of detectors for observing this region of the electromagnetic spectrum: coherent and direct detectors. Coherent detectors measure and preserve both the phase and amplitude information of an incoming EM wave. The signal is typically down-converted with a stable local-oscillator to some intermediate frequency (IF) before it is amplified and sensed. Modern coherent detectors are quantum-noise limited for frequencies below 100 GHz, but suffer from noise degradation above 100 GHz . They are typically used in interferometry where phase preservation is essential. The other class of detectors, direct detectors, convert the incoming electro-magnetic radiation to heat and generate a signal which is directly proportional to the incident power. Although phase information is lost, these detectors are much more suitable for precision measurements of CMB intensity because of their superior noise performance.

One of the most common types of direct detector is the bolometer. A bolometer senses the incident power from EM radiation by closely monitoring the temperature of an absorbing element, which converts the EM power to heat, with an ultra-sensitive thermometer called a thermistor. The first bolometer was developed by Samuel Langley in 1881 to measure infrared (IR) radiation [41].

Bolometers are widely used in mm/sub-mm applications due to the fact their properties can be tuned to a wide variety of applications and their excellent noise performance. Since their development in the 1990s, voltage-biased transition edge sensor (TES) bolometers have become one of the most popular choices for observations of the CMB [25, 72, 74, 77].

2.2 Theory and Basic Operation of TES Bolometers

A thermistor is an electrically active element whose electrical properties are strong function of temperature (see Section 2.2.1). Transition edge sensor (TES) bolometers

measure temperature fluctuation in the absorber as function of radiation absorbed by the detector by monitoring the resistance of a superconducting film biased between in its superconducting and normal states. A diagram of a TES bolometer is shown in Figure 2.1. The thermistor is voltage-biased with electrical power to measure fluctuations in optical power coming from the sky. The entire structure is isolated on a thermal island at some temperature $T_{\rm detector}$ via a weak thermal link, G_0, above a thermal bath temperature $T_{\rm bath}$.

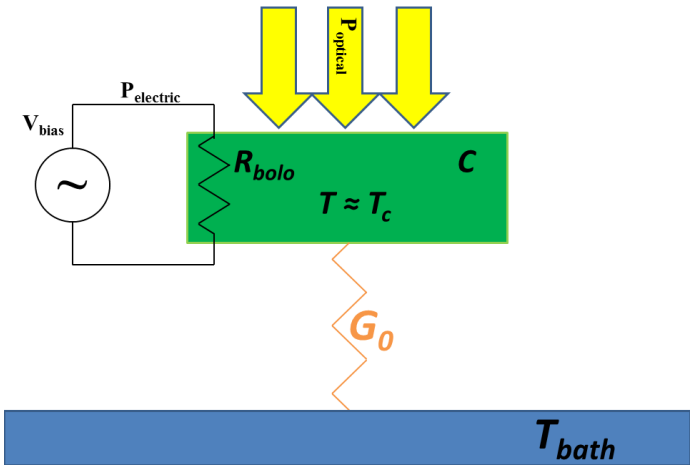

Figure 2.1: A cartoon diagram of a voltage-biased TES bolometer, which illustrates the physical location of the bolometer's intrinsic properties G_0, $T_{\rm c}$, $T_{\rm bath}$, $R_{\rm bolo}$, and $C_{\rm bolo}$. In CMB experiments, optical power is coupled to the absorbing element via a telescope and cold optics in the same cryostat which cools the bolometer. As the optical power fluctuates, the resistance of the TES changes, which manifests as fluctuation in current through the bolometer at constant voltage bias. The power is then dissipated to the bath with some characteristic time constant $\tau_0 = C/G$.

2.2.1 TES as a Thermistor

Early CMB experiments used carbon resistors and doped semi-conductors (e.g. Neutron Transmutation Doped (NTD) Germanium) to construct thermistors. Thermistors made with these materials have a strongly temperature dependent resistance at cryogenic temperatures [29], which allows them to be effective thermistors. TESs take advantage of the strong dependence of resistance as function of temperature

near the superconducting transitions of metal films[1]. Figure 2.2 compares resistance versus temperature plots for an NTD bolometer and an Aluminum-Titanium bilayer. In addition TESs are typically operated at lower temperatures, which further improves their noise performance.

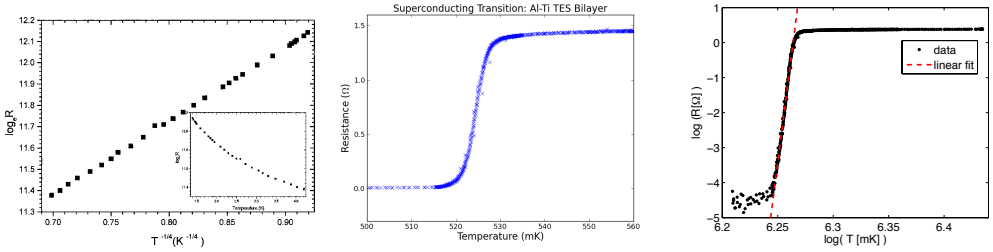

(a) Resistance Vs. Temperature NTD-Ge Thermistor

(b) Resistance Vs. Temperature TES

(c) Alpha for TES

Figure 2.2: Comparison of an NTD and TES Resistance Vs. Temperature curves. **Left:** An example Resistance vs Temperature plot for an NTD-Ge bolometer, which exhibits a exponential dependence on temperature. It is important to note that resistance *increases* with decreased temperature and the thermistor is operated at ∼2.5 K. **Middle:** Resistance vs Temperature for an Al-Ti superconducting bilayer. A clear transition to the super conducting state is seen at T = 525 mK, which occurs over a $\Delta T \approx 7$ mK. **Right:** This panel shows log(R) vs log(T) with a linear log-log best fit to the data indicate a value of $\alpha \approx 250$.

2.2.2 Review of Basic Operation

TES bolometers are first cooled in a cryostat to a temperature just above their transition temperature (typically ∼700-800 mKfor the TES materials used in this work). An AC voltage bias is applied to the TES which will begin to dissipate power through the thermal link G_0 to the thermal bath in a process called 'over-biasing.' It is consider 'over-biasing' because the initial electrical power supplied by the over-bias voltage is larger than the saturation power (see section 2.5.2). The bolometers are then cooled well below their superconducting transition temperature. However, due the high electrical (i.e 'over') bias power and the thermal isolation of the TES, the TES temperature stays at/near its T_c, which is typically 1.5 to 2 times the bath temperature. The voltage biased is slowly dropped until the TES starts to cool allowing it to enter its superconducting transition in a process known as bolometer biasing (sometimes called tuning), which is illustrated in Figure 2.3. The bolometers

[1]The sharpness of the temperature dependence is quantified with the log derivative of the resistance with respect to temperature $\alpha = dln(R(T))/dlnT = (T/R)\frac{dR}{dT}$

are typically biased to a resistance that is about 75% of its normal resistance when the TES temperature is above its T_c. Changes in resistance manifest as fluctuations in current under a constant voltage bias.

2.3 Mathematical Model of Bolometer Behavior

In order to mathematically model the behavior of a bolometer in operation, it is helpful to consider the operation of the bolometer from the perspective of power conservation. In a steady state, the power deposited on the bolometer by the sky and the constant voltage bias will be equal to the power dissipated through the weak thermal link shown in Equation 2.1.

$$P_{\text{total}} = P_{\text{optical}} + P_{\text{elec}}(T) = P_{\text{optical}} + \frac{V_{\text{bias}}^2}{R(T)} = G_0(T - T_{\text{bath}}) \tag{2.1}$$

If we take the derivative of Equation 2.1 with respect to temperature (the optical power is constant with respect to bolometer temperature) we see that the total power on the bolometer exhibits a negative feedback: $dP/dT \propto -P$. If we examine Figure 2.2(b) and Equation 2.1 this makes perfect physical sense. If the optical power on the bolometer increases the bolometer is driven out of the superconducting transition which increases its resistance which is inversely proportional to electrical power. Thus any increase in optical power is compensated with a decrease in electrical power (and vice-versa). Thus, the bolometer can be stabilized to its superconducting transition temperature T_c with strong electro-thermal-feedback (ETF) as shown mathematically in Equation 2.2.

$$\frac{dP_{\text{total}}}{dT} = -\frac{V_{\text{bias}}^2}{R^2}\frac{dR}{dT} = -P_{\text{elec}}\frac{1}{T}\frac{T}{R}\frac{dR}{dT} = -\frac{P_{\text{elec}}\alpha}{T} \propto -P_{\text{elec}} \tag{2.2}$$

To complete the model of the bolometer during operation we refer back to Figure 2.1 to consider the power dissipated through the thermal link, G_0. By energy conservation we can equate the power deposited by the voltage bias and any optical power to the power dissipated by the thermal link. The total power that is deposited on the thermally isolated bolometer is then described by the L.H.S. of Equation 2.3 and the total power dissipated by the thermal link is described by the R.H.S.[2]

[2]We assume a power law dependence for the conductance of the thermal link, with $\kappa(T) = \kappa_0 T^n$ and that the link has a cross-sectional area A_{cross} and length l. If there are multiple legs the result can simply me multiplied by the number of legs used.

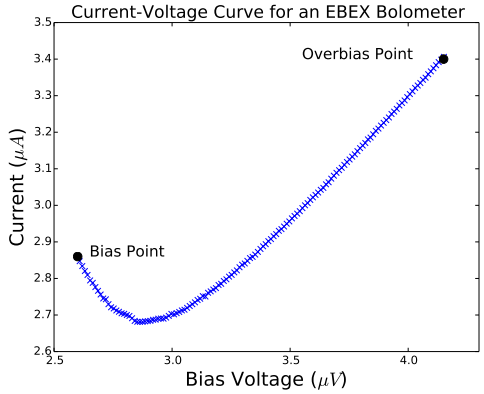

(a) Current Vs. Voltage

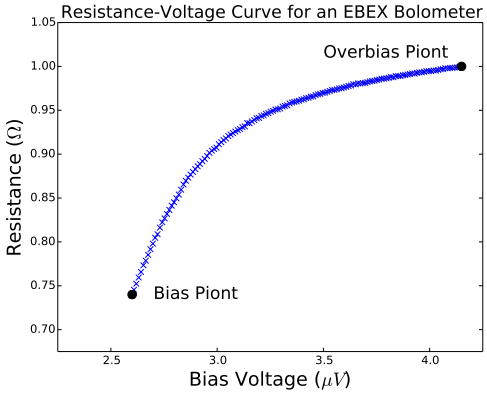

(b) Resistance Vs. Voltage

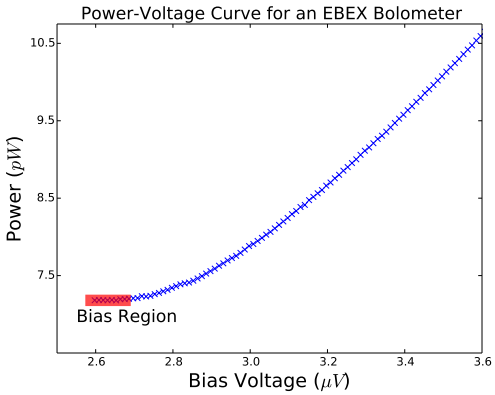

(c) Power Vs. Voltage

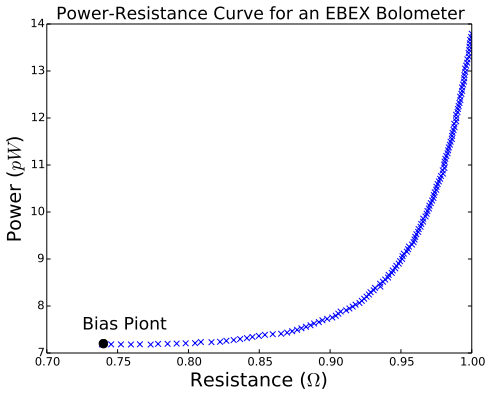

(d) Resistance Vs. Power

Figure 2.3: I-V, R-V, P-V, and R-P curves for a TES bolometer illustrating the bias process. **Upper Left:** A current vs voltage curve taken to bias a detector in its transition. **Upper Right:** A Resistance Vs. Voltage Curve for a TES illustrating using a lower voltage amplitude to bias the bolometer in its superconducting transition. **Bottom Left:** A Power Vs. Voltage Curve. Once the TES enters its superconducting transition the power becomes roughly constant with voltage due to electro-thermal feed back in the TES. **Bottom Right:** A Resistance Vs. Power Curve. This curve shows how the resistance changes as a function of power. When the TES is trapped its superconducting transition the resistance is strong function of power incident on the bolometer. If there is too much power on the bolometer it will become saturated and enter the vertical part of the P-R curve.

$$P_{\text{total}} = P_{\text{elec}} + P_{\text{opt}} \tag{2.3a}$$

$$P_{\text{out}} = \int_{T_{\text{bath}}}^{T_{\text{bolo}}} \frac{A_{\text{cross}}}{l}\kappa(T)dT = \frac{A_{\text{cross}}}{l}\int_{T_{\text{bath}}}^{T_{\text{bolo}}} 33\, k_0 T^n = \frac{\frac{A_{\text{cross}}}{l}k_0}{n+1}[T_{\text{bolo}}^{n+1} - T_{\text{bath}}^{n+1}] \tag{2.3b}$$

$$P_{\text{total}}(T_{\text{bolo}}) = \frac{\frac{A_{\text{cross}}}{l}k_0}{n+1}[T_{\text{bolo}}^{n+1} - T_{\text{bath}}^{n+1}] = G_0(T_{\text{bolo}} - T_{\text{bath}}) \tag{2.3c}$$

Be rearranging Equation 2.1, we find that $T_{\rm bolo} = P_{\rm total}/g + T_{\rm bath}$, where $g = g(T) = dP/dT$, see that the temperature of the detector has a dependence on the total incident power $P_{\rm total}$. In practice the bolometer cannot change its temperature instantly due to the fact that it has a non zero-heat capacity C and it takes some finite amount of time (see Equation 2.4) for the heat to be dissipated through the weak link to the bath, which is simple restatement of Newton's Cooling Law.

$$\tau_0 \equiv \frac{C}{g} \tag{2.4a}$$

In order to calculate the bolometer's response to changes in optical power it is useful to consider a time-varying perturbation to the optical power, $\delta P e^{i\omega t}$, which varies with time at some frequency ω and couples to the TES causing a perturbation in the temperature $\delta T e^{i\omega t}$. Note this requires that $\delta T e^{i\omega t} << T_b$, which is an excellent approximation for most experiments. We can treat fluctuations occurring at different frequencies independently from one another so we can model a single frequency and superimpose the results [43].

$$P = P_{\rm opt} + \delta P e^{i\omega t} \tag{2.5a}$$
$$T = T_{\rm c} + \delta T e^{i\omega t} \tag{2.5b}$$

Plugging the above equations into Equation 2.1 we get a equation describe the power flow through the bolometer where the left hand side describe fluctuations in the power entering and the right hand side describes the power leaving the bolometer. By conservation of energy the two must be equal.

$$P + \delta P_{\rm opt} e^{i\omega t} - \frac{P_{\rm elec}\alpha}{T_c}\delta T e^{i\omega t} = G(T_c - T_b) + (g + i\omega C)\delta T e^{i\omega t} \tag{2.6a}$$
$$P + e^{i\omega t}(\delta P_{\rm opt}) = G(T_{\rm c} - T_{\rm b}) + e^{i\omega t}(\delta T(\frac{P_{\rm elec}\alpha}{T_c} + g + i\omega C)) \tag{2.6b}$$
$$P = G(T_c - T_b) \;\; [Static] \tag{2.6c}$$
$$\delta P_{\rm opt} = \delta T(\frac{P_{\rm elec}\alpha}{T_{\rm c}} + g + i\omega C)) \;\; [Time - Varying] \tag{2.6d}$$
$$\delta P_{\rm opt} - \delta T(\frac{P_{\rm elec}\alpha}{T_{\rm c}}) = \delta T(g + i\omega C) \tag{2.6e}$$
$$\delta P = \delta P_{\rm opt} + \delta P_{\rm elec} = (g + i\omega C)\delta T \text{ , where } \delta P_{\rm elec} = -\delta T(\frac{P_{\rm elec}\alpha}{T_{\rm c}}) \tag{2.6f}$$

We define the loop gain of this amplifier with Equation 2.7.

$$\mathscr{L}(\omega) = -\frac{\delta P_{\rm elec}}{\delta P} = \frac{P_{\rm elec}\alpha}{gT_{\rm c}(1+i\omega\tau_0)} = \frac{\mathscr{L}}{(1+i\omega\tau_0)} \tag{2.7}$$

Examining equations 2.6 and 2.7 reveals that this model is analogous to an amplifier for a purely electrical circuit with feedback where the output is δP and the feedback term is $\delta P_{\rm elec} = -\frac{P_{\rm elec}\alpha}{T_{\rm C}}\delta T$.

We define one last parameter S_I, called responsivity, to quantify the bolometers change in current as a function of change in optical power.

$$S_I = -\frac{dI_{\rm elec}}{dP_{\rm opt}} = \frac{1}{V_{\rm bias}}\frac{dP_{\rm elec}}{dP_{\rm opt}} \tag{2.8a}$$

$$= \frac{1}{V_{\rm bias}}\frac{\frac{-P_{\rm elec}}{T_{\rm c}}\delta T}{(\frac{P_{\rm elec}\alpha}{T_{\rm c}} + g + i\omega C)\delta T} \tag{2.8b}$$

$$= -\frac{1}{V_{\rm bias}}\frac{\mathscr{L}}{(\mathscr{L}+1)}\frac{1}{(1+\omega\tau_{\rm eff})}\text{ , where } \tau_{\rm eff} = \frac{\tau_0}{(\mathscr{L}+1)} \tag{2.8c}$$

In the limit of very high loop gain, $\mathscr{L} >> 1$, the two right most terms simply to unity and the responsivity simply becomes Equation 2.9.

$$S_I = -\frac{1}{V_{\rm bias}} \tag{2.9}$$

Loop gains of 5-50 are routinely achieved by CMB experiments when operating their TES detectors. The high loop gain combined with the negative feedback provided by the TES leads to a bolometer responsivity that is independent of the intrinsic characteristics of bolometer like C and G, which aids in the fabrication of bolometers arrays with high uniformity. Now that we have a model for the bolometer behavior while it is in operation we must model the optical loading on the bolometer to complete the design process.

2.4 Optical Loading

The bolometers presented in this thesis are designed to measure fluctuations in the polarization and intensity of the radiation from the CMB and the cosmic foreground. This radiation is coupled through a radio telescope, an optical chain composed of mirrors, filters, and lenses to arrays of bolometers cooled to mK temperatures inside of a cryostat[3]. The amount of the radiation that couples to the detector is central to its design and construction. As such, an accurate model of the expected optical

[3]Many of these optical elements are cryogenically cooled in the cryostat with the bolometers.

loading due to all of the elements in the optical chain (including the CMB and atmosphere) is required before we can begin designing the physical attributes of the bolometer. For the purposes of modeling the optical loading on a bolometer we model all of the elements which contribute to the optical loading as ideal black bodies, which absorb radiation with some efficiency and are illuminated by the bolometer beam over some fraction of the full 4π sr. For simplicity, it is useful to calculate the loading in the case of perfect absorption and total illumination before we attempt to model a real system.

2.4.1 Photon Brightness

The photon power at a given mode is simply the occupation number of photons, (see Equation 2.10), multiplied by the photons' energy $h\nu$ in some frequency mode $d\nu$.[4] A detailed calculation of n_ν is given in Section 7.4 of the Appendix.

$$n_\nu = \frac{1}{e^{\frac{h\nu}{k_\mathrm{b}T}} - 1} \tag{2.10}$$

Equation 2.11 describes a black body which will radiate at all frequencies in all directions, which allows us to write an expression for the Planck spectral brightness (Equation 2.12) in terms of Equation 2.11.

$$P(\nu, T)d\nu = n_\nu h\nu d\nu = \frac{h\nu}{e^{\frac{h\nu}{k_\mathrm{b}T}} - 1} d\nu \tag{2.11}$$

$$B(\nu, T) = \frac{k_\mathrm{pols} h\nu^3}{c^2[e^{\frac{h\nu}{k_b T}} - 1]} d\nu = \frac{k_\mathrm{pols}\nu^2}{c^2} P(\nu, T) = \frac{k_\mathrm{pols}}{\lambda^2} P(\nu, T)d\nu \tag{2.12}$$

However, bolometers operate in optical systems which limit the illumination to an area, A, a beam solid angle Ω, and transmittance, $\tau(\nu)$. Thus the power incident on the bolometer will be fraction of the total Brightness reduced by the throughput of the telescope integrated across the transmittance of the optical system as shown in Equation 2.13 [72][5][6].

[4] Equation 2.11 in the Raleigh-Jeans limit where $h\nu << k_b T$, becomes $P_\nu(\nu, T)d\nu \approx k_\mathrm{b} T d\nu$ through Taylor expansion of the occupation term.

[5] Diffraction limited optical systems operating at a single mode will have $A\Omega = \lambda^2$

[6] $k_\mathrm{pols} = 1, 2$ for single polarization and intensity measurements respectively.

$$P_{\text{total}}(\nu,T) = \int_0^\infty A\Omega\tau(\nu)B(\nu,T)d\nu = k_{\text{pols}}\int_0^\infty A\Omega(\frac{v}{c})^2\tau(\nu)P(\nu,T)d\nu \tag{2.13a}$$

$$= k_{\text{pols}}\int_0^\infty \tau(\nu)(\frac{A\Omega}{\lambda^2})P(\nu,T)d\nu \tag{2.13b}$$

$$= k_{\text{pols}}\int_0^\infty \tau(\nu)\frac{h\nu}{[e^{\frac{h\nu}{k_b T}}-1]}d\nu \tag{2.13c}$$

2.4.2 Modeling a Real System

Figure 2.4 shows a mock optical system to illustrate the calculation of optical loading for a real experiment. We must consider the contribution to the total loading for each of the elements in the system.

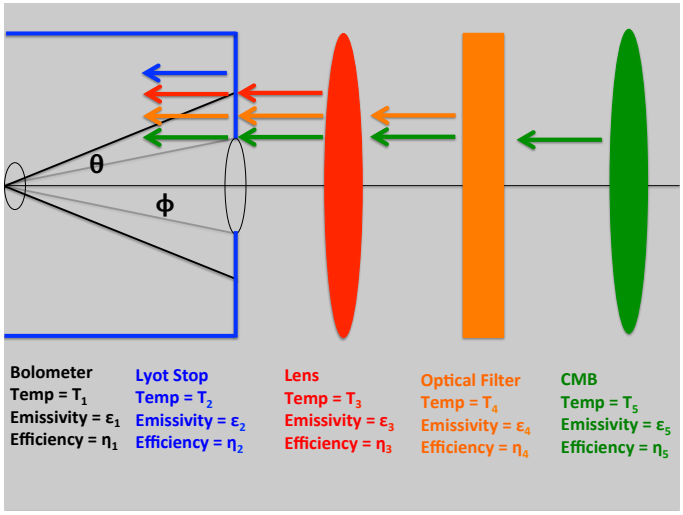

Figure 2.4: A cartoon diagram of a cryostat with 4 optical elements: a Lyot Stop, an image lens, and optical filter, and the CMB. The Lyot Stop is represented as a blue aperture with a fixed diameter. The lenses and filters are each modeled with a fixed temperature T, transmission efficiency η, and emissivity ϵ. The CMB is modeled as a perfect black body. The total power will be the sum of power from the blue, red, orange, and green arrows multiplied by the bolometer efficiency.

To calculate the total power that the i^{th} optical element at temperature, T_i, can radiate onto the detectors one can integrate the spectral brightness of element mul-

tiplied by the the transmittance of the detector. This integral is shown in Equation 2.14.

$$P_{\mathrm{i,rad}} = k_{\mathrm{pols}} \int_0^\infty \tau(\nu) \frac{h\nu}{[e^{(\frac{h\nu}{T_{\mathrm{i}} k_{\mathrm{b}}})} - 1]} d\nu \tag{2.14}$$

However, Equation 2.14 is too idealized since we must consider real elements which radiate with emissivity, ϵ and bolometers with efficiency, η, which leads to equation 2.15 for single element in the chain.

$$P_{\mathrm{i,absorbed}} = \eta \int_0^\infty \tau(\nu) \frac{\epsilon_i h\nu}{[e^{(\frac{h\nu}{T_i k_B})} - 1]} d\nu \tag{2.15}$$

The calculation is slightly easier to do when we operate in the reverse time sense. Each element will emit its own radiation as well as transmit the radiation of element further away from detector as illustrated by the colored arrows in Figure 2.4. Since the Lyot Stop is the last optical element between the detector's optical cavity and the sky, all of the radiation leaving the Lyot stop will be incident on the detector. Thus the power absorbed by the detector is the power emitted by the Lyot Stop, which is the sum of all 4 transmittance arrow multiplied by the bolometer efficiency as shown in Equation 2.16.

$$P_{\mathrm{bolo,absorb}} = \eta_{\mathrm{bolo}} P_{\mathrm{Lyot,Emit}} = \eta_1 P_{\mathrm{2,Emit}} \tag{2.16}$$

Lyot Stop

CMB experiments will often deploy a cryogenically cooled aperture stop to truncate the beam at an angle given by Φ_{Lyot}. The temperature, location, and size of the Lyot Stop all affect the overall efficiency of the detector and the F-number of the receiver.

We can calculate the throughput efficiency of the Lyot stop as the fraction of the detector's beam that makes it through the Lyot stop with radius r. A Gaussian beam profile with half-angle θ will be truncated to a half angle Φ as shown in Figure 2.4. This means that the Lyot stop is a *negative* element in the sense that the transmittance efficiency is given as $\eta_2 = 1 - \eta_{\mathrm{Lyot}}$.

$$P_{\text{lyot,emit}} = P_{2,\text{emit}} = \int_0^\infty \tau(\nu) \frac{\epsilon_2 \eta_2 h\nu}{[e^{(\frac{h\nu}{T_2 k_\text{b}})} - 1]} d\nu \tag{2.17a}$$

$$P_{\text{lyot,absorb}} = P_{2,\text{absorb}} = \eta_1 \int_0^\infty \tau(\nu) \frac{\epsilon_2 \eta_2 h\nu}{[e^{(\frac{h\nu}{T_2 k_\text{b}})} - 1]} d\nu \tag{2.17b}$$

$$P_{2,\text{absorb}} = \eta_1 P_{2,\text{emit}} \tag{2.17c}$$

Lens and Filter

The model for the lens and optical filter is now straightforward. Continuing to operate in the reverse time sense, the loading from the lens will be its spectral brightness integrated over the transmission of the detector and multiplied by the throughput efficiency of the Lyot stop as show in Equation 2.18.

$$P_{\text{lens,emit}} = P_{3,\text{emit}} = \int_0^\infty \tau(\nu) \frac{\epsilon_3 h\nu}{[e^{(\frac{h\nu}{T_3 k_\text{b}})} - 1]} d\nu \tag{2.18a}$$

$$P_{\text{lens,absorb}} = P_{3,\text{absorb}} = \int_0^\infty \tau(\nu) \frac{\eta_1 \eta_2 \epsilon_3 h\nu}{[e^{(\frac{h\nu}{T_3 k_\text{b}})} - 1]} d\nu \tag{2.18b}$$

$$\tag{2.18c}$$

In a similar fashion the loading from the filter will be its spectral brightness integrated over the transmission of the detector and multiplied by the transmission efficiency of the Lyot stop and the transmission efficiency of the lens as show in Equation 2.19.

$$P_{\text{filter,emit}} = P_{4,\text{emit}} = \int_0^\infty \tau(\nu) \frac{\epsilon_4 h\nu}{[e^{(\frac{h\nu}{T_4 k_\text{b}})} - 1]} d\nu \tag{2.19a}$$

$$P_{\text{lens,absorb}} = P_{4,\text{absorb}} = \int_0^\infty \tau(\nu) \frac{\eta_1 \eta_2 \eta_3 \epsilon_4 h\nu}{[e^{(\frac{h\nu}{T_4 k_\text{b}})} - 1]} d\nu \tag{2.19b}$$

CMB

The CMB in this model is the last element in the optical chain and is be treated just like any other optical element as shown in Equation 2.20. The loading will simply be the spectral brightness integrated over the illumination and transmittance of the optical system and multiplied by the transmission efficiencies of elements further down the chain.

$$P_{\text{cmb,emit}} = P_{\text{3,emit}} = \int_0^\infty \tau(\nu) \frac{\epsilon_5 h\nu}{[e^{(\frac{h\nu}{T_5 k_\text{b}})} - 1]} d\nu \tag{2.20a}$$

$$P_{\text{lens,absorb}} = P_{\text{3,absorb}} = \int_0^\infty \tau(\nu) \frac{\eta_1\eta_2\eta_3\eta_4\epsilon_5 h\nu}{[e^{(\frac{h\nu}{T_5 k_\text{b}})} - 1]} d\nu \tag{2.20b}$$

$$\tag{2.20c}$$

Total Loading

As we move away from the detector the power absorbed from the i^{th} element in the optical chain will be its radiative power multiplied by the cumulative efficiency of the elements up to that point as shown in equation 2.21.[7]

$$P_{\text{i,absorbed}} = \int_0^\infty \tau(\nu) \frac{\eta_i^{cum}\epsilon_\text{i} h\nu}{[e^{(\frac{h\nu}{T_\text{i} k_\text{b}})} - 1]} d\nu \tag{2.21a}$$

$$\eta_i^{cum} = \prod_{n=1}^{i-1} \eta_\text{n} \tag{2.21b}$$

Now that we have model for the loading from each element we can compute the total expected loading on the detector by summing the power absorbed from each optical element by the bolometer as shown in Equation 2.22.

$$P_{\text{bolo,total}} = \sum_i P_{\text{i,absorbed}} \tag{2.22}$$

This calculation is unique to each experiment and generally will include more elements which are physically present in the system. For ground base experiments the total loading is usually 5 to 15 pW and for balloon-borne experiments the total loading is typically 3 to 5 pW.

2.5 Bolometer Noise

Transition Edge Sensor (TES) bolometer noise have 4 primary sources: photon noise, thermal carrier noise, resistive Johnson noise, and noise introduced by the bias and readout electronics.

[7]The Lyot stop requires special treatment since it is a *negative element* described in Section 2.4.2.

2.5.1 Photon Noise

Photon noise arises from a non-uniform absorption rate of photons by the detector. The magnitude of these fluctuations depends only on the total optical power absorbed by the bolometer and is analytically written as Equation 2.26. To understand equation 2.26 we start by considering the fluctuations in the power absorbed by the detector from a statistical perspective.

If we consider the variance (see Equation 2.23) in the arrival of photons, σ_ν^2 which is generically written in Equation 2.23, we can model the variance in the optical power, NEP_ν, as function of variance in occupation number per standing wave mode.

$$\sigma_\nu^2 = \langle (n_\nu - \langle n_\nu \rangle)^2 \rangle \tag{2.23a}$$
$$\sigma_\nu^2 = \langle n_\nu^2 - 2n_\nu \langle n_\nu \rangle + \langle n_\nu \rangle^2 \rangle \tag{2.23b}$$
$$\sigma_\nu^2 = \langle n_\nu^2 \rangle - 2 \langle n_\nu \rangle^2 + \langle n_\nu \rangle^2 \tag{2.23c}$$
$$\sigma_\nu^2 = \langle n_\nu^2 \rangle - \langle n_\nu \rangle^2 \tag{2.23d}$$

A calculation for $\langle n_\nu^2 \rangle$ is shown in Section 7.4 of the Appendix.

$$\langle n_\nu^2 \rangle = \langle n_\nu \rangle + 2 \langle n_\nu \rangle^2 \tag{2.24}$$

Plugging the result of Equation 2.24 into Equation 2.23 we find that the variance in the occupation number is given by Equation 2.25.

$$\sigma_\nu^2 = n_\nu + n_\nu^2 \tag{2.25}$$

Recalling that total power incident on the bolometer depends on the throughput of the telescope (Equation 2.13), we write an expression for the mean square fluctuations in photon energy arriving in 1s intervals. We simply integrate over the whole bandwidth the energy fluctuations $\delta P = (h\nu)^2 \sigma_\nu^2$ by the number of polarization, k_{pols}, and the optical throughput, $\frac{A\Omega}{\lambda^2}$, and the transmittance of the system, $\tau(\nu)$ as shown in Equation 2.26.

We now derive a closed form expression for NEP_γ (per unit bandwidth) by multiplying the power at each mode ($d\nu$) by the variance in its occupation number as shown in Equation 2.26.

$$NEP_\gamma^2/B == \int_0^\infty k_{\rm pols}\frac{A\Omega}{\lambda^2}\tau(\nu)(\delta P)^2 = \int_0^\infty k_{\rm pols}\frac{A\Omega}{\lambda^2}\tau(\nu)(h\nu\sigma_\nu)^2 \tag{2.26a}$$

$$= \int_0^\infty \tau(\nu)k_{\rm pols}\frac{A\Omega}{\lambda^2}h\nu n_\nu d\nu + \int_0^\infty \tau(\nu)k_{\rm pols}\frac{A\Omega}{\lambda^2}(h\nu n_\nu)^2\nu \tag{2.26b}$$

$$= \int_0^\infty \tau(\nu)h\nu[\frac{A\Omega}{\lambda^2}\frac{k_{\rm pols}h\nu}{e^{h\nu/k_bT}-1}]d\nu + \int_0^\infty \frac{\tau(\nu)\lambda^2}{k_{\rm pols}A\Omega}[\frac{A\Omega}{\lambda^2}\frac{k_{\rm pols}h\nu}{e^{h\nu/k_bT}-1}]^2 d\nu \tag{2.26c}$$

$$= \int_0^\infty \tau(\nu)P_\nu h\nu d\nu + \int_0^\infty \tau(\nu)\frac{\lambda^2}{k_{\rm pols}A\Omega}P_\nu^2 d\nu \tag{2.26d}$$

$$\text{where } P_\nu = \frac{A\Omega}{\lambda^2}\frac{k_{\rm pols}h\nu}{e^{h\nu/k_bT}-1} \text{ (See Equation 2.13b)} \tag{2.26e}$$

We can recongnize 2.26e as the form reported in [72]. From this equation it becomes clear that the photon noise is a function of the total power P_ν and the bandwidth of the bolometer $\tau(\nu)$.

2.5.2 Thermal Carrier Noise

Another principal noise source for TES Bolometers comes from fluctuations in the number of phonon modes that carry heat from the TES to the cold bath. This noise is referred to as thermal carrier noise and is defined in Equation 2.27 [49]. In order to understand thermal carrier noise for a TES bolometer, we must consider the power flow across the weak thermal link, G_0 in Figure 2.1. We define $P_{\rm sat}$ to be the power flow through weak thermal link when the TES is held in its superconducting transition $T_{\rm c}$ and the thermal bath is at its base temperature $T_{\rm b}$. If the incident power is increased beyond $P_{\rm sat}$ the TES is driven out of its superconducting transition causing it to 'saturate' and most of its temperature sensitivity. In practice, it is common to design $P_{\rm sat}$ such that it is 2 to 3 times larger than the optical load, $P_{\rm opt}$ (i.e. power absorbed by the detectors).

$$NEP_{\rm g} = \sqrt{4\gamma k_{\rm b}T_{\rm c}^2 g} \tag{2.27}$$

where γ is a numerical factor that depends on, n, the index for thermal conductivity which depends on the type(s) of materials used for the thermal path, and the ratio of T_c to T_b [6].

$$\gamma = \frac{n+1}{2n+3}\frac{1-(\frac{T_{\rm bath}}{T_{\rm c}})^{2n+3}}{1-(\frac{T_{\rm bath}}{T_{\rm c}})^{n+1}} \tag{2.28}$$

To put this formula into more familiar parameters for the actual optimization of the bolometer we refer back to Figure 2.1 and Equation 2.3 to get Equation

2.27 in terms of $P_{\rm sat}$. Plugging Equation 2.28 into Equation 2.27 and recalling that $g(T) \equiv dP/dT$ (which we can get by differentiating Equation 2.3 with respect to $T_{\rm bolo}$) we get Equation 2.29.[8]

$$NEP_{\rm g} = \sqrt{4k_{\rm b}T_{\rm c}^2\gamma\frac{dP_{\rm sat}}{dT}} \tag{2.29a}$$

$$= \sqrt{4k_{\rm b}T_{\rm c}^2\gamma[k_0\frac{A_{\rm cross}}{l}T_c^n]} = \sqrt{4k_{\rm b}T_{\rm bath}\frac{T_{\rm c}}{T_{\rm bath}}\gamma[k_0\frac{A_{\rm cross}}{l}T_c^{n+1}]} \tag{2.29b}$$

$$= \sqrt{4k_{\rm b}T_{\rm bath}P_{\rm sat}}\sqrt{(\frac{T_{\rm c}}{T_{\rm bath}})[\frac{n+1}{1-(\frac{T_{\rm bath}}{T_{\rm c}})^{n+1}}]\frac{n+1}{2n+3}\frac{1-(\frac{T_{\rm bath}}{T_{\rm c}})^{2n+3}}{1-(\frac{T_{\rm bath}}{T_{\rm c}})^{n+1}}} \tag{2.29c}$$

$$= \sqrt{4k_{\rm b}T_{\rm bath}P_{\rm sat}}\sqrt{\frac{(n+1)^2}{2n+3}\frac{(\frac{T_{\rm c}}{T_{\rm bath}})^{2n+3}-1}{((\frac{T_{\rm c}}{T_{\rm bath}})^{n+1}-1)^2}} \tag{2.29d}$$

Equation 2.29 tells us that the thermal carrier noise only depends on $P_{\rm sat}$, the bath temperature, and the material dependent value of n, which makes optimization straightforward, to minimize $NEP_{\rm g}$ we must minimize $P_{\rm sat}$ given the optical loading conditions for any given experiment.

2.5.3 Johnson Noise

A significant source of noise in TES Bolometers arises from the fact that the TES remains partially resistive while operating. This gives rise to Johnson current noise which is well understood. The noise equivalent power of a TES with resistance R and temperature $T = T_{\rm c}$ and is shown in Equation 2.30.

$$NEP^2_{\rm Johnson} = 4k_{\rm b}TR \tag{2.30}$$

For the values of R and T used in this thesis (typically 1 Ω and 500 mK) the Johnson Noise is sub-dominant to the other sources of noise. However, the readout electronics and basic operation of the bolometer constrain $T_{\rm c}$ and $R_{\rm bolo}$ so that it cannot be made arbitrarily low.

2.5.4 Readout & Bias Noise

The 300 K readout electronics also contribute to the overall noise seen in the bolometer signal. We always reference this noise to the input coil of the SQUID so that it can be added in quadrature with the bolometer noise. At the input coil of the

[8]See Section of the Appendix for more details on the calculation.

SQUID we can account for the noise produced by the SQUID as well as the Johnson noise produced by the various elements on the SQUID readout boards. In general we write the readout noise as a current noise multiplied by the bias voltage (taking into account the loop gain's effect on bolometer responsivity) as shown in Equation 2.31.

$$\begin{aligned} NEP_{\text{readout}} &= V_{\text{bias}} \frac{\mathscr{L}+1}{\mathscr{L}} NEI_{\text{readout}} \\ NEP_{\text{readout}} &\approx V_{\text{bias}} NEI_{\text{readout}} \\ NEP_{\text{readout}} &= \sqrt{R_{\text{bolo}} P_{\text{bias}}} NEI_{\text{readout}} \end{aligned} \tag{2.31}$$

This is difficult to analytically model so it is typically measured empirically. Many experiments share the frequency domain multiplexing readout electronics produced by McGill University and find that these electronics produce $NEI_{\text{readout}} \approx 7$ pA/Hz$^{-1/2}$ (referenced to the input coil of the SQUID) [6, 18, 81].

2.5.5 Noise Summary and NET

Since these noise sources are uncorrelated we can add them in quadrature to calculate the total noise in the bolometer as shown in Equation 2.32.

$$NEP_{\text{total}} = \sqrt{NEP^2_{\text{photon}} + +NEP^2_{\text{ThermalCarrier}} + NEP^2_{\text{Johnson}} + NEP^2_{\text{readout}}} \tag{2.32}$$

The noise equivalent temperature (NET) is defined as the temperature of a signal that will give a signal-to-noise ratio of 1 after 1 second integration time and is the ratio of NEP to the bolometers power sensitivity to changes in temperature as shown in Equation 2.33.[9]

$$NET = \frac{NEP_{\text{total}}}{\sqrt{2}\frac{dP}{dT}} \tag{2.33}$$

We can calculated the responsivity dP/dT by taking the temperature derivative of Equation 2.13b to get Equation 2.34[10].

[9] A factor of $\sqrt{2}$ arises from the integration time differences (0.5 and 1 seconds) in the definitions of NEP and NET.

[10] Note we make this calculation for a single-mode experiment, i.e. $A\Omega = \lambda^2$ and assume that the detector has some efficiency η, which multiplied by the transmittance of the system $\tau(\nu)$ becomes $\eta(\nu)$

$$\frac{dP}{dT} = \frac{d}{dT}[\int_0^\infty \eta k_{\text{pols}} \tau(\nu)(\frac{A\Omega}{\lambda^2})P(\nu,T)d\nu] \tag{2.34a}$$

$$= k_{\text{pols}} \int_0^\infty \eta(\nu) \frac{d}{dT}[\frac{h\nu}{e^{h\nu/k_bT}-1}]d\nu \tag{2.34b}$$

$$= k_{\text{pols}} \int_0^\infty \eta(\nu) h\nu - [\frac{\frac{-h\nu}{k_bT^2}e^{h\nu/k_bT}}{(e^{h\nu/k_bT}-1)^2}]d\nu \tag{2.34c}$$

$$= k_{\text{pols}} \frac{h^2}{k_b} \int_0^\infty \eta(\nu)(\frac{\nu}{T_{\text{CMB}}})^2 \frac{e^{h\nu/k_bT_{\text{CMB}}}}{(e^{h\nu/k_bT_{\text{CMB}}}-1)^2}d\nu,\ T \equiv T_{\text{CMB}} \tag{2.34d}$$

$$\tag{2.34e}$$

We can reduce this expression to an integral which can be easily solved for numerical by making a change of variables as shown in Equation 2.35.

$$\frac{dP}{dT} = k_{\text{pols}} \int_0^\infty \eta(\nu) k_b (\frac{h\nu}{k_bT_{\text{CMB}}})^2 (e^{h\nu/k_bT_{\text{CMB}}})[\frac{1}{(e^{h\nu/k_bT_{\text{CMB}}}-1)}]^2 d\nu \tag{2.35a}$$

$$x \equiv h\nu/k_bT_{\text{CMB}},\ \ d\nu = k_bT_{\text{CMB}}/hdx \tag{2.35b}$$

$$= \frac{k_{\text{pols}}k_b^2T_{\text{CMB}}}{h} \int_0^\infty \eta(x) e^x [\frac{x}{e^x-1}]^2 dx \tag{2.35c}$$

Equation 2.35 tells us a few important pieces of information about the optimization process. First we see a dependence on $\eta(\nu)$ (or $\eta(x)$). We optimize NET by maximizing the absorption efficiency over the band $\Delta\nu$ and/or increase the bandwidth $\Delta\nu$ if the input NEP from Equation 2.33 is constant.

2.6 Spiderweb-Absorber Transition Edge Sensor Bolometers

Thus far we have laid down the general framework for optimizing a generic TES bolometer. The following section discusses the optimization of a specific type of TES bolometer called a Spiderweb Absorber Transition Edge Sensor (SATES) Bolometer. Early bolometers were constructed using small blackened metal or thin metal film (such as Bismuth) for the absorber material [72]. These absorbers tend to have a large heat capacity and limit the bolometer response time and absorptive area. Micro-mesh absorbers were developed by Mauskopf in the late 1990s, as an alternative. Instead of a bulk or continuous metal film the absorber is constructed as simple grid of highly conductive wire and a grid spacing that is much less than the wavelength of light being absorbed. Under this condition, the structure will behave like a thin film and provide good absorption across a wide range of frequencies while having a significantly reduced heat capacity [50].

The micro-mesh absorbers presented in this thesis are constructed on gold-coated silicon nitride membranes patterned in the shape of a spiderweb and then thermally isolated from the silicon substrate. The absorber is coupled to a TES with a superconducting transition temperature, T_c, of about 500 mK. At these temperatures the gold remains normal and is an excellent conductor of heat, which allows the absorber to be thermally coupled to the TES.

2.6.1 Optical Cavity and Photon Coupling

In order to discuss the performance and advantages of the spiderweb absorber it is useful to outline how these detectors are integrated into the experiment. A common and proven technique for coupling a radiation absorber to the sky is through a highly conductive feed horn [15]. In the reverse time sense, the beam of the detector diverges from these horns and is coupled to the primary mirror of the telescope through a series of focusing and imaging filters (as well as thermal filters to block unwanted infrared (IR) radiation). A typical integration cavity for one of these bolometers is shown in Figure 2.6.1.

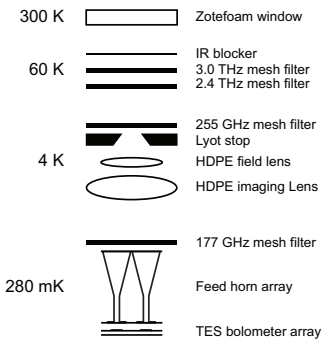

(a) Example Filter Stack

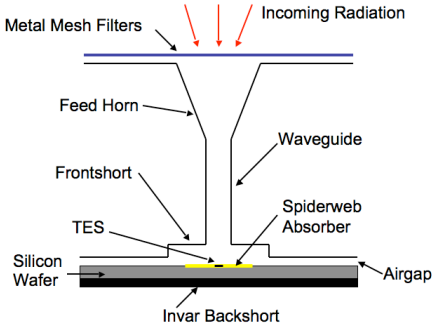

(b) mK Coupling

Band Defining Filters

Metal mesh filters define the upper edge of the bandwidth of the detector. Capacitive metal mesh filters make excellent low pass filters and can be tuned to filter a variety of frequencies by modulating the spacing of the wires embedded into an epoxy material [3]. A SolidWorks diagram of the EBEX focal plane is shown in Figure 2.5.

Feed Horns

Feed horns provide an optimal coupling between free space and the detectors. They exhibit high transmission efficiency, low side-lobs, highly symmetric beam patterns, and large bandwidths [15]. The horn arrays presented in this thesis machined

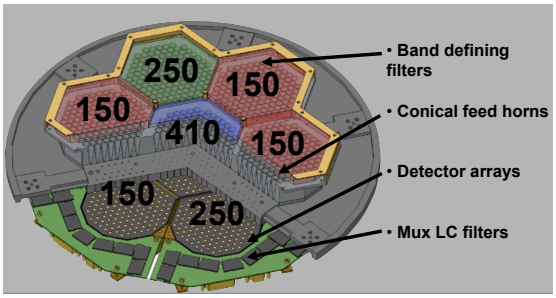

Figure 2.5: A SolidWorks rendering of a single EBEX focal plane showing the placement of the metal mesh filters above the feed horns. The frequency sensitivity of each wafer is tuned with its 'device' wafer (backshort) thickness and is matched to the horn/metal mesh combination appropriate to that bands desired bandwidth.

out of large blocks of aluminum using a Computer Numerical Controlled drilled by a skilled machinist at UC Berkeley. An example of a monolithically-machined feed horn array for the ASTE experiment is shown in Figure 2.6. The horn arrays are then gold plated to maximize their conductivity. The smooth walls and cylindrical structure of the horn acts like a wave guide and has an impedance of $R_{\text{waveguide}} = 377\ \Omega$ when in vacuum. The impedance of the spiderweb structure is tuned to match the impedance of the waveguide in the horn.

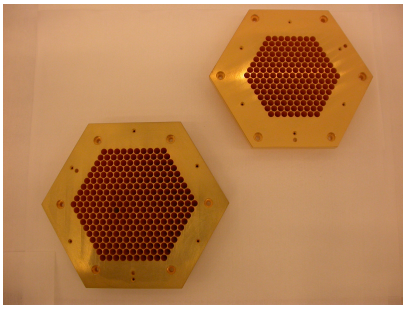

Figure 2.6: A photograph of the two monolithic horn arrays deployed on the ASTE experiment. The arrays in the upper right and lower left are machined for the 350 GHz and 270 GHz respectively.

Backshort Thickness

A superconducting Aluminum back-short and the silicon wafer form the optical cavity for the bolometer. The absorptivity of the bolometer is a function of the thickness and refractive index of the device wafer. The refractive index at 4K of the

silicon used to fabricate the SPT, APEX-SZ, and EBEX array is $n_{\rm Si} = 3.38$ [39]. We chose the device wafer's thickness to be an odd number of quarter wavelengths (in Silicon) to provide the optimal absorptive properties. The $\lambda/4$ cavity ensures that the photon will be phase shifted by a multiple of 2π. Simulations in HFSS reveal that that the use of a $\lambda/4$ backshort provides superior absorption compared to a $3\lambda/4$ design. Simulations results comparing these designs for APEX-SZ at 150 GHz is show in Figure 2.7.

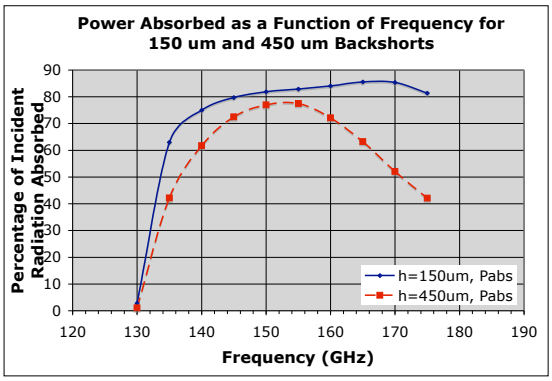

Figure 2.7: Simulation results in HFSS for a 150 μm ($\lambda_{\rm Si}/4$ and 450 μm (3 $\lambda/4$) device wafer across a typical frequency range for 150 GHz (2 mm) detectors. The $\lambda/4$ design provide higher absorptivity across typical bandwidths for CMB experiments.

The thickness of the device wafer must satisfy the quarter-wavelength condition (in Silicon) for each frequency band for each experiment. For high frequencies fabrication wafers becomes a challenge when the quarter-lambda condition requires wafers that are under 100 μm thick. The thinnest wafers discussed in this paper were 56 *pm* 5 μm (for the EBEX 410 GHz band). Table 2.1 lists the device wafer thickness used by the experiments discussed in this thesis.

Spiderweb Absorber

Gold-coated silicon nitride spiderweb structures have been used as absorptive elements for many years [40, 44]. This shape absorbs both polarizations of incoming light, has a suitable beam shape, and provides symmetry which eases fabrication tolerances. Several experiments have combined spiderweb absorber technology with a TES thermistor (APEX-SZ, SPT-SZ, EBEX, and ASTE experiments) [33, 60, 71, 74, 77].

There are three principal design parameters for these devices: web size, web-link size/spacing, and Au thickness. When the web-link size is factor of 6 smaller than the wavelength of the observed radiation it can be modeled as a thin sheet absorber

Experiment	Frequency Band Center(GHz)	Wavelength (mm)	$\lambda_{Si}/4$ Wafer Thickness (μm)
APEX-SZ	150	2.0	150
SPT	90	3.33	250
	150	2.0	150
	220	2.0	100
EBEX	150	2.0	150
	250	1.20	90[a]
	410	0.73	56[a]
ASTE	270	1.11	85[a]
	350	0.85	65[a]

Table 2.1: Summary of the device wafer thicknesses used for four experiments that deployed spiderweb-absorber TES focal planes. [a]:EBEX and ASTE have required fabrication using much thinner wafers than previous experiments (see Section 3.2.5 for more information on the bonding technique).

with the equivalent impedance. Figure 2.8 shows the equivalent absorbed used to model the spiderweb absorbers.

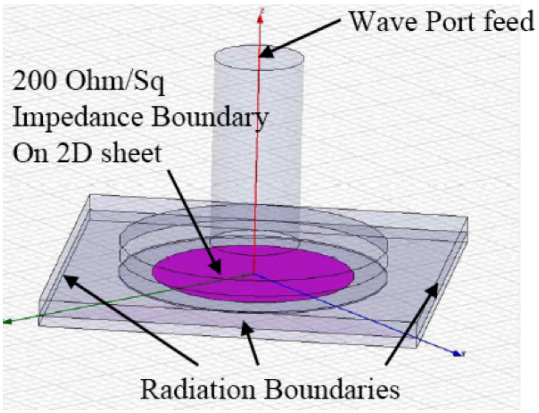

Figure 2.8: A diagram illustrating the sheet resistance model of spiderweb absorber inside the integration cavity. A 2 dimensional thin lossy sheet resistor is used to model the spiderweb absorber. A small fraction of the power is lost at the radiation boundaries and the air gap just above the silicon wafers.

2.6.2 Thermal Isolation and Heat Capacity

As shown in Figure 2.1 the absorber, heat capacity, and TES need to be thermally isolated to establish a temperature gradient across the weak thermal link. Due to the time constant restraints discussed in Section 2.7.2, we must also modify the structures

heat capacity whenever we modify the conductance of the thermal link to ensure the time constant of the bolometer lies within the constraint of the experiment.

Thermal Isolation

During fabrication the bolometer is constructed directly onto the silicon wafer and will be thermally coupled to the thermal bath well. To provide the thermal isolation the bolometer is released from the silicon below by etching away 20-30 μm of silicon beneath the SiN membrane so there is no physical contact with the Si substrate except at the end the bolometer legs which are not released from the bulk of the substrate. Since the absorber is coated with gold we make the approximation that the TES and gold web are completely isothermal and the only temperature gradient occurs from the edge of the web (start of the legs) to the end of the legs where they meet the bulk of the Silicon substrate as shown in Figure 2.9.

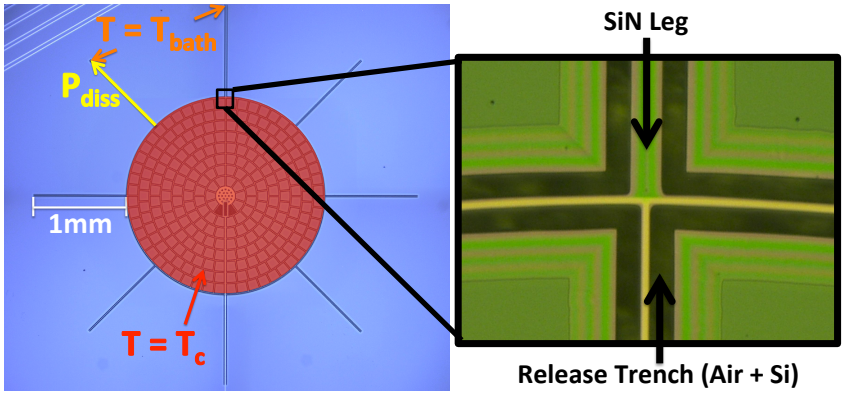

Figure 2.9: **Left:** A photograph of an EBEX bolometer illustrating where the thermal gradient occurs between the bolometer and the thermal bath. **Right:** A 200X magnified photograph showing where trenches are etched into the SiN to allow XeF_2 to etch the silicon below the structure. The regions with dark solid green have silicon below the SiN, the lighter green regions with a slight rainbow pattern are SiN with no Silicon beneath, and the dark regions have no SiN or Silicon nitride. The bolometer structure is suspended ∼25 μm above the silicon substrate.

Heat Capacity

An element whose purpose is to provide extra heat capacity is often necessary to slow down the intrinsic optical time constant of the bolometer to improves stability during operation. The amount of heat capacity that needs to be added depends on the value of G_0. We refer to this added heat capacity as a bandwidth limiting

interface of normal gold (BLING) [11]. In the case of EBEX, G_0 was low enough that the heat capacity from the Al-Ti island and the gold-coated SiN web was enough to keep the time constant between 10 and 20 ms. However, for ASTE, APEXSZ, and SPTSZ (all ground based experiments), we used a much higher value for G_0 which required the addition of and extra gold layer to increase the heat capacity. This layer is only added on top of the small circular waffle structure as shown in Figure 2.11.

2.7 Optimizing Spiderweb Absorber TES Bolometers

Now that we have theoretical framework for the optical loading and bolometer noise we can chose particular design parameters for the SATES bolometer in order to maximize bolometer sensitivity (see Equation 2.33 and Chapter 3 for more detailed information) given the physical properties of the experiment location and construction. For SATES bolometers we have the ability to modify the properties of the spiderweb absorber, the TES (T_c, R_{TES}), the Silicon Nitride legs which thermally isolate the bolometer, and the bolometer's heat capacity. The physics bolometer properties we can tune are summarized in Table 2.2 (see Figure 2.1 for more information).

Property	Attributes to Modify	Minimum Restriction	Maximum Restriction
Saturation Power	$T_{\rm bath}$, $T_{\rm c}$, G_0 (geometry)	$P_{\rm optical}$	$NEP_{\rm tot}$
Time Constants	$R_{\rm TES}$, $C_{\rm bolo}$, G_0 (geometry)	$\tau_{\rm scan}$	$\tau_{\rm readout}$
Absorption Efficiency	Spiderweb geometry, Backshort Thickness	NET	$\eta = 1$

Table 2.2: Summary of the bolometer properties that can be tuned during fabrication.

2.7.1 Optimizing Thermal Carrier Noise

Thermal carrier noise generally is the largest source of non-background (photon) noise in the bolometer. As such optimizing the bolometer's overall noise properties largely depends on a well optimized saturation power. The first step for this optimization is to calculated the expected optical load on the bolometers to set a minimum value for $P_{\rm sat}$, which is chosen to be 2-3 larger than the predicted optical power. When $P_{\rm sat}$ is tuned properly against $P_{\rm opt}$, the bolometer will dissipate roughly equal parts of electrical and optical power, which minimizes both the thermal car-

[11] The term 'BLING' was originally a nickname originating from the fact that this element is simply a chunk of gold and looks like 'Bling-Bling' under a microscope.

Experiment-Frequency (GHz)	Optical Load (pW)	Target $P_{\rm sat}$ (pW)
APEXSZ-150	15	30
ASTE-270	15	40
ASTE-350	20	60
EBEX-150	2.5	7.5
EBEX-250	4.0	12.0
EBEX-410	5.0	15.0

Table 2.3: Summary of optical loads for the experiments presented in this thesis. There are similar loading conditions for APEX and ASTE which are both located on the Chajnantor Plateau, but a large reduction in $P_{\rm sat}$ for EBEX, because of its balloon-borne platform.

rier noise and the readout noise (with a lower voltage bias) while ensuring that the bolometers do not saturate during operation.

Determining Saturation Power

Following the method in Section 2.4, we measure the transmittance, emissivity, reflectivity, and temperature of all of the optical elements in the telescope and cryostat. We combine this with a a model of loading due to the atmosphere, cosmic foregrounds, and the CMB itself to produce an expected load on the detectors. The $P_{\rm sat}$ design targets for the experiments discussed in this thesis are summarized in Table 2.3.

Optimizing $T_{\rm c}$

Once the target $P_{\rm sat} \approx 2.5 P_{\rm optical}$ is fixed we can optimize the thermal carrier noise in terms of T_c/T_b. If we set $T_{\rm bath} = 300$ mK and $P_{\rm sat} = 3.5$ pW into Equation 2.29 and plot it against $T_{\rm c}/T_{\rm b}$ we get Figure 2.10.

As Figure 2.10 shows there is broad minimum in the thermal carrier noise when $T_{\rm c}$ is roughly 1.4 to 2.1 times larger that $T_{\rm b}$. The minimum of the curve is found by taking the derivative of Equation 2.29 with respect to T_c/T_b and setting it equal to 0 and for a system with n=3 corresponds to $T_{\rm c} = 1.7 T_{\rm b}$.

Bath Temperature: The bath temperature is largely independent of the bolometer. However, the base temperature of the cryostat must be known in order to start building a bolometer design. The thermal bath for the bolometers presented in this thesis is created with Simon Chase He-10 sorption fridge that typically cools the bath to ∼250-285 mK. For EBEX, which operated at a bath temperature of 0.275K we had a target $T_{\rm c}$ of $1.7 \times T_{\rm bath} = 0.48$ K.

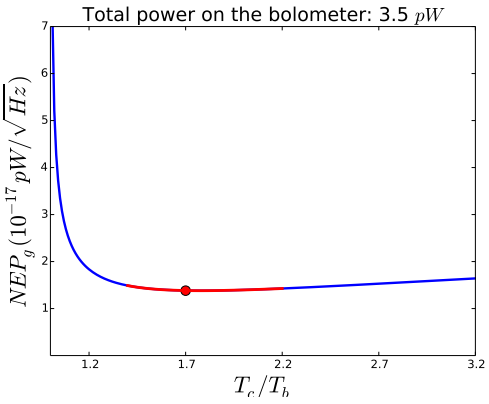

Figure 2.10: Thermal carrier noise (Equation 2.29) plotted as function of T_c/T_b for a 3.5 pW bolometer with n=3 (which is reasonable for Low Stress Silicon Nitride [6, 51, 79]). The analytic minimum is shown with the red dot at $T_c = 1.7T_b$.

Optimizing G_0

The saturation constraint sets a firm lower bound on the minimum P_{sat} for the bolometers, so the next optimization step is design the other readout/bolo properties in such a way that it keeps the total noise low without violating any design or practical constraints. In theory, P_{sat} can be tuned by modifying the geometry of the thermal link and/or the T_c per Equation 2.3. However, we found that it was reliably reproduce consistent T_c values with the equipment we had available, so our strategy was to modulate P_{sat} by changing the geometry of the thermal link and maintaining T_c as constant as possible. Furthermore, thermal carrier noise has a broad optimum for T_c, which means that errors in T_c do not significantly impact noise performance.

To optimize the thermal link we must consider how the thermal properties of the material translate into power dissipation. The simplest model is to assume the standard heat conduction equation derived in many texts books, which says the thermal conductance will scale inversely with leg length and directly with cross-sectional area (see Equation 2.3) [38][12]. In the case of a spiderweb bolometer which is supported by 8 or 12 legs (APEXSZ/SPT/EBEX and ASTE respectively), we model the total conductance to be that of 8 legs (each with their own conductance value) operating in parallel (i.e $G_{tot} = \sum_i G_i$). Using Equation 2.3 and empirical measurements we can isolate the geometric and material factors, A_{cross}, l, & k_0 which ultimately affect P_{sat}. Using measurements P_{sat} and T_c and Equation 2.3, we

[12]For typical bolometer leg geometry this model only works so well since the phonons may not behave both ballistically and in a bulk manner. As such dependence on A_{cross}/l is softened.

can find a empirical value for the effective thermal conductance, G_0 . Since the value of G_0 needs to be tuned against the expected optical loading which increases with frequency, EBEX deployed 4 different designs for the SiN leg structure geometries (see Figure 2.9) to achieve different G_0 values for the different bands. The empirically determined values of G_0 from 3 EBEX wafers (i.e. unique spiderweb leg geometry) are shown in Table 2.4.

Table 2.4: Summary of the pre-factor values of Equation 2.3 for the 3 EBEX bands. The value of the pre-factor scales monotonically with the effective $A_{\rm cross}/l$ and G_0.

Experiment-Frequency (GHz)	G_0 (pW/K)	Mask Used
EBEX-150-47	30	EBEX SiN Low-G
EBEX-250-24	52	EBEX SiN High-G
EBEX-410-28	85	EBEX SiN Highest-G

2.7.2 Optimizing Time Constants

The thermal time constant of the bolometer, τ_0, is set by the heat capacity, $C_{\rm bolo}$, the thermal conductivity, G_0, and loop gain, $\mathscr{L}$, of the detector during operation (see Equation 2.8). If the time constant is too short, the detector bandwidth exceeds the readout bandwidth which leads to instabilities in the operation of the detector. On the other hand, if the time constant is large compared to the scan speed of the telescope and the beam size, the bolometer signal will have elevated $1/f$ noise.

Readout Bandwidth and TES Resistance

The time constant of the detector is constrained on the lower end by the bandwidth of the frequency domain multiplexing readout electronics, which provide an AC voltage bias to a bolometer wired to a LCR notch filter. The fundamental time constant of this readout circuit is set by Equation 2.36.

$$\tau_{\rm readout,max} = \frac{L_{\rm max}}{R_{\rm min}} \tag{2.36}$$

where $L_{\rm max}$ and $R_{\rm min}$ are constrained by cross talk requirements and are typically $\sim$20 nH and $\sim$1 Ω, which give $\tau_{\rm readout,max} \approx 20$ ns. [81]. Following the work of Hilton and Irwin, we can write down differential equations for the thermal and electrical states of a voltage biased TES as shown in Equation 2.37.

$$\begin{aligned} C\frac{dT}{dt} + G(T_{\rm c} - T_{\rm b}) &= P_{\rm opt} + P_{\rm elec} \\ V &= L\frac{dI}{dt} + IR_{\rm L} + IR_{\rm TES} \end{aligned} \tag{2.37}$$

Solving this coupled set of differential equations leads to Equation 2.38 which describes the time constant of the readout.

$$\tau_{\pm} = \left[\frac{1}{2\tau_{\rm elec}} + \frac{1}{2\tau_1} \pm \frac{1}{2}\sqrt{\left(\frac{1}{\tau_{\rm elec}} - \frac{1}{\tau_1}\right)^2 - 4\frac{R_{\rm TES}}{L}\frac{\mathscr{L}(2+\beta)}{\tau}} \right]^{-1} \tag{2.38}$$

We notice that this solution has both a positive and negative solution (denoted with $\pm$). The system will not roll off exponentially when $\mathrm{Re}[\tau_- > 0]$ nor will it have an under damped response to TES oscillations. Furthermore, the bolometers are operated in the high loop gain limit where $\mathscr{L} >> 1$ and $\beta = 0$. This leads to the constraint that the detector time constant must be $\sim$5.8 times larger than the readout time constant. This simplifies to Equation 2.39. [35, 81]

$$\tau_{\rm detector} \geq 5.8 \times \tau_{\rm readout,max} \geq 5.8 \times (2 \times 10^{-8})s = 115{\rm ns} \tag{2.39}$$

Scan Speed

The scan speed and the beam size of the telescope set the upper limit on the acceptable value of τ_0. EBEX was designed to scan across the sky at ≤ 1 [deg/sec] and has beam size $\theta_{\rm FWHM}$ $8'$[71]. Thus the fundamental time constant for astronomical signals coupling through the telescope is given by $\tau_{\rm sky} = \theta_{\rm FWHM}/v_{\rm scan}$. The sample rate of the sky must be faster than they Nyquist frequency of the scan pattern, which requires that our time constant be at least twice as fast as $\tau_{\rm sky}$. In practice we introduce an additional safety factor of 2 to ensure that the time constant is set appropriately even if there are variations in fabrication. In Equation 2.40, we define the upper limit on detector time constant to be 2 times the scan Nyquist Frequency set by the scan speed and beam width.

$$\begin{aligned} \nu_{\rm detector} \geq 2 \times \nu_{\rm sky,Nyquist} = 2 \times 2 \times \nu_{\rm sky} = 2 \times 2 \times \frac{v_{\rm scan}}{\theta_{\rm FWHM}} \\ \tau_{\rm detector} \leq \frac{1}{2 \times 2}\frac{\theta_{\rm FWHM}}{v_{\rm scan}} \end{aligned} \tag{2.40}$$

Bolometer Heat Capacity

Although the bolometer time constant depends on both G_0 and C_0, we typically tuned G_0 independently of $\tau_{\rm detector}$, in order to optimize $NEP_{\rm g}$ and $P_{\rm sat}$. Once the value of G_0 is set, we can correct Equation 2.39 with the addition/removal of heat

capacity. For EBEX, Equations 2.40 2.39 and suggests that 0.11 μs$\leq \tau_{\rm detector}/(1+\mathscr{L}) \leq$ 33 ms. Typically speaking the G_0 values were low for EBEX detectors and we found that the heat capacity of the gold web and TES material was sufficient to keep the bolometer time constants between 10 and 20 ms.

2.7.3 Optimizing NET

The last thing to optimize from the perspective of detector fabrication is the absorption efficiency of the detector across the entire desired bandwidth. The absorption efficiency is defined as the ratio of the power sensed by the TES to the ratio of power incident on the TES [13]. This optimization is mathematically easiest to understand in the Rayleigh-Jeans limit where $P_\nu = k_{\rm b}T$. The total power absorbed by the TES is given by Equation 2.41.

$$P_{\rm absorbed} = k_{\rm b} T_{\rm CMB} \eta_{\rm detector} \Delta\nu_{eff} \tag{2.41}$$

,where $\Delta\nu_{eff} = \int_0^\infty F(\nu)d\nu$ (i.e. the band pass function). Both the effective bandwidth, $\Delta\nu_{\rm eff}$, and the detector efficiency, $\eta_{\rm detector}$ will increase the fraction of the total possible power absorbed. In general the absorbing element is optimized to ensure high efficiency over a broad bandwidth and the backshort and optical cavity are optimized to ensure that the detector absorbs as much radiation with the desired band width as possible.

Backshort Thickness

Finally we can optimize $\Delta\nu$ in Equation 2.41 by choosing an appropriate backshort thickness (see Chapter 3). In short, using $\lambda/4$ backshort provides much better absorptivity across the band compared to a $3\lambda/4$ backshort design [51, 77, 90].

Spiderweb Absorber

A photograph of an ASTE spiderweb absorber is shown in Figure 2.11 [89]. The web grid spacing $g_{\rm web}$ and web thickness are tuned to maximize the absorption efficiency. When $g_{\rm web} << \lambda$ (at least a factor of 6), the spiderweb absorber acts very similarly to a lossy sheet resistor with a resistance given by Equation 2.42.

$$R_{\rm absorber} = \frac{\rho g_{\rm web}}{2 g_{\rm width} g_{\rm thickness}} \tag{2.42}$$

The values of $g_{\rm web}$, $g_{\rm width}$, and $Au_{\rm thickness}$ are tuned to achieve a sheet resistivity of $R_\square \approx$ 400-500/ $\Omega_\square$ which was shown by Jared Mehl to optimize absorptivity at 150

[13] This should not be confused with the overall receiver efficiency which calculates the total loss of signal in the entire optical chain.

GHz[51]. A detailed comparison of the bolometers used in SPT, ASTE, and EBEX is outlined in Table 2.5.[14]

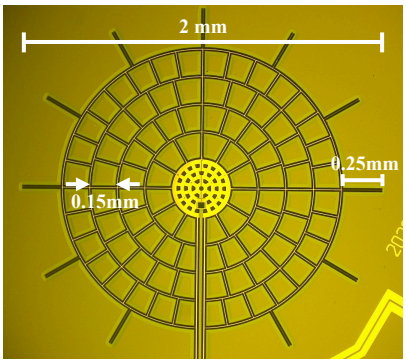

Figure 2.11: A photograph of a ASTE spiderweb absorber. It is constructed out of SiN membrane and a thin gold layer. The spacing between the links of the web is 150 μm and thickness of the gold is 20nm.

Table 2.5: Basic spiderweb absorbers for the 4 experiments in which UC Berkeley was responsible for the fabrication.

Experiment	Frequencies (GHz)	Web Diameter (mm)	Grid Spacing mm
APEX-SZ	150	3.0	0.2
SPT	90, 150, 220	3.0	0.2
ASTE	270, 350	1.5	0.15
EBEX	150, 250, 410	2.0	0.1

2.8 Summary

SATES bolometers make excellent candidates for observations of the cosmos at millimeter and sub-millimeter wavelengths. They have been successfully implemented in many different experiments. Their design is dynamic and can be tailored to a wide variety of deployment environments and can be tailored for many different applications ranging from studies of the SZE, CMB temperature anisotropies, CMB polarization anisotropies, cosmic foregrounds, and dusty galaxies.

[14]See Figure 7.2 in 7.2 of the Appendix for a photographic comparison

Chapter 3

Fabrication of Spiderweb TES Bolometer Arrays

3.1 Introduction

Early CMB experiments employed bolometers which were assembled individually by hand. Construction of these bolometers was an arduous process prone to error [40, 44]. As detector technology progressed so did the need to build ever more sensitive experiments, which required improving the detector technology and increasing the detector counts of CMB experiments by a factor of ∼100. It became necessary to produce large arrays of bolometers in a single step. A natural solution to this problem came from replacing semi-conductor thermistors (e.g. NTD-Ge thermistors used by Maxima and Boomerang [40, 44]) with lithographed superconductor metal film thermistors. Superconducting metals can be deposited and patterned on silicon using standard microfabrication techniques and make great material for Transitions Edge Sensors (TES). This provides a basis to monolithically fabricate bolometer arrays on silicon wafers in a clean room environment allowing for the construction of thousands of ultra-sensitive bolometers with uniform properties on a single silicon wafer [25, 26]. This techniques provide the technological foundation for many upcoming experiments which plan to deploy tens of thousands of bolometers [11, 85].

The Cosmology group at UC Berkeley has a long history of fabricating and deploying detectors arrays for observations of the cosmos. This work is spear-headed by graduate students doing thesis work for the APEXSZ, SPTSZ, POLARBEAR, and EBEX experiments [6, 26, 51, 55, 71, 79, 81]. Much of the work presented in this thesis builds of the previous work done by these talented fabricationists under the supervision of Adrian Lee, Bill Holzapfel, and Paul Richards. UC Berkeley has operated its own clean room facility since 1983 in Cory Hall on the UC Berkeley campus. In 2010, UC Berkeley opened a new ∼$80 million dollar fabrication facility named The Marvell Nanofabrication Facility (MNF). The bulk of the fabrication work done in this thesis was performed at the MNF.

Spiderweb Absorber TES Bolometer Arrays

The work in this thesis focus on a specific type of bolometer called a Spiderweb absorber TES (SATES) bolometer. SATES bolometers are constructed on spiderweb shaped membrane of Silicon Nitride (SiN) suspend above a silicon substrate . The membrane is coated with patterned Niobium (Nb), Aluminum-Titanium (Al-Ti), and Gold (Au), which form the leads, TES, and absorber of the bolometer respectively. Figure 3.1 provides a mapping between the elements in a typical bolometer diagram and the corresponding physical structures on a SATES bolometer which provide that particular attribute.

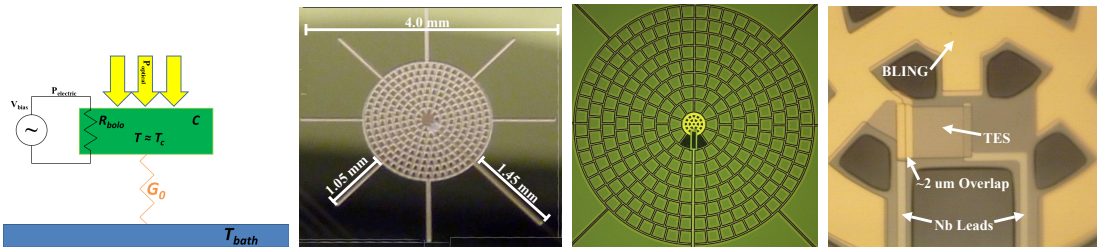

(a) Bolometer Cartoon (b) SiN Legs (c) Spiderweb Absorber (d) TES and BLING

Figure 3.1: **Figure 3.1(a):** The cartoon diagram of a voltage-biased TES bolometer from Chapter 2. **Figure 3.1(b):** A photograph showing the 8 silicon nitride legs used to suspend the entire bolometer structure above the silicon below. The longest leg also carries the Niobium leads which provide the bias and readout the TES signal. **Figure 3.1(c):** A photograph of the spiderweb absorbing element used for the bolometers in this thesis. When the grid spacing of the bolometer is much less than the wavelength of radiation being absorber the structure exhibits high absorption efficiency. **Figure 3.1(d):** A zoomed-in photograph of the TES thermistor and BLING (bandwidth limiting interface of normal gold), which supplies heat capacity to slow the bolometer's time constant below the limit set by the scan speed. The TES is connected to a pair of Niobium leads which provide the AC voltage bias shown in panel 3.1(a).

3.2 Fabrication Details

The arrays are fabricated on a stack of two wafers comprised of the 'device' wafer and the 'backing' wafer as shown in the diagram. In principal only the 'device' wafer is needed to fabricate the array. However, due to the $\lambda/4$ requirement for the silicon backshort, the 'device' wafer must be bonded to a much thicker 'backing' wafer for mechanical stability during fabrication. The Nb, Al-Ti, and Au are are sequentially deposited and patterned before the SiN is etched around the structure to allow for

XeF_2 to etch away the silicon beneath the SiN to 'release' the structure and provide its thermal isolation. A diagram of the wafer stack shown in Figure 3.2 and the layers are summarized in Table 3.1.[1]

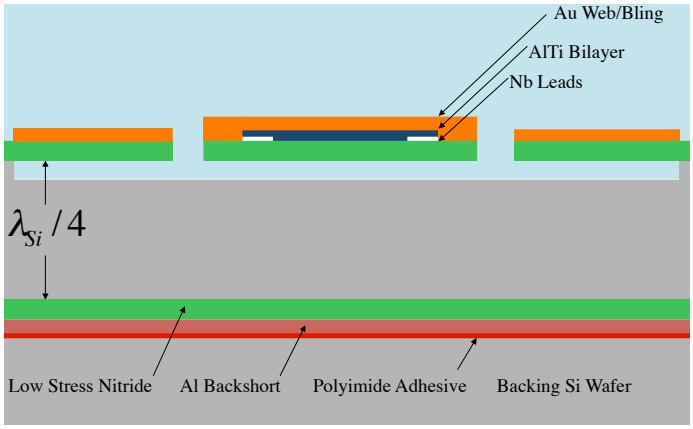

Figure 3.2: A diagram of the EBEX Wafer Stack. All of the metal layers are deposited and patterned prior to releasing the structure from the substrate below leaving it suspended by the SiN legs. See Table 3.1 for more information.

3.2.1 Fabrication Steps

The next section summarizes the steps required to construct an array of SATES bolometers. Each section gives an overview of the steps purpose and its particular process details

1. Wafer Preparation: Prepare the device and backing wafers for fabrication.
2. Low Stress Nitride Deposition: Coat the wafer with the SiN, which is the membrane on which the bolometer is constructed.
3. Back Short Deposition: Depositing a layer of Al on the back side of the device wafer to form a $\lambda/4$ optical cavity for the incoming radiation.
4. Wafer Bonding: Gluing the device wafer using a polyimide to a thicker backing wafer for mechanical stability during fabrication.
5. Niobium Wiring Layer: Depositing and patterning a layer of Nb, which provides the electrical bias and readout leads to interface the array with the readout electronics.

[1]The wafers presented in this thesis were fabricated on 4 inch silicon wafers using microfabrication techniques including low pressure chemical vapor deposition (LPCVD), metal sputtering, metal evaporation, reactive ion etching (RIE), contact and stepper photo-lithography, dry gas etching, and wafer dicing.

Layer	Material	Thickness	Deposition Process	Etch Process
Backplane	Aluminum (Al)[a]	1.0 µm	DC Sputter	NA
Substrate	Silicon	56-150 µm	std. wafer manufacturing	XeF_2 Dry Gas
Membrane	Low-Stress Silicon Nitride (LSN)	1-1.2µm	LPCVD [b]	CF_4 RIE[c]
Bias Leads	Niobium (Nb)	$\sim 120nm$	DC Sputter	CF_4 RIE[c]
TES 1	Aluminum (Al)[a]	$\sim 40nm$	DC Sputter	Al Wet Etch
TES 2	Titanium (Ti)	$\sim 120nm$	DC Sputter	SF_6
Web/Thermal Link/BLING	Gold (Au)[d]	20-1500nm	E-beam Evaporation	Photo-resist Lift Off

Table 3.1: Fabrication layers for spiderweb absorber bolometer fabrication. Note that only the ASTE design requires additional BLING and Thermal Link Layers after the Au web layer is deposited. [a]: All Aluminum used in this fabrication was doped with 2% Si. [b]: Low Pressure Chemical Vapor Deposition. [c]: Reactive Ion Etching. [d]: All Au layers include a 2.5 nm Ti adhesion layer.

6. Niobium Oxide Removal: Removal of the native later of NbO_2 that forms in ambient environment and is a strong electrical insulator a cryogenic temperatures.
7. Aluminum-Titanium TES Layer: Deposition and patterning of Al-Ti bilayer which forms the TES of the bolometer.
8. Gold Absorber, Thermal Link, and BLING Layer: Deposition and patterning of the gold layers that provide the absorbing element, additional thermal conductivity, and additional heat capacity.
9. Silicon Nitride Patterning and Etching: Removing a portion of the SiN to allow access point for XeF_2 to etch away the silicon beneath the SiN.
10. Wafer Dicing: Cutting the array into a shape for integration into the experiment.
11. Wafer Release: Using XeF_2 to thermally isolate the structure by removing the silicon beneath the bulk of bolometer leaving it suspended by its legs.
12. Photo-resist Ash: Clearing away the photo-resist used to protect the bolometers during the SiN etch and bolometer release.
13. Electrical and Visual Inspection: A careful quality control inspection of the wafers visual properties and the electrical properties at 300K.

3.2.2 Wafer Preparation

Silicon Quest International (SQI) can grind and polish high purity silicon wafers to a thickness between 56 and 150 μm with a tolerance of ± 5μm. The wafers are shipped in cylindrical jars with 4 inch discs of anti-static Styrofoam layered between each Silicon wafer in the shipment. To increase the stability during travel the wafers are shipped with plastic backing sheet adhered to the wafer with a photosensitive adhesive. Prior to shipping the plastic is exposed to UV light and the adhesive is weakened enough that it can be removed by a worker in the clean room without damaging the ultra-thin device wafer(s).

The wafers are carefully removed from the jar one-by-one. The wafers are placed face down with the plastic facing the ceiling on a short stack of TechniCloths to protect the surface of the wafer. A needle is firmly attached to a wooden stick to provide a tool capable of creating separation between the wafer and the backing plastic. Small bubbles form between the back of the wafer and the plastic material which provides seed-sites to start lifting the plastic away. The needle is used to lift the edge of the plastic until it is released enough from the wafer that it can be held with a finger tip. At this point the plastic can be carefully rolled wafer from the silicon wafer with little resistance. However, great care must be taken to ensure that the wafer stays flat and does not stick too strongly to the wafer plastic. Once the plastic is removed the wafer is ready for a pre-furnace clean.

3.2.3 Low Stress Silicon Nitride Deposition

Prior to Low-stress Silicon Nitride (LSSN) deposition the wafers under go a standard Metal Oxide Semiconductor (MOS) grade cleaning process. The clean starts with a ten minute Piranha[2] soak, followed by a de-ionized (DI) water quick dump rinse (QDR). Finally any native oxides are removed from the wafer surface by doing a ten second hydrofluoric (HF) acid dip followed by an additional QDR. The wafers are rinsed an additional time and dried in spin rinse drier (SRD) provided by the MNF.

The device wafers are so thin that the cohesive forces of the water can cause the wafers to stick together and in some cases case them to break. The wafers are placed in the wafer cassette with standard thickness backing wafers which are also prepared for LSSN deposition. The rigid backing wafers placed between the device wafers helps reduce the breakage rate of the device wafers.

Once the final SRD cycle is complete, the wafer is ready for LSSN deposition in a Low Pressure Chemical Vapor Deposition (LPCVD) Tystar furnace[3]. The tool

[2]Piranha is sulfuric acid heated to 100°C spiked with ∼100 mL of H_20_2

[3]Dichlorosilane (DCS; SiH_2Cl_2) will react with Ammonia (NH_3) at high temperature to produce non-stoichiometric silicon nitride (LSSN; Si_3N_x)

has a deposition rate that is well characterized by MNF staff and confirmed with a tool-characterization run using test-grade wafers prior to device wafer deposition. Deposition rate, uniformity, and film quality are verified using optical spectroscopy and a microscope for visual inspection. The standard deviation of LSSN thickness was typically less than 2% when measuring the top, left, bottom, right, and center locations of 4 inch wafer. The deposition time for the device wafer was determined by linearly extrapolated the deposition rate of the characterization run to achieve a target thickness of 1.1 $\pm$ 0.1 μm and was typically between 300 and 330 minutes.

3.2.4 Back Plane Deposition

Once the backing wafers and device wafers are coated with LSSN, the optical cavity must be completed by creating a reflective surface on the backside of the device wafer. Aluminum with 2% Si was chosen as the metal for this purpose as it can be reliable deposited using the CPA DC sputtering system at MNF[4].

The skin depth of metals is given by ($\delta = \sqrt{\frac{2\rho}{\omega\mu_0}}$). Work done by Erik Shirokoff and Jared Mehl confirmed that the resistivity of the Aluminum (impregnated with 2% Si) deposited with the CPA confirmed, ρ, the resistivity to be 2 $\mu\Omega \cdot$cm at 2.3K [79, 51]. At 131 GHz , the lower edge of the lowest band used in EBEX is $\approx$ 0.2 μm. As such a thickness of 1 to 1.2 μm provides a highly reflective surface for frequencies of 150 GHz and greater.

3.2.5 Wafer Bonding

The $\lambda/4$ condition requires the use of literally paper thin wafers, which do not have the strength to withstand the fabrication processes. Our group implemented wafer bonding process to adhere the thin device wafer to a much thicker backing wafer for mechanical stability. Once the device wafer is prepped (coated with LSSN on both sides and an Al back short on the 'back' side) and the backing wafer is prepped (coated with LSSN on both sides), they are ready to be bonded.

The bonding process consists of spin coating the inner surfaces (back of device wafer and front of backing wafer) of the wafers with and adhesion promoter and polyimide adhesive[5] using a Headway programmable spinner system.

Between 10 to 15 mL of AP3000 is placed on the inner third of the backing wafer.[6] The spinner slowly ramps up to 3000 rpm over the course of 10 seconds to evenly

[4]DC sputtering done with CPA (Circuits Processing Apparatus, Inc.) 9900 track sputtering system. Deposition done at a base pressure of $\leq 5.0^{-7}$ Torr, 6mTorr Argon process pressure, and 1 kW DC magnetron power with a 15 inch target. The wafer is passed 4 times under the target at a track speed of 13.3 cm/min)

[5]AP3000 (adhesion promoter) and Cyclotene 3022 (polyimide) manufactured by Dow Jones Chemical.

[6]Unused, clean plastic droppers are used each time any product is extracted from the bottle.

distribute the adhesion promoter across the wafer. Once up to speed, the wafer spins at 3000 rpm for 60 seconds and is ramped back down to a stationary position. At this point 10-15 mL of Cyclotene 3022 are careful transfered to the wafer and ramped up to 2000 rpm over the course of 10 seconds and is spun at full speed for 30 seconds, which produces a layer of polyimide approximately 1 μm thick. A small amount of T1100 Rinse solvent is dropped on to a synthetic swab and the wafer is rotated at 5 rpm while the swab is head at the edge of the wafer to remove any edge beads present. The backing wafer is placed carefully to the side and the process is repeated to the back side of the device wafer.

Once each wafer is coated with polyimide, they are manually aligned and carefully placed together such that the surfaces of the wafer are kept as parallel as possible and the major flats are aligned (typically to within a degree). This completes the initial bonding process and the wafer is ready for curing.

The curing process is completed inside a simple vacuum oven pumped below 1 Torr. A hot plate with temperature controller is placed inside the oven. The device wafer is carefully placed onto a chuck between two 1 mm thick dummy wafers[7] with Technicloths on both sides. Iron weights are stacked on top of the wafers to apply roughly 30 PSI on the wafer. The temperature of the hotplate is incrementally increased in three steps to 225°C (75°C , 150°C , 225°C in 30 minute intervals) over the course of 90 minutes. At the point the wafer is carefully removed from the oven to remove the Technicloths and clean the edges of any residual polyimide that beads onto the edge of the wafer. The stack is de-constructed and the polyimide is cleared using acetone and cotton swabs. The stack is remade without the TechniCloths and fresh dummy wafers to ensure the device wafer does not bond to any other objects and surfaces.

The temperature is the set to 350°C and the wafer is left to cure for 8.5 hours. The wafers are typically cured over night and removed the next morning when they are cool. After bonding, they are inspected for cracks, smoothness, and cleanliness. Wafer with large cracks and/or largely uneven surfaces are discarded and a new wafer is bonded. If the wafer passes inspection, it is cleaned with a 10 minute piranha soak, QDR, and SRD. The bonded wafer is marked with is frequency and index name using a carbon tip scribe.

3.2.6 Niobium Wiring Layer

Once the wafer is bonded it is ready for device fabrication. The first step is to deposit and pattern a layer of Niobium (Nb) to provide an electrical interface between the detector and the readout electronics (see Figure 3.2.6). Niobium is an ideal material for this wiring layer. Previous fabrication of these types of arrays used

[7]These stacking wafers are cleaned with a 10 minute Piranha soak, QDR, and SRD after being used to bond a single wafer.

the Aluminum from the TES bilayer for both the TES and wiring layer. Switching to Nb provided many advantages over using the exist Aluminum layer for leads. The first is that Nb is mechanically stronger than Aluminum. The thickness of the aluminum is restricted to thickness between 40 and 50 nm because that provides ~ 500 mK T_c and ~ 1 Ωin the bilayer. The Nb layer thickness can be much thicker since the TES is deposited independently and one only has to worry about step coverage issues. We chose a target thickness of 120 nm for Nb, which makes the wafer more robust against yield loss to do open forming on the leads. Furthermore the Nb sputtered in the nanolab using the Gartek system had a T_c of 7K [6, 55], which facilitates testing as the network analysis of the bolometer array for detector characterization is done at 4K [47].[8]

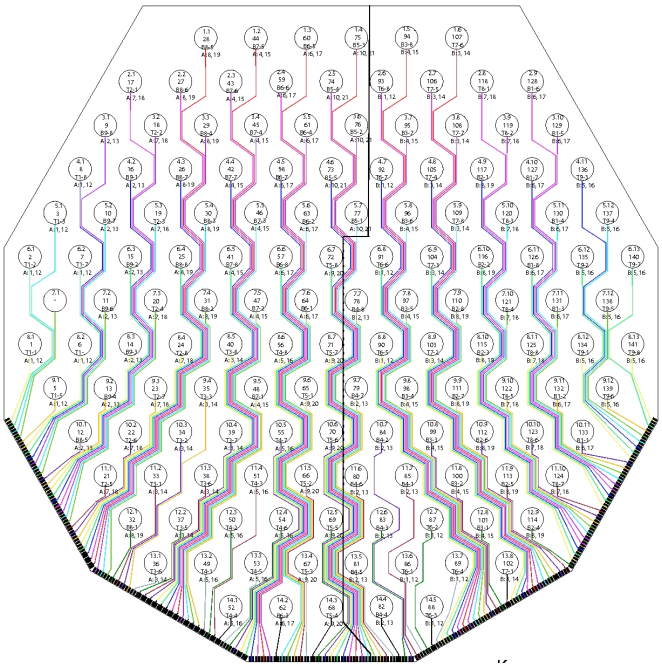

Figure 3.3: A diagram of an EBEX wafer illustrating the naming scheme of the pixels and the mapping of the pixel locations to their respective bond pads. The location of each individual bolometer is programmed into the gcaws system as a fixed offset from the alignment marks printed on the wafer, which allows for the precision alignment of all layers in the process. The bond pads are simply numbered from 1 to 141 from left to right and pixels are identified by their row-column position.

[8]The Nb wiring layer is deposited next using DC magnetron sputtering in the Gartek deposition system with a base pressure of $\leq$ 1.5e-7, $\sim$ 8 mTorr Argon pressure, and 350 V, and 1.5 A.

Alignment Marks

Once 120 nm layer of Nb is sputtered on to the wafer, it is ready for the first lithography step to pattern the bias leads from the TESs to the bond pads at the edge of the wafer. This is the most complex lithography step, because it requires the placement of the alignment marks for all subsequent layers, and the simultaneous use of the Karl Suss Mask Aligner (ksaligner) and the GCA Wafer Stepper (gcaws) on a single photo-resist layer[9].

The gcaws system implements a fixed alignment mark scheme so that multiple layers can align to one another with $\leq 1\mu$m accuracy. The location of all of the EBEX bolometer locations is given by a 2D closed-hex pattern with the diameter of each pixel location set by the physical spacing of the horns. Figure illustrates the layout of an EBEX wafer. The location of each pixel is programmed into gcaws as a relative offset from special alignment marks which are printed during the first lithography step. To do this, an alignment mark mask is loaded into gcaws (see Figure 3.4 for more information on mask-to-gcaws alignment) and two alignment marks (see Figure 3.7)are printed and developed roughly 2/3 of the height of the wafer from the major flat and roughly centered on the wafer. The distance (87.2 mm) between these marks is set by the fixed distance between the objectives in the gcaws system.

Contact Printing of Bond Pads and Bulk Wire

Once the position of the alignment marks is established with an gcaws exposure and photo-resist develop, two more lithography steps complete the patterning of the wiring layer, using the developed photo-resist pattern for alignment. The contact mask which pattens the bond bands and the bulk of the wires has special alignment marks which mate to the alignment marks printed by gcaws. The wafer is aligned to the contact mask prior to exposure using the alignment marks as shown in Figure 3.5. This method allows us to regularly achieve alignment between the stepper and contact lithography to within 1 μm. This pattern contains the bond pads (250 μm pitch) and the 'wires' from the bond pads to the bolometer locations (printed in a close-packed hexagonal pattern).

Stepper Printing of Fine Lead Features

Once the contact printing is finished the fine features of the Nb wiring layer at each bolo location are printed. Unfortunately, the alignment requirements of the of the Nb leads within the pixel require that this portion of the pattern be printed with

[9]Furthermore modifications to the standard photo-resist coating procedure were made. I found that the heated vacuum of the HMDS Primeoven would sometimes cause the wafers to debond. I replaced the HMDS priming step with a 1 minute 90°C hard-bake on a hot plate to dehydrate the wafer followed by 2 minutes in HMDS bubbler box. I found that this was sufficient for photo-resist adhesion during wafer processing.

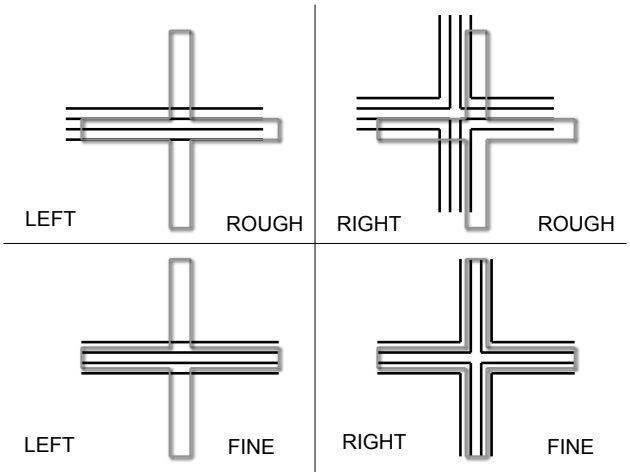

Figure 3.4: A diagram illustrating the gcaws mask alignment system. The mask has either a cross-shaped window or a dark cross printed directly on it (shown in gray). The gcaws exposure columns has two objectives placed directly above the marks with the sets of dark lines embedded in them. The mask is moved into position with X, Y, and θ micro-manipulators. The vertical/horizontal strips on the right side are used for X-Y alignment and the 2nd and 3rd lines on the left are use for θ alignment.

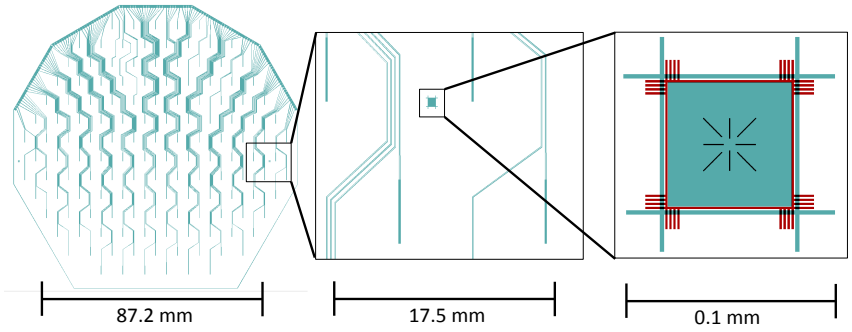

Figure 3.5: A CAD diagram illustrating the gcaws to ksaligner alignment. The ksalinger contact mask (Left) has two alignment marks spaced precisely to match the standard alignment marks of the gcaws. The two alignment marks printed by the gcaws (shown in red) align neatly to the marks printed on the mask. The location of each mark on either side ensures that there is good θ alignment.

the gcaws system to ensure sufficient alignment with subsequent layers. Since the

two masks expose the pattern on a single layer of photo-resist, great care is taken to ensure that no portions of the Nb leads are double exposed which would lead to opens in the wiring layer. Figure 3.6 shows how this mating is accomplished. The contact 'wiring' mask has short rectangle which mask the area that is exposed by the gcaws and the gcaws 'leads' mask only exposes a small region near the center of the pixel.

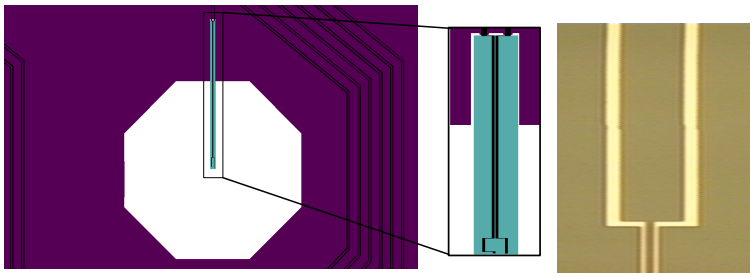

(a) CAD (b) Completed Etch

Figure 3.6: A CAD diagram illustrating simultaneous exposure of the Nb pattern using the gcaws to ksaligner. The ksalinger contact mask exposes everything except the black regions under the purple and the green region at the center of the pixel. Using the alignment procedure outlined in Figure 3.5, the gcaws then exposes the fine features near the center of the bolometer, but is masked off in the purple region to not double expose the bulk of the Nb wiring.

At this point, the wafer still has visible alignment marks formed by the developed photo resist, but is not exposed in the rectangular regions masked by the contact mask. The Nb 'leads'[10] mask is loaded into gcaws initiate the exposure (see Figure 3.4) of this portion of the pattern. The fine tune alignment of the wafer to the gcaws is illustrated in Figure 3.7.[11] The each pixel location is exposed for 0.8 s and then undergo a 5 minute, 85°C post-exposure bake (PEB) before being developed using OPD-4262, a standard I-line photo-resist developer.

Nb Etching

These three steps complete the wiring layer lithography. In order to improve the quality of the NB layer and reduce the number of unwanted shorts between leads a

[10]'Leads' are meant to indicate the part of the bias wires that are with in the spatial location of the pixels and 'wires' are meant to indicated the bulk of the trance from the pixel location to the bond pad

[11]This fine-tuned alignment is used on all subsequent layers.

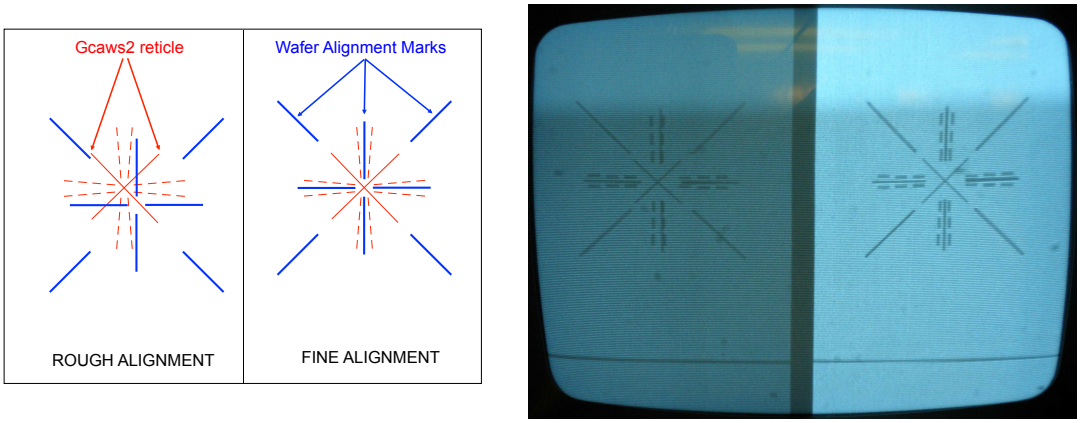

(a) Alignment Mark Diagram (b) Alignment Mark Photo

Figure 3.7: **Left Panel:** A diagram showing the layer-to-layer alignment system. The objectives of the gcaws system have alignment marks embedded in them (red). A set of alignment marks (blue) are printed on the wafer and align to the same two (fixed) marks for each subsequent lithography layer. **Right:** A photograph of the CRT monitor used to align the marks on the wafer to the gcaws system for layer-to-layer alignment. In practice X-Y alignment is done with the right hand set of alignment marks and θ alignment is done with the left hand set of alignment marks.

photo-resist 'descum' process is run.[12] The quality of the photo-resist post-descum is visually verified prior to etching the Nb. The Nb is etched in the SEMI Reactive Ion Etcher system in the MNF.[13] An optical end pointing detection system is monitored to determine the length of the etch. A typical output is shown in Figure 3.8.

The wafer is visually inspected to ensure the Nb etch is complete. The photo-resist is then stripped using a 30 minute soak in an 80°C PRS-3000 bath, a QDR, and an SRD cycle. At this point the wafer should be open circuits (as the circuit is completed with the placement of the TES at the end of the leads). The leads are inspected from shorts that can result from unwanted particles masking the etch between leads. The rate of occurrence of shorts was typically 1 to 2%.

[12]Descum process is done in the Plasma-Thermal Parallel Plate Plasma Etcher system. Base pressure is 3-10 mtorr, a flow rate of O_2 at 100 sccm for a process pressure 100mtorr, and 50 W RF power for 1 minute.

[13]Nb etched at a base pressure of $\leq$ 14, flowing 100 sccm of CF_4, 8 sccm of O_2, and 100 W of RF power

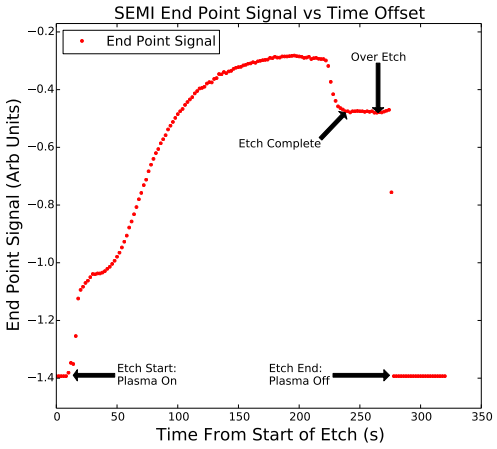

Figure 3.8: A typical outpoint of the SEMI end point detection system during an Niobium etch. As the niobium etch progresses more of the CF_4 Nb etch product is released in the chamber increasing the signal. As the etch finishes the signal drops to a constant residual value which indicates that the CF_4 is beginning to etch the SiN below the Nb layer. A 10 to 15 second over-etch is typically done to ensure a complete etch without significantly etching the SiN below.

.

3.2.7 Nb Oxide Removal

The wafer is now ready for deposition of the Al-Ti TES. However, a native layer of Nb Oxide, which is a strong electrical insulator at cryogenic temperatures, forms on the leads when they are exposed to atmosphere for more than a few minutes. To solve this issue the wafer is Argon sputtered etch just prior to the deposition of the Al-Ti bilayer.

Unfortunately this could not be done in a single vacuum step, because the CPA used to sputter the Al-Ti bilayer did not have any sputter etch capability. However, the load lock of the Gartek is equipped with sputter etch and is located roughly 30 feet from to CPA. Wafers were Ar sputter etched in the load lock of Gartek and transfered to the load lock of the CPA in 5-10s, which is not enough time for an insulating layer of Nb Oxide to form.[14] This step was a source of yield loss because the sputter etch would sometimes cause the wafer to debond if there was a small

[14]The sputter etch is performed with the Gartek system. The sputter etch is done at a base pressure of $1e-6$torr, at 8mTorr of Argon process pressure, and a 100 W RF power supply, which is well matched to the chamber (reflected power is typically 1-3%, for 5 minutes). The etch rate is typically 100 $\mathring{A}$ after a 5 minute etch.

pocket of air between the backing and device wafers.

3.2.8 Al-Ti Deposition

While the wafer is pumping down for the sputter etch, the Titanium and Aluminum targets are pre-sputtered at 110% of their deposition power for 5 minutes. The load-lock of the CPA is then isolated and vented in preparation for the sputter-etched wafer. Once the wafer is successfully sputter etched it is quickly transferred to the load lock of the CPA and immediately pumped down to base pressure. The Al-Ti bilayer is deposited sequentially beginning with the aluminum layer (which provides a hard etch stop and protect the Nb layer during the Ti etch) followed by the Ti layer.[15]

Critical Temperature Control

We found that the T_c of these Al-Ti bi-layers would very rapidly with deposition conditions, as such we attempted to normalize the process as much as possible so that we could modulate the T_c via the proximity effect by varying the thickness of the Aluminum layer [84]. Figure 3.9 shows scatter plots of T_c against the several process parameters. These deposition tests lead to the following requirements for the machine conditions: $0.8e-7 \leq P_{\text{base}} \leq 2.5e-7$, a minimum pump time of 30 minutes, a stable process pressure of 6mTorr, and a richly colored plasma observed during the pre-sputter. Furthermore we controlled the timing between the two metal layer steps to control for the thickness of Aluminum Oxide and the absorption of any other gasses. The wait time between the steps was controlled to be 90 to 110 s.

Al-Ti Etching

Once the TES bilayer is deposited it is ready for patterning and etching. An Al-Ti island is patterned using the gcaws. The Nb alignment markers are still visible under the microscope allowing a precision alignment of the TES to the Nb leads and subsequent layers. The wafer is coated with I-line and patterned using the gcaws system with a 1.2 second exposure. Finally the pattern is developed. The quality of the lithography is visually verified before the bilayer is etched.[16]

[15] DC sputtering done with CPA (Circuits Processing Apparatus, Inc.) 9900 track sputtering system. Deposition done at a base pressure of $\leq 5.0^{-7}$ Torr, 6mTorr Argon process pressure. Al deposited with 1 kW DC magnetron power with a 15 inch target with one pass at track speed of 35-48 cm/min. Ti deposited with 1.5 kW DC magnetron power with a 15 inch target with two passes at 31.3 cm/min).

[16] We skip both the post-exposure bake and the post-lithography descum step because the RIE for the TI has a 10% O_2 which clears away any unwanted photo-resist and the pattern is very large and is well resolved with a simple exposure and develop.

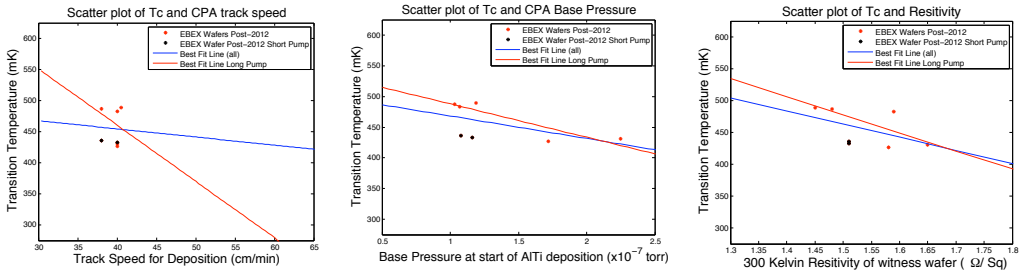

(a) Critical Temperature Vs. Track Speed (b) Critical Temperature Vs. Base Pressure (c) Critical Temperature Vs. Resistivity

Figure 3.9: **Upper Left Panel:** A plot of track speed (for Al deposition) vs. T_c **Upper Right Panel:** A plot of base pressure vs T_c. **Bottom Panel:** A plot of Resistivity vs T_c.

The Ti layer is etched first using RIE and followed by a wet Al etch.[17] Once the wafer is etched it the remaining photo-resist is cleared with an acetone soak followed by an acetone, isopropanol, methanol rinse and SRD. Figure 3.10 shows a wafer after the bilayer is etch but before the wafer is cleaned of photo-resist illustrating good alignment and electrical contact between the TES and Nb leads. The quality of the wiring layer is the inspected by testing continuity across each pair of leads to ensure good yield potential of the wafer. Wafers typically had 95%+ electrical yield at this point in the process.

3.2.9 Gold Web, Gold Thermal Link, and BLING

The wafer is now ready for gold deposition. However due to the low-G values of EBEX only a single gold layer is needed. However, the extra optical loading at the APEXSZ and ASTE sight requires increases G through the addition of a think gold thermal link along side the Nb leads. As the G is increased for this wafer another layer of Gold located at the center of the pixel, which we colloquially refer to as BLING. Each of the Gold steps are very similar except for the pattern, photo-resist thickness, and Gold thickness.

Gold patterning is achieved using a lift-off step which requires doing the lithography prior to metal deposition. The Nb alignment marks were protected during

[17]Ti RIE is performed in the Plasma-Thermal Parallel Plate Plasma Etcher system. Base pressure of 3-10 mTorr and process flow of 90 scm of SF_6/O_2 (90%/10%) mixture at an RF power of 100 Wfor 5 minutes, which is an over etch with hard aluminum etch stop. The Al wet etch is proceed by a 2 minute ultrasound in DI with 3 drops of Al wet etch as a surfactant to prepare the Al surface for etching. The Al is wet etched in once-prepared Al wet etch heated in a double boiler to 50°C for 40 to 60 seconds. Once the Aluminum etch is finished it is rinsed throughly with DI water to stop the etch.

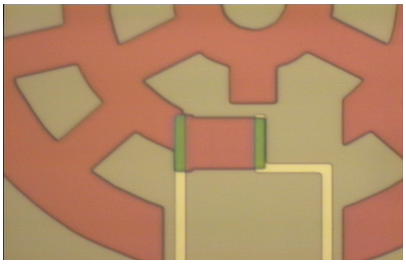

Figure 3.10: A photograph of the bilayer waffle-shaped structure just after the Al is etched. The gray area is silicon nitride, the red area is the bilayer coated with patterned photo-resist, and the white area is the Nb leads which are routed to bond pads at the edges of the wafer.

.

by the Al during the Ti etch and are used to align the gold layers to the Nb and Al-Ti layers. The thickness of the photo-resist is chosen to be at least 3x+ the thickness of the gold layer. For the Gold web and thermal link this only required 1.2 μm of I-line photo-resist and the Gold BLING for ASTE required 4.0 μm of g-line photo-resist.

The pattern is exposed with the gcaws stepper and developed with a 85 °C PEB and a standard track developer system. Prior to gold deposition, a descum process is run to clean the wafer of any residual photo resist to ensure excellent adhesion of the gold to the wafer. Between 200 $\mathring{A}$ and 1 μm gold is then deposited via e-beam evaporation on to the wafer using an 25$\mathring{A}$ evaporated layer of Ti as an adhesion layer.[18] The thickness is monitored using crystal monitor system. After deposition the wafer and crucibles are cooled for 5+ minutes.

The wafer is carefully removed from the chamber and placed in wafer carrier and submerged gold-side down into an acetone bath for an overnight soak (8 hours minimum). The next day the wafer is cleaned for 5 minutes in an ultrasound bath to clear away any unwanted gold that is still sticking to the surface of the wafer. The wafer is throughly cleaned with acetone, isopropanol, and methanol before it is finally rinsed clean in an SRD. Figure 3.11 shows a pixel just after the gold is patterned, evaporated, and lifted off.

[18] Au evaporated in the Davis & Wilder E-beam evaporation system. The evaporation is deposited at a base pressure ≤ 5e-6 Torr. The Ti is evaporated first at a e-beam current of 100-125 mA for a deposition rate of ∼1 $\mathring{A}$/s for a total thickness of 25 $\mathring{A}$. The Au is evaporated in the same vacuum step using a e-beam current of 100-125 mA or 150-175 mA for a deposition rate of 1-3 $\mathring{A}$/s and 4-8 $\mathring{A}$/s.

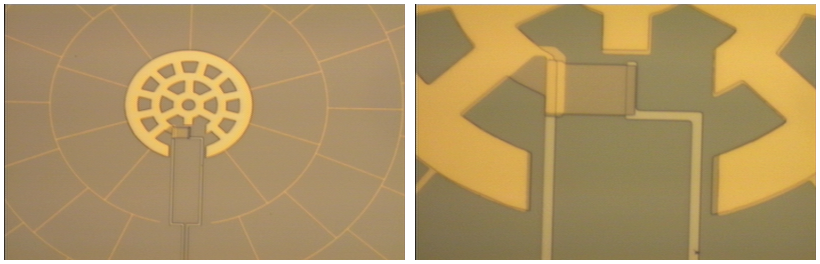

(a) 10X Magnification (b) 50X Magnification

Figure 3.11: A photograph of a pixel just after gold patterning, deposition, and lift-off.

.

3.2.10 Spiderweb Patterning and Etching

The final lithography is done to pattern the trenches in the LSSN to complete the formation of the gold-coated silicon nitride structure. The LSSN is 1 μm thick and requires a long etch. As such the LSSN is patterned using 2.0 μm of G-line photo-resist. The LSSN is patterned in the gcaws stepper using the same Nb alignment marks to align the patter to the 3 previous layers (Nb, Al-Ti, Gold). The typically alignment accuracy was about 0.5 μm. The pattern is double-developed after an 85°C, 2 minute, PEB and then hard baked at 85°C for 15 minutes to harden the photo-resist, which improves its ability to with stand wafer dicing, LSSN etching, and bolometer structure release.

The LSSN is etched carefully in two steps to avoid a over etching the wafer, which protects the photo-resist, which protects the Nb leads during both the SiN etch and bolometer release. The LSSN thickness is measured using a NanoSpec optical measurement system and an etch rate of 500$\mathring{A}$/s is assumed and the wafer is etched approximately half way through.[19] After approximately 8 minutes the wafer is removed from the chamber, the LSSN thickness is remeasured to calculate an etch rate. Using the etch rate from the first round of etching and the remaining thickness the etch time for the second round is calculated such that it will over etch 5% of the remaining LSSN. Once the etch is complete the wafer is ready for wafer dicing.

3.2.11 Wafer Dicing

The wafer must be diced into into its final shape out of the round 4 inch silicon wafer. Bonded wafers are fragile and much care must be taken during the dicing

[19]SiN RIE is performed in the Plasma-Thermal Parallel Plate Plasma Etcher system. Base pressure of 3-10 mTorr and process flow of 50 sccm of CF_4 mixture at an RF power of 100 W for 15-20 minutes, depending on the thickness of the LSSN.

process in order to maximize the chance of survival. Prior to wafer dicing the blade is throughly inspected for defects which may cause it to break during dicing. Furthermore the photo-resist used to pattern the SiN remains on the wafer to protect the bolometer structures. Any silicon dust from the dicing process will either be caught by the photo-resist or will land int the exposed silicon trenches left by the LSSN etch, where it will be quickly etched away during the bolometer release process.

The DISCO dicing system is then initialized and its condition is verified before it is configured for the specific job, which stores information about cut locations, orientations, and spacing, wafer size, and dicing parameters. A test cut at the edge of the wafer, where there are no pixels, is used to measure the offset between the blade and the camera in the system that results from using different blades in the tool. Each cut is manually aligned and verified prior to cutting to ensure no unwanted cuts are made.[20] The cut depth is set to leave about 200 μm of Si in the back wafer to minimize the kerf of the cut in the device wafer. This excess silicon is easily cleaved off and the wafer is thoroughly rinsed with water to clear debris and then blown dry with a nitrogen gun. The wafer is soft-baked at 85°C for 20 minutes to fully dehydrate it prior to releasing its spiderweb structures.

Figure 3.12: An EBEX array diced into its final decagonal shape for integration with the rest of the experiment

3.2.12 Bolometer Release

The final step to completing the bolometer array is to thermally isolate the spiderweb structures by etching the silicon away from beneath the silicon nitride leaving it suspended at the edges by its legs. This is achieved using a XeF_2 dry gas etch. Bare silicon is exposed during the silicon nitride etch which begins to etch away when it is exposed to XeF_2 at 35-45°C. During the this time a chemical reaction takes place

[20]The wafer is diced at 0.5 mm/sec at 30 krpm using a Keteca P/N K3T20L45 Silicon Dicing Blade, at a cut depth of 350 μm using the DISCO.

removing the silicon, once the XeF_2 is consumed by this reaction the contents of the process chamber are pumped out of the chamber and more XeF_2 is introduced into the etch chamber.[21]

The silicon needs to be completely removed from below the surface of the bolometer. The widest region of silicon nitride sets the total amount of silicon etch required to prevent any silicon pillars connecting the bolometer to the silicon substrate below from remaining after the etch, which introduces an unwanted thermal path from the bolometer to the wafer. Since the etch rate can vary from wafer to wafer depending on the condition of the tool, they are inspected for completeness using the Keyence digital microscope technology with precision metrology capability, which is illustrated by Figure 3.13.

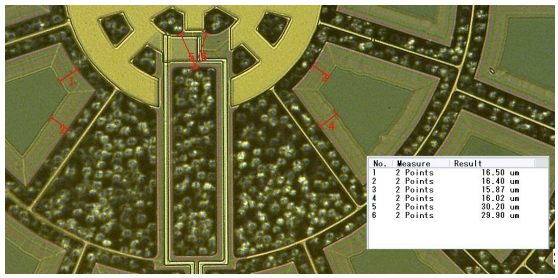

Figure 3.13: A photograph illustrating the process of verifying a bolometer release. The total amount of bolometer release is measurable using an optical microscope because Silicon Nitride with Silicon beneath it appears much darker. The widest region of the silicon nitride is measured (measurements 1 and 2) and then two other regions measure the amount of completed edge (measurements 3, 4, 5, 6).

This process requires high etch selectivity between Silicon and Silicon Nitride which can vary with the conditions of the wafer and the tool. If there is any water left on the wafer it can react with XeF_2 to form hydrochloric acid with is an etchant of Silicon Nitride. Furthermore the etch produce of the Si – XeF_2 also etches the silicon nitride membrane, which holds up the structure. A low quality release process will etch away the silicon nitride and reduce the integrity of the gold web as well as change the conductivity of the Silicon Nitride legs.

3.2.13 Photo-resist Ash

The remaining photo-resist layer provides necessary protection to the bolometer during the release process. The Niobium is quickly etched by XeF_2 so it is es-

[21] The release is done in the X-etch system using 100-120 cycles of filling the etch chamber to 3.5 mtorr and exposing it to the gas for 10 seconds before evacuating the etch.

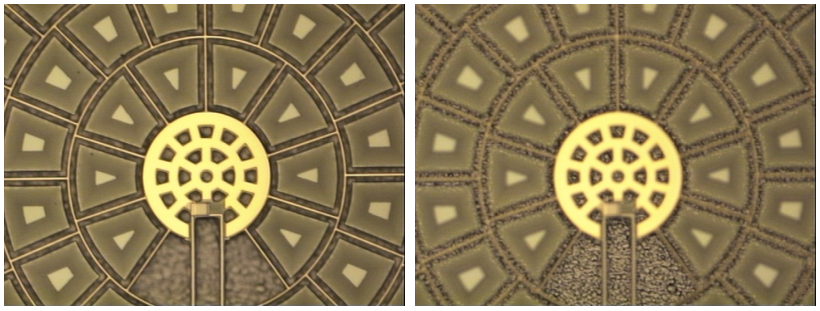

(a) Focus on Bolometer (b) Focus on Silicon Beneath Bolometer

Figure 3.14: Two photos showing a release bolometer structure with different microscope focus points for the bolometer structure and the silicon below it.

sential that the photo-resist layer remain in tact during both of the two previous steps.[22]

3.2.14 Wafer Inspection

Once the wafers are completed a series of room temperature measurements is done in MNF to determine the quality of the wafer and if it is worth cooling down to cryogenic temperatures for complete characterization.

Electrical Inspection: At the completion of fabrication the electrical yield is tested to ensure it is worth taking the time visually inspect and eventually test in a cryostat for flight suitability. An IV probe station provides the ability to make 2 resistance measurements across the TES through the Nb leads. The total resistance of the leads plus the TES was between 5 and 70 kΩ for the shortest and longest leads respectively. An resistance values outside of the nominal range are marked as open or short depending the value and the result is then verified visually afterwards

Visual Inspection: A pixel by pixel inspection is performed on each wafer that successfully completes fabrication and has an electrical yield of 85%+.

[22]Photo-resist ash at a base pressure of ≤ 14, flowing 100 sccm of O_2, and 100 Wof RF power, for 1 hour and 15 minutes.

Chapter 4

Atacama Pathfinder Experiment - Sunyaev Zel'dolvich

4.1 Introduction

The Atacama Pathfinder Experiment - Sunyaev Zel'dovich (APEXSZ) project is a ground based mm-wave cosmology experiment designed to study galaxy clusters via the Sunyaev- Zel'dovich Effect (SZE) [80]. APEXSZ made observations of 43 galaxy cluster with and SZE sensitive instrument over the course of 5 years from 2005 to 2010 from the Chajnantor Plateau in the Atacama Desert in Northern Chile. The instrument deployed an array of 280 TES bolometers (operated at 275 mK) sensitive to 150 GHz radiation with $1'$ resolution and $22'$ field of view. It was the first experiment to deploy an array of superconducting TES bolometers for science observations and is considered to be a pathfinder experiment for subsequent SZ experiments such as ACT and SPTSZ [74, 77, 82]. APEXSZ publications include multi-wavelength analysis of the Bullet cluster, SZ-X-ray scaling relations, cluster profiles dynamics, and high-ℓ TT CMB power spectrum [9, 10, 30, 57, 69, 77].

4.1.1 Galaxy Clusters

Throughout cosmic history gravity has collected large groups of galaxies in massive dark matter halos that we call galaxy clusters. They consists of any where from tens to thousands of individual galaxies, Intra Cluster Medium (ICM) (hot gas interspersed between the galaxies), and a halo of Dark Matter (which makes up the majority of the cluster mass). The ICM contains the bulk of the baryonic mass in the cluster and is typically between 6 KeV (7×10^8K) and 15 KeV (2×10^9K) in temperature. Clusters typically take several billion years to form and are the largest gravitationally bound structures in the universe.

Their unique composition and size make them excellent probes of the composition and evolution of the universe as whole. Galaxy clusters are believed to have formed at a redshift of $\sim$2-6, about the time when dark energy overtook matter as the dominant form of energy in the universe. As a result the growth of structure (i.e. the evolution of the galaxy clusters) are sensitive to both the negative pressure exerted by dark energy, which depends on both the dark energy density and its equation of

state. Measurements of cluster number density also constrain matter power spectrum normalization and mass density of the universe. They also provide a wealth of information about the local environment and are used to study heat transport, magnetized plasma, evolution of galaxies in various environments, and cosmic circulation of heavy elements [28, 88].

4.1.2 The Sunyaev-Zel'dovich Effect

The Sunyaev Zel'dolvich Effect (SZE) is the inverse Compton scattering of cold CMB photons off of hot (relativistic) electrons trapped in the ICM and is depicted in Figure 4.1. Approximately 1% of CMB photons will scatter off of the ICM, which causes a spectral distortion (i.e. the SZE) of the CMB's 2.725K blackbody spectrum. This spectral distortion is shown graphically in Figure 4.2.

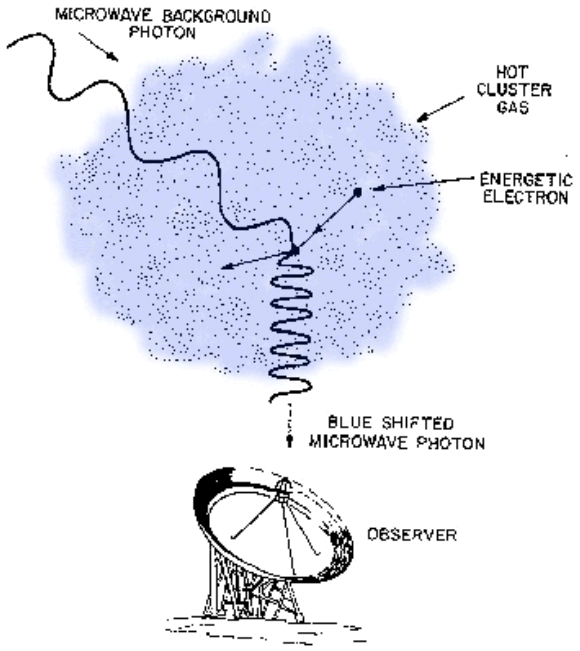

Figure 4.1: A diagram depicting an observation of SZE. Approximately 1% of CMB photons will Inverse-Compton scatter off of the relativistic electrons trapped in the hot ICM of galaxy clusters. Only those photons that scatter along the line of sight of the telescope can be observed.

Equation 4.1 shows the details of the SZE in terms of the cluster properties.

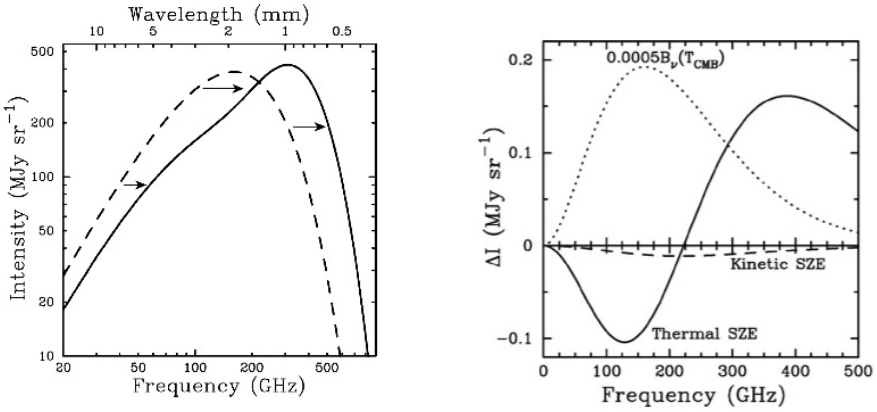

Figure 4.2: **Left Panel:** An exaggerated depiction of the spectral distortion caused by the blue-shifting of photons after their energy is boosted by Inverse Compton Scattering off of the electrons in the ICM. **Right Panel:** A graph of the spectral signature of the SZE between 0 and 500 GHz. The decrement (a deficit of photons) occurs at frequencies below 217 GHz and the increment (a increase in photons) occurs at frequencies above 217 GHz.

$$f(x) = (x\frac{e^x+1}{e^x-1} - 4)(1 + \delta_{\rm SZE}(x, T_x)) \tag{4.1a}$$

$$x = \frac{h\nu}{k_B T} \tag{4.1b}$$

$$\frac{\Delta T_{\rm SZE}}{T_{\rm CMB}} = f(x) \cdot \int n_e \sigma_T \frac{k_B T_e}{m_e c^2} dl = f(x) \cdot y \tag{4.1c}$$

Equation 4.1 demonstrates two important features of the SZE. First, the SZE is effectively redshift dependent because its a fractional change of CMB temperature, which originates at Z$\sim$1100. Second, the magnitude of the SZ effect at a given frequency only depends on the temperature and an number density of the electrons in the ICM along the line of sight and therefore gives a direct measurement of the thermal energy in the cluster.

The integral in Equation 4.1 the integral is along the line of sight of the telescope (dl). However, typically speaking clusters will also have an angular extent on the size which depend on its physical size and its redshift. Clusters typically have a radius of $1'$ to $8'$. In practice we map the value of y across the angular extent on the sky in the region of the galaxy cluster, which are originally discovered with X-ray, SZE, and optical survey experiments.

We then define the total Comptimization of the cluster, Y, to be the integral of the SZE over the angular extent of the sky.

$$Y = \int y d\Omega \tag{4.2}$$

The Comptonization, Y, measures the total thermal energy of the cluster. We expect it to be an excellent proxy for its total mass. Since the 'edge' of the cluster is ill-defined, we instead choose to integrate Equation 4.2 out to a radius of r_N (e.g. r_{500}, r_{2500}) which is defined to be the radius at which the average matter density of the cluster is N times greater than the critical density of the universe, $\rho_c(z) = 3H_0^2 E(z)^2/8\pi G$, where $E(z)$ is the expansion rate of the universe normalized to the present date vale $E(z) = H(z)/H_0 = \sqrt{\Omega_M(1+z)^3 + \Omega_\lambda}$.

4.2 Overview of the APEXSZ Experiment

The experiment is located on the 12 meter APEX telescope on the Chajnantor Plateau in Northern Chile. The Chajnantor Plateau is a premier sight for mm/sub-mm/wave astronomy because of its unique combination of high and dry conditions [68]. The focal plane of the experiment contains 280 spider-web absorber transition edge sensor (TES) bolometers readout with a cryogenic frequency domain multiplexing system. Three aluminum mirrors, two 4K lenses, and a horn array couple the detectors to the telescope. The experiments observes galaxy clusters at 150 GHz with $1'$ resolution ad $22'$ field of view, which was optimized for observing galaxy clusters via the SZE. A photograph of the telescope and receiver are shown in Figure 4.3.

4.2.1 Cryostat and Optics

All of the experiments on APEXSZ share at least 2 mirrors: the primary and secondary mirror of the APEX telescope. Depending on the location of a given experiment within the cabin (C-cabin, or one of two auxiliary cabins on either side of the C-cabin). A 'pick-off' mirror can be rotated into the beam bath to direct the incoming radiation to one the two side cabins. A tertiary mirror (called M3) which can be rotated between two fixed positions by hand or (via an remote rotation system) sits on the floor of the C-cabin and was used by APEXSZ. Two additional mirrors (called M4 and M5, respectively) redirect the incoming radiation into the window of the cryostat. The receiver (cryostat) is mounted in the main cabin where tertiary optics couple it to the telescope. A ray-tracing diagram of the tertiary optics is shown in Figure 4.4.

The incoming radiation is then coupled into the window of the cryostat through an aperture lens followed by an imaging lens and a Lyot Stop at 4K before it is coupled to the focal plane. The lenses are constructed with HDPE and have micro-machined groove which form an anti-reflection coating. The Lyot stop is 72 mm in diameter

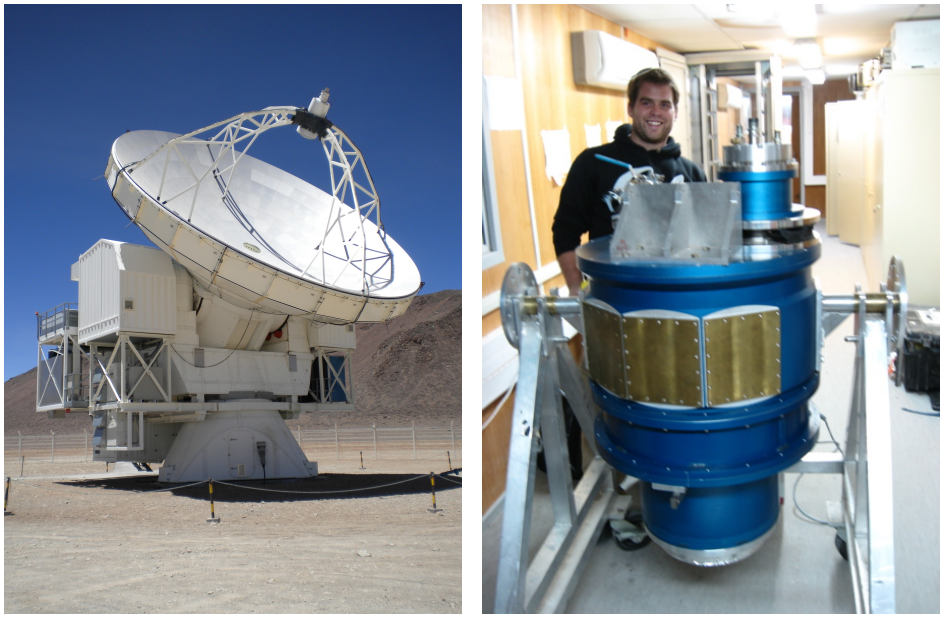

Figure 4.3: **Left Panel:** A photograph of the Atacama Pathfinder EXperiment telescope on the Chajnantor Plateau at an altitude of 5104 m. **Right Panel:** A photograph of me standing next to the APEXSZ cryostat at the control room just after finishing installing an upgraded focal plane.

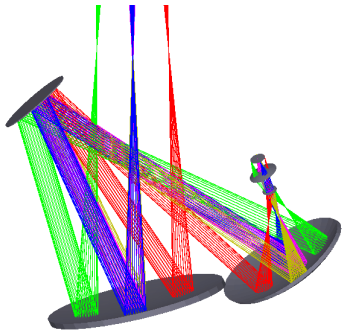

Figure 4.4: The APEXSZ re-imaging optics layout. Each bundle of rays represent the beam from a single detector. The tertiary mirror is M3, the folding flat mirror is M4, and the re-imaging mirror is M4.

and truncates to beam to immunization roughly the inner 70% of the primary mirror and provides $1'$ beams in the far-field limit for the experiment.

4.2.2 Integration Cavity

In addition to the beam forming optics there is also a series of filters, which reduce the load on the mK stage and minimize loading coming from outside of the APEXSZ band, which was designed to lie between Oxygen and water vapor atmospheric absorption lines at 118 and 183 GHz respectively. This provides a window to observe the SZ decrement near its maximum value at 150 GHz. The basics of the mK integration cavity is describe in the Chapter 2. A capacitive metal mesh filter is installed above the a horn array and is thermally sunk to the mK stage to provide an upper band defining edge at 177 GHz. The array is precision machined and gold-plated to provide a conical feed horn and a cylindrical waveguide which defines the minimum frequency of the observation band, which is 130 GHz for APEXSZ. The detectors sit in the optical integration cavity as shown in Figure 4.5. The spiderweb-absorbers were designed such that their resistivity matches the resistivity of the wave-guide in vacuum at 177 Ω.

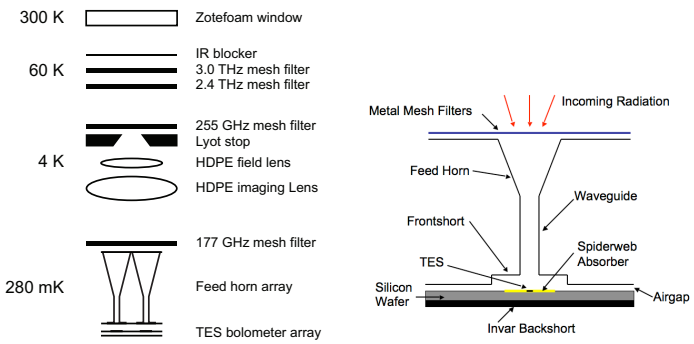

Figure 4.5: **Left Panel:** A schematic diagram showing the essential optical components inside of the APEXSZ cryostat showing the optical elements photons pass through before being coupled to the integration cavity. **Right Panel:** A cross-sectional diagram of the conical feed horn and cylindrical wave guide which form the integration cavity used by APEXSZ. The bolometers are lithographed on the front side of a $\lambda/4$ silicon backshort, which is mounted to a thick backing wafer and then mounted on to an invar plate (note the thickness of the focal plane arrays are drastically exaggerated). A cylindrical waveguide forms the lower edge of the detector bandwidths.

4.2.3 Focal Plane

The focal plane is constructed of six triangular shaped sub arrays mounted on triangle invar plates. The plates are mounted to an aluminum backing plane to form a large hexagon shaped focal plane containing 330 spatial pixel locations. However, due

Wafer Geometry	η_{cav}	Calculated $\delta\nu_{eff}$ (GHz)	Measured $\delta\nu_{eff}$ (GHz)	NET ($\mu K_{CMB}\sqrt{s}$
Perfect Cavity	1	37.6	...	...
$3\lambda/4$	0.72	32.3	24.5	530
$\lambda/4$	0.78	37.5	33.5	890

Table 4.1: Comparison of the APEX-SZ Detector Design Bandwidths

to readout limitations we could only readout 280 of these pixels, which is well matched to typical fabrication yield (see Chapter on Fabrication for a detailed description of the detectors). The performance of the detectors and focal plane is summarized in Table 4.1.

Upgrade to the APEXSZ Focal Plane

When APEXSZ was first commissioned its bolometers were fabricated using a $3\lambda/4$ design, which allowed the wafers to be fabricated without an initial bonding step (see Chapter 3). This reduces the overall optical efficiency and therefore increases the NET per detector as the $\lambda/4$ has high absorption efficiency compared to the previous $\lambda/4$ design. Figure 4.6 compares the spectral response of the two designs and Table 4.1 summarizes the quantitative differences.

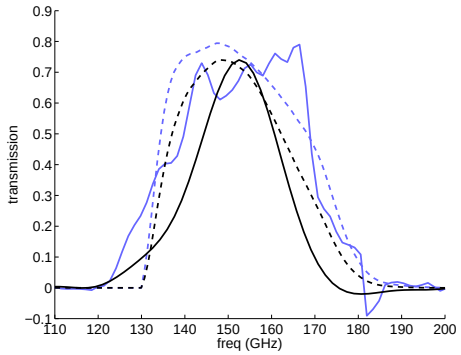

Figure 4.6: A comparison of the spectral bandwidth of the two detector designs deployed by APEXSZ. The solid lines represent actual spectral measurements and the dashed lines are the calculated transmission of the waveguides and metal mesh filters. The $\lambda/4$ and $3\lambda/4$ are blue and black respectively.

4.3 Overview of observations

APEXSZ completed a total of seven observation runs and two engineering runs between 2005 and 2010. The APEX telescope is a shared use instrument and the

APEXSZ experiment would get roughly 2-4 weeks per observation campaign.

During this time, we observed a total of 42 clusters spread over a total of ∼760 hours. These clusters were largely selected in an ad-hoc fashion with the exception of the REFLEX-DXL survey, which has a well known selection function. All of the clusters observed are organized in Table 4.2 and are depicted in a postage stamp style collection in Figure 4.7.

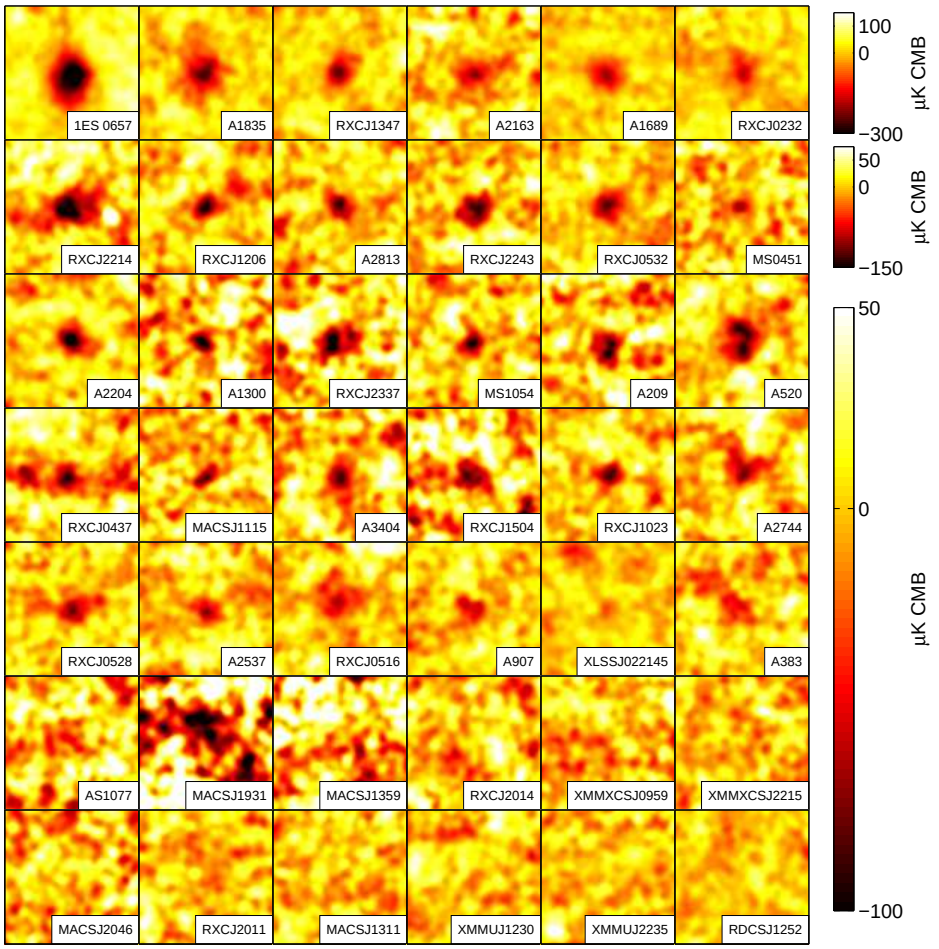

Figure 4.7: Maps of all of the clusters observed and analyzed by the APEXSZ team. They are ordered from highest to lowest signal-to-noise.

Prior to each observation run a team would fly to San Pedro de Atacama to prepare the receiver for the upcoming campaign. This generally required moving the receiver from its stow position to its observation position, run a number of health

Cluster Name	Right Ascension (h m s)	Declination ($^\circ\,'\,''$)	Redshit	Max Depth[a] (μK_{CMB})
Abell 2744	00 14 18.6	-30 23 15.4	0.307	12
Abell 2813	00 43 24.5	-20 37 31.2	0.292	21
Abell 209	01 31 52.6	-13 36 35.5	0.209	16
XLSS J022145.2-034617	02 21 45.2	-03 46 17.4	0.430	7
RXCJ0232.2-4420	02 32 18.8	-44 20 51.9	0.284	17
Abell 383	02 48 03.3	-03 31 43.6	0.187	14
RXCJ0437.1+0043	04 37 09.5	+00 43 54.5	0.284	14
MS0451.6-0305	04 54 11.3	-03 00 52.6	0.550	21
Abell 520	04 54 09.0	+02 55 18.0	0.203	14
RXCJ0516.6-5430	05 16 35.2	-54 30 36.8	0.294	10
RXCJ0528.9-3927	05 28 52.5	-39 28 16.7	0.284	11
RXCJ0532.9-3701	05 32 55.9	-37 01 34.5	0.275	16
Abell 3404	06 45 30.0	-54 13 42.1	0.164	13
1ES 0657-56	06 58 30.2	-55 56 33.7	0.296	19
Abell 907	09 58 21.9	-11 03 48.2	0.160	11
XMMXCSJ095940.8+023111.3	09 59 40.8	+02 31 11.3	0.720	14
RXCJ1023.6+0411	10 23 39.6	+04 11 12.0	0.291	12
MS1054.4-0321	10 56 59.0	-03 37 37.0	0.830	13
MACSJ1115.8+0129	11 15 51.9	+01 29 55.0	0.355	16
Abell 1300	11 31 54.7	-19 55 40.5	0.308	18
RXCJ1206.2-0848	12 06 12.3	-08 48 06.0	0.439	18
XMMUJ1230.3+1339	12 30 16.9	+13 39 04.3	0.975	11
RDCSJ1252-2927	12 52 54.4	-29 27 17.0	1.240	8
MACSJ1311.0-0311	13 11 01.7	-03 10 37.6	0.494	12
Abell 1689	13 11 29.3	-01 20 26.7	0.184	19
RXCJ1347.5-1144	13 47 30.8	-11 45 09.0	0.451	28
MACSJ1359.1-1929	13 59 10.3	-19 29 24.0	0.447	27
Abell 1835	14 01 01.9	+02 52 35.5	0.253	36
RXCJ1504.1-0248	15 04 07.6	-02 48 16.0	0.215	21
Abell 2163	16 15 46.0	-06 08 54.0	0.203	30
Abell 2204	16 32 47.1	+05 34 32.3	0.152	10
MACSJ1931.8-2635	19 31 49.6	-26 34 34.0	0.352	30
RXCJ2011.3-5725	20 11 27.1	-57 25 09.8	0.279	11
RXCJ2014.8-2430	20 14 49.7	-24 30 30.0	0.161	15
MACSJ2046.0-3430	20 46 00.5	-34 30 17.0	0.423	15
RXCJ2214.9-1359	22 14 57.4	-14 00 10.8	0.503	23
XMMXCSJ2215.9-1738	22 15 58.0	-17 38 02.5	1.450	11
XMMUJ2235.3-2557	22 35 20.6	-25 57 42.0	1.393	9
RXCJ2243.3-0935	22 43 21.4	-09 35 43.0	0.447	20
Abell S1077	22 58 48.1	-34 47 59.4	0.313	17
Abell 2537	23 08 22.0	-02 11 30.0	0.297	11
RXCJ2337.6+0016	23 37 37.8	+00 16 15.5	0.278	20

[a]: Map depth is measured within the central arcminute from the standard deviation of 500 jackknife noise map realizations.

Table 4.2: Clusters observered by APEX-SZ

and consistency checks, and cool the receiver down for observation. However, in 2009 the team performed an upgrade to the focal plane by replacing 2 of the 6 sub-arrays, which were constructed using a $3\lambda/4$ with sub-arrays fabricated using a $\lambda/4$ backshort design (see Chapter Detector Theory).

During a typical day during an observation run, a team would begin the daily observations by running a fridge cycle to cool the focal plane to $\sim$300 mK. Once cold the detectors are biased into their super conduction transition. At this point the receiver is tuned and the system is ready for observations. This tuning procedure take approximately 5 to 7 hours and must be repeated every day. We chose to tune receiver during the day time hours when the atmosphere was most turbulent. We typically yielded 160-180 bolometers on sky per night [30].

In a given night, clusters are observed according to a priority lists which we created based on the available clusters on the sky, observation elevation, and scientific interest. As clusters rise and fall across the sky, we executed circular scans centered on the cluster position and let the cluster drift through the FOV of the experiment. After 11 to 20 circles (depending on the circle radius) the telescope would recenter on the updated cluster position and begin repeating the circular scans. This process is repeated until the cluster is either too low in elevation to observe and/or a new higher priority cluster emerges in the night sky. Figure 4.8 shows an example of our cluster scan pattern for a fixed cluster position. In addition to the cluster scans we also performed nightly raster scans of a noise point source (such as Mars and Uranus) for temperature and beam calibration and sky-dips to get relative calibration between detectors to track gain drifts over the course of a given night.

4.3.1 Data Analysis

Data Cuts

The first step of data analysis is to eliminate those data which are known to be of no value to the final analysis. During observation we record data for all 280 of our available readout channels at a sampling rate of 100 Hz. However due to yield loss in fabrication, problems with cold wiring of the bolometers, and malfunctions in the squid operation we immediately cut those channels which we know are not active. In addition to this we make simple cuts on the overall responsivity of the bolometer to the calibrators. This tends to cut more bolometers on days with heavy optical loading. During typical days, 160-180 out of the total 280 bolometer channels remain after the initial data cuts.

The data are the decomposed into individual circle (sub) scans. We cut the roughly 7% of data at the start and end of a the unit scan where the telescope no longer maintains constant angular velocity. The data are then examined for electrical spike and cosmic rays which appear as glitches in the time stream, which results in a roughly 8% reduction in data. Finally we reject any detectors with excessive in-band

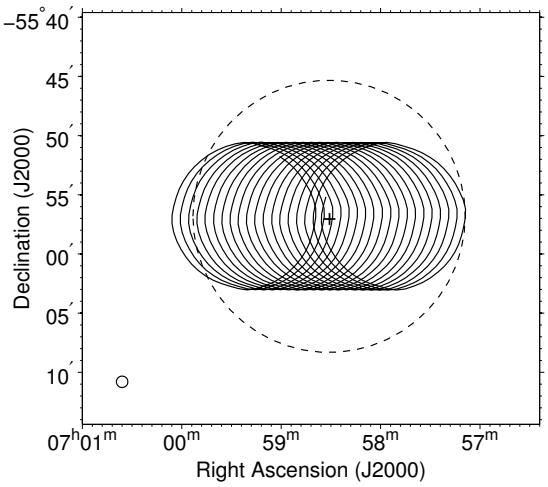

Figure 4.8: The scan pattern used by APEXSZ to observe clusters. The set of circles is called a unit scan and each individual circle is called a sub-scan. The dashed line indicates the instantaneous field of view of the instrument. The position of the cluster during the unit scan is denoted with a cross. The radius and duration of the circle was chosen to match the angular extent of the cluster and was typically 5-7′ in diameter and lasts 5-10 seconds.

noise, which results in roughly another 19% loss of data.

A fraction of the bolometers we used on sky were on able to be biased low enough in their transitions such that their responsivity is effectively constant in the presence of fluctuations of optical power, which arise excess airmass at low elevations, overall atmospheric opacity, and the flux from bright point sources [43]. Bright points sources causing gain fluctuations was rare and only affected our ability to use certain calibrators if they were too bright for calibration. The circular scan pattern induces a elevation dependent signal into each of the bolometers timestreams, which could be normalized to their response pointing at Zenith. Any detectors which exhibits non-linear behaviors is removed from the analysis so that the remaining channels response can be modeled as linear function of incident power.

Beams and Calibration

For each night of observation, we calibrate the pointing of the telescope, detector beam shape and size, and detector responsivity. The telescope pointing must be corrected over the course of the night due to slow variations in the telescope pointing accuracy which can broaden our effective beam width and increase our uncertainty in calibration measurements. Over the course of a night of observations we observe bright point sources such as quasars and planets to correct for telescope pointing

errors. Ideally we observe pointing calibrators that are as close as possible to the cluster we are observing to mitigate pointing errors further. We find that the RMS pointing errors for the APEX telescope to be $\sim 4''$ [30].

The beam shape and size as well as the responsivity of the detector is measured from raster scans of our calibrators: Mars, Uranus, and Saturn[1]. The far side-lobes of the beams are mapped individually for a small subset of the detectors are included in the final calibration calculation. The absolute flux calibration of the instrument is done by comparing the amplitude response of the detector to either Mars or Uranus. known celestial source a model of that sources brightness. For Mars we used the work of Rudy (1987), and Muhleman & Berge (1991) and for Uranus, we used the JCMT FLUXES applet available online[2] [73, 54]. At certain point during the observation campaign the primary calibrators were not available due to their close proximity to the sun. We used the stable H-II regions of RCW38 and IRAS12073-6233 as secondary calibrators by boot strapping the flux from back to back scans of the primary and secondary calibrators. Accurate calibration also required that we account for differences in atmospheric opacity, which is achieved by extrapolating the precipitable water vapor (PWV) measurements from the APEX radiometer to 150 GHz using the ATM model [61]. We estimate that the overall error in the calibration due to uncertainty in the beam solid angle, calibrator temperature, atmospheric opacity, and band center to $\pm 8\%$.

Timestream Filtering

Once the data have been cleaned of unresponsive, high-noise, non-linear, and low optical efficiency channels, they are filtered to remove unwanted fluctuations due to variations in the atmosphere and the temperature of the detectors and to correct for detector response delay by deconvolving the intrinsic time constant of the detector from the time stream. Both of these signals are well correlated across all channels. Two high-pass filters, a polynomial filter and a high-pass Butterworth filter, remove the arbitrary offset from the detector timestreams and cuts out any 1/f noise.

In practice the filters are applied iteratively. After the first high pass filter is completed, we perform a *spatial template removal*, which is a 2D spatial polynomial fit to either each sub-array or the entire focal plane, to remove any residual correlated signal between the detectors. Any channels that exhibit excess variance of the fit are discarded. Figure 4.9 shows the PSD of a bolometer timestream a three different stage of filtering: the raw timestream, after the initial high pass filter, and the fully filtered timestream.

[1]Saturn is used to measure beam shape but not to obtain absolute calibration.

[2]http://www.jach.hawaii.edu/jac-bin/planetflux.pl

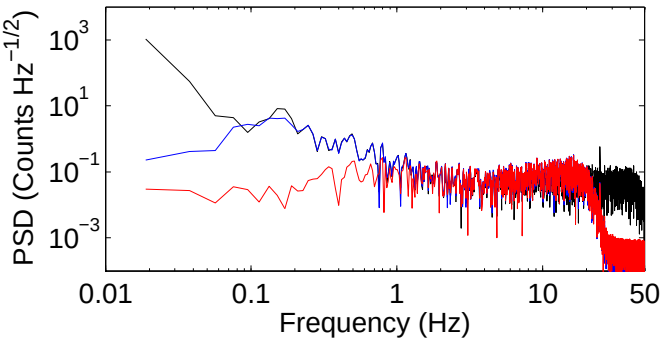

Figure 4.9: The power spectral density (PSD) of an APEXSZ timestream at three different stages of timestream reduction. The black line represents the raw data in units of readout counts. The blue line shows the power remaining after initial data cuts are performed, optical time constants are deconvolved, and a high-pass filter is applied. The decrease in low-frequency power is due to the high-pass step, whereas roll-off high-frequencies is a result of the low-pass filter included in the time constant deconvolution. The red line shows the power spectrum after spatial template removal and polynomial removal steps are performed, removing the remaining low-frequency contamination and completing the cleaning of the data.

Map Making, Transfer Function, & Noise Characterization

The each of the unit-timestreams are then mapped onto the sky using 10″ x 10″ pixels and are binned according the absolute bore-sight pointing of the APEX telescope and the detector offsets measured during the raster scans of the calibrators. The individual channel maps are co-added into the final map using a minimum variance weighting. All 42 of the APEXSZ cluster maps are shown in Figure 4.7. Those particular maps are smoothed with a 1′ Gaussian beam for presentation, but all fits and analysis of clusters properties are performed on the non-smoothed data.

The timestream filtering of the data also attenuates the signal from the galaxy cluster and the effects of the filtering process must be quantified to understand the *transfer function* of the analysis process. The transfer function is computed by running a simulated cluster (see Parametric Cluster Modeling) through the pipeline to measure the filtering effect on a known signal. The simulated cluster is convolved with the measured beam properties of the experiment and then reverse-mapped into the timestreams using the original pointing information used to construct the cluster map. The simulated timestreams are processed using identical data cutting and filtering that was performed on the cluster. A variety of simulated clusters are

processed through the pipeline to find that cluster model which most closely models our actual data after it has been filtered. We can now define a transfer function **K** for every cluster by normalizing the filtered cluster map back to the values of the simulated cluster which yielded the best fit.

Next we characterize the noise in the map by creating jackknife maps of our data by multiplying a random half of the data by -1 prior to co-adding them into the final map to remove any astronomical signals from the data. We add simulated CMB noise to the jackknife noise map by convolving a noise realization of the CMB from the WMAP7 best fit power spectrum, which is convolved with the transfer function in the same way a cluster is.

Parametric Cluster Modeling

There is no known way to model a cluster profile from basic physical principles (e.g virialization, gravity, etc.). As a result researchers have developed parametric models for the pressure (SZE) profile of galaxy clusters. We used the elliptical β model (Equation 4.3) to analyze the bullet cluster and the Arnaud universal pressure profile (Equation 4.4) for our analysis of SZE scaling relations.

$$n_e(r) = n_{e0}(1 + \frac{r^2}{r_c^2})^{-3\beta/2} \tag{4.3a}$$

$$\Delta T = \Delta T_0(1 + \frac{\theta^2}{\theta_c^2})^{(1-3\beta)/2} \tag{4.3b}$$

$$P_e(r) = \frac{P_0}{(\frac{r}{r_s}^\gamma)[1 + \frac{r}{r_s}^\alpha]^{\frac{\beta-\gamma}{\alpha}}} \tag{4.4}$$

These analytics equations provide a uniform framework for modeling and understanding many different galaxy clusters so that they can be compared with other observations (e.g. X-ray).

4.4 Point Source Contamination

The observation of a galaxy cluster is always constrained to be along the line of sight. Any astronomical object that is along the line of sight of the observation can have a significant impact on the measurement of the SZE decrement at 150 GHz. The two most common point sources of concern are bright radio points sources located with in the galaxy cluster and background infrared galaxies that lie behind the cluster. In practice we research the literature for published results of observations made near the locations of the galaxy cluster of interest. To check for radio point sources we extrapolate flux from the NRAO VLA Sky Survey at 1.4 GHz, VLA

FIRST at 1.4 GHz, and Parkes-MIT-NRAO at 4.85 GHz to 150 GHz by assuming a power law spectral energy distribution with a falling dependence on frequency. We chose to use $S_\nu \sim \nu^\alpha$ with $\alpha = -0.7$, which is a good estimate for synchrotron radiation coming from radio galaxies. Simulations suggest that approximately 1% of clusters will contain radio galaxy emission strong enough to have a significant impact on the SZE decrement at 150 GHz. We find that this method is sufficient to select galaxy clusters that will not have any significant contamination from point sources.

In several cases a lack of published data or doubt arising from a non-detection of galaxy cluster by APEXSZ required that we follow up our observations with observations of the same celestial location at frequency below for 150 GHz to check for radio point sources and frequencies above 150 GHz to check for IR points sources. The APEXSZ collaboration followed up on eleven of our clusters using the Combined ARray for Millimeter-wave Astronomy (CARMA) at 90 GHz and four clusters at 230 GHz through their public proposal system.

The data are collected by on-sight observers at the observatories once an observation planned is coordinated and uploaded by the APEXSZ team. Once collected the data are analyzed using the publicly available and documented MIRIAD software written for the CARMA array[3]. The software makes all of the necessary baseline, timing, and beam corrections and convert the UV coverage of the interferometer to an on-sky map. Figure 4.10 shows an example map of a detection and non-detection of a point source from CARMA observations. Table 4.3 summarize all of the follow up observations done with CARMA.

4.5 APEXSZ Observation of the Bullet Clusters

One of the most interesting clusters studied using the SZE is known at the Bullet cluster, which is undergoing a merger between a two smaller clusters. A particularly interesting aspect is that the merger is happening almost perfectly perpendicular to the line of sight of observations. The APEXSZ team did a detailed analysis of the Bullet cluster by comparing the observation of the cluster by APEXSZ to weak lensing and X-ray measurements [30]. Figure 4.11 shows a beautiful image of the Bullet clusters with data from X-ray (color map), weak lensing (green contours), and APEXSZ (white contours).

The Bullet Cluster is a unique astronomical laboratory as it is the massive merger of two galaxy clusters and has been studied by wide range of experiments (e.g. X-ray and Weak Lensing). However, the SZE flux measurement by APEXSZ represents the first published scientific results produced with an array of multiplexed superconducting spider-web absorber transition edge sensors [30].

[3]http://carma.astro.umd.edu/wiki/index.php/Miriad

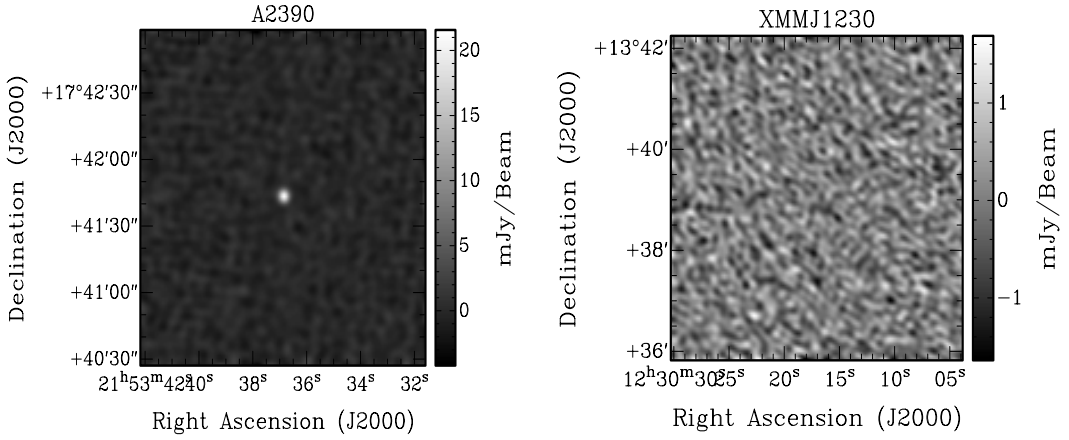

Figure 4.10: **Left Panel:** A map of Abel 2390 observed with CARMA at 3 mm. A 21 mJy point source is clearly visible and the map RMS is 1.7 mJy. **Right Panel:** A map of XMMJ1230 observed with CARMA at 3 mm. There is no point source detected in the map with an RMS of 0.4 mJy.

Combining the observations of the Bullet cluster using the SZE, X-ray, and weak lensing gives an exquisite picture of the dynamics of this particular cluster. The SZE and X-ray observations are most sensitive to the ICM of the galaxy cluster, while weak lensing measurements are most sensitive to the mass distribution of the galaxy cluster. As the merger happens the hot ICM of each sub-cluster will start to interact strongly through Coulomb forces, while the dark matter will only interact very weakly through gravity. As a result, the bulk of the dark matter will pass-through the merger while the ICM will collide at the center forming a shock wave. Figure 4.11 shows this clearly. The green contours are the peak weak lensing signals and clearly show two distinct clumps of dark matter while the SZE and X-ray measurements show that the gas in the ICM is clumped at the center of the merger.

The β-model is generally used to fit isothermal, relaxed (spherical) clusters, which are two conditions the Bullet cluster violates. However, the resolution and the depth of the APEXSZ observations allow the cluster to be modeled with sufficient accuracy for analysis of the cluster gas properties by comparing them to X-ray observations. We find that the mass-weighted temperature of the Bullet cluster is 10.8 ± 0.9 keV, which is on the lower edge of previously reported temperature for this clusters.

4.6 APEXSZ Scaling Relations

Since the distribution, mass, and number density of galaxy clusters depends on the underlying cosmology of the universe. The SZE can be used to understand the underlying cluster mass by studying a large group of clusters [10]. One method to

Table 4.3: Summary of APEXSZ Clusters Observed with CARMA

Cluster Name	ν_{obs}(GHz)	S_{rms} (mJy/bm)[a]	Point Source Flux	(RA, Dec)
Non-Detections				
XMMJ2235	90	0.9	N/A	(22:35:20.748,-25:57:45.00)
A2204A	90	0.7	N/A	(16:32:42.279,-05:34:38.75)
A2537B	90	0.7	N/A	(23:08:05.782,-02:13:59.33)
A520A	90	1.0	N/A	(04:54:01.505, 02:57:40.40)
A520B	90	0.4	N/A	(04:54:20.934, 02:54:55.70)
A1689A	90	1.5	N/A	(13:11:31.769,-01:19:34.57)
RXJ1504B	90	1.6	N/A	(15:03:43.972,-02:50:20.83)
XMM2215	90	1.5	N/A	(22:15:59.837,-17:38:09.42)
XMMJ1230	90	0.4	N/A	(12:30:17.517, 13:38:52.30)
A502B	230	2.5	N/A	(04:54:20.934, 02:54:57.70)
XMM1230	230	6.7	N/A	(12:30:17.517, 13:38:52.30)
XMMJ2215	230	6.2	N/A	(22:15:58.640,-17:38:04:00)
XMMJ2235	230	2.1	N/A	(22:35:20.748,-25:57:43.00)
PS-Detections				
A2390	90	1.7	21	(21:53:36.80, 17:41:43.63)
A2537A	90	1.1	5.2	(23:08:28.39, 02:02:38.18)
RXJ1504A	90	0.8	7.4	(15:04:7.50,-02:48:22.03)

[a]: For conversion between mJy and μK_{CMB} see Section 7.1 of the Appedix.

estimate the mass of galaxy clusters is to provide a scaling relation between the observable Y and the intrinsic cluster properties from the literature ($M_{\rm gas}$ and $T_{\rm X-ray}$, and $Y_{\rm X} = M_{\rm gas}T_{\rm X-ray}$). An accurate scaling value provides a simple, straightforward mapping from a readily available observable, Y, directly to the mass of the cluster through a power law scaling relation [37]. Given the assumption of hydrostatic equilibrium in the cluster we can define an unnormalized scaling between the observable Y and the underlying cluster properties shown in Equations 4.5

$$Y_a d_A^2 \propto f_{gas} T_e^{5/2} E(z)^{-1} \tag{4.5a}$$

$$Y_a d_A^2 \propto f_{gas}^{-2/3} M_{gas}^{5/3} E(z)^{2/3} \tag{4.5b}$$

$$Y_a d_A^2 \propto Y_X \tag{4.5c}$$

$$\tag{4.5d}$$

The relations are generally described by Equation 4.6

$$Y_{500} d_A^2 E(z)^{\delta} = A \cdot (\frac{X}{X_0})^B \tag{4.6}$$

For each of the galaxies observed by APEXSZ, we compute the Arnaud universal pressure profile to compute the cluster comptonization Y_{500} (out to a radius of r_{500}). These APEXSZ observables are compared with X-ray values of the cluster mass from literature. Specifically we find the scaling between Y_{500} against T_X, M_{gas}, and Y_X by fitting a power law to each of them using Equation 4.6. We use self similar values

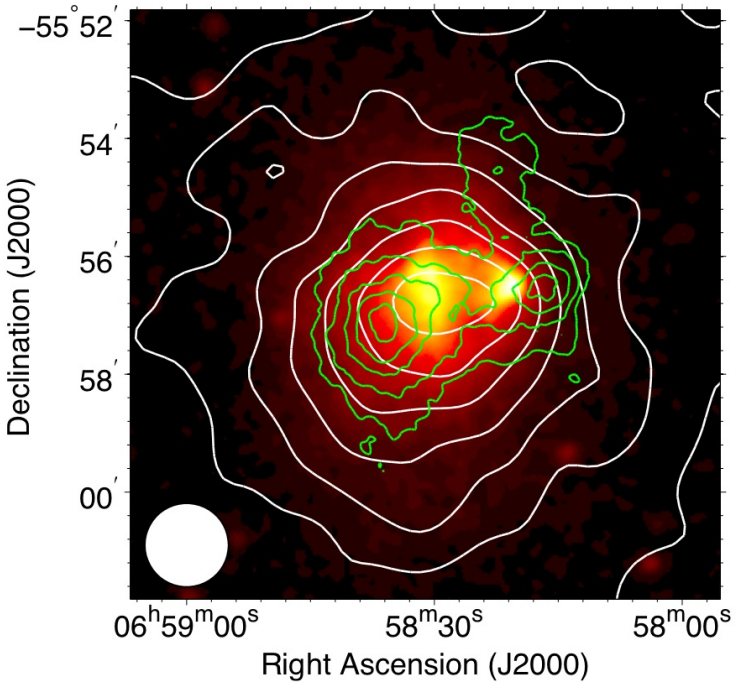

Figure 4.11: A map of the Bullet cluster with three data sets. The SZE observed with APEXSZ appears as the white contours, X-Ray data from XMM-Newton appears as the color map back drop, and the weak lensing data are displayed as green contours. The SZE signal is detected at 23σ within the central $1'$ of the map.

for δ of 1, -2/3, 0 and a pivot point (X_0) of $T_0 = 7.5keV$, $M_{gas,0} = 1.0 \times 10^{14} M_{\odot}$, $Y_{X,0} = 8.0 \times 10^{14} M_{\odot}$, respectively. The results of these scaling relations are listed in Table 4.4 and Figure 4.12.

Conclusions

The APEXSZ sample which includes the REFLEX-DXL luminous cluster sample was one of the largest of its kind at the time the result was published. We find that the scaling agrees very well with a self-similar model for the REFLEX-DXL sample for $Y_{500} - Y_X$, $Y_{500} - M_{gas}$, and $Y_{500} - T_X$. For the entire sample we find that our data indicates a slight preference for cluster models that include radiative cooling and feedback in the ICM of the cluster core. However, we find significant variations in the best fit power law values when dividing the full sample into sub-sets with uniform X-ray analysis. A uniform X-ray analysis of the cluster sample is on going, which will resolve the systematic limitations arising from non-uniform X-ray analysis.

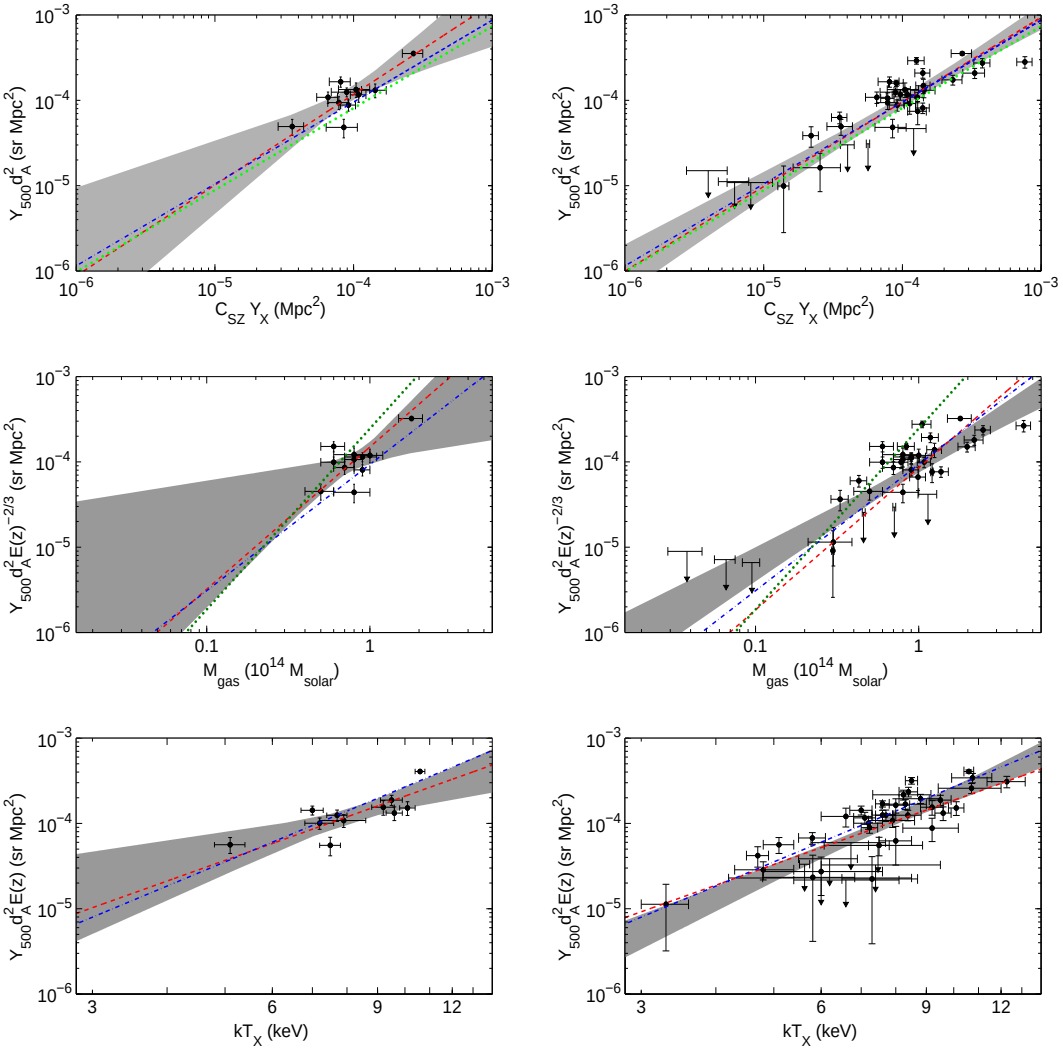

Figure 4.12: $Y_{500} - Y_X$, $Y_{500} - M_{gas}$, $Y_{500} - T_X$ scaling relations for the REFLEX-DXL (left column) and full (right column) cluster samples. The black points show the APEXSZ measured values given in Table 3. Non-detections are plotted as 95% upper limits. The shaded region depicts the 68% confidence interval of the power law for the three-parameter fit. Also shown is the maximum likelihood result for the case where the exponent is fixed to the self-similar value (red dashed). For comparison, we plot the best-fit results from PLANCK Collaboration XI (2011) (blue dot-dash), Plagge et al. (2010) (dark green dot), and Anderson et al. (2011) (light green dot).

Table 4.4: Scaling Relation Regression Parameters.

Subset	Full Fit $N_{\rm clusters}$	A[a]	B	$\sigma_{\log_{10}(\rm Y)}$	Fixed Exponent $N_{\rm clusters}$	A[a]	B	$\sigma_{\log_{10}(\rm Y)}$
				Y-Y_X				
REFLEX-DXL	11	$1.34^{+0.24}_{-0.13}$	$1.06^{+0.24}_{-0.32}$	$0.11^{+0.07}_{-0.05}$	11	$1.41^{+0.16}_{-0.16}$	1.00	$0.13^{+0.03}_{-0.06}$
All Clusters	35	$1.08^{+0.12}_{-0.08}$	$0.99^{+0.09}_{-0.08}$	$0.19^{+0.03}_{-0.03}$	35	$1.11^{+0.10}_{-0.10}$	1.00	$0.20^{+0.02}_{-0.02}$
Relaxed Only	17	$1.08^{+0.18}_{-0.18}$	$1.04^{+0.19}_{-0.23}$	$0.24^{+0.06}_{-0.05}$	17	$1.06^{+0.21}_{-0.16}$	1.00	$0.26^{+0.05}_{-0.06}$
Disturbed Only	17	$1.04^{+0.11}_{-0.11}$	$0.85^{+0.13}_{-0.10}$	$0.13^{+0.05}_{-0.03}$	17	$1.07^{+0.11}_{-0.12}$	1.00	$0.12^{+0.08}_{-0.01}$
				Y-$M_{\rm gas}$				
REFLEX-DXL	11	$1.35^{+0.22}_{-0.27}$	$1.07^{+0.52}_{-0.43}$	$0.15^{+0.08}_{-0.05}$	11	$1.50^{+0.22}_{-0.19}$	1.67	$0.13^{+0.03}_{-0.06}$
All Clusters	35	$0.89^{+0.11}_{-0.09}$	$1.14^{+0.14}_{-0.12}$	$0.24^{+0.03}_{-0.03}$	35	$0.85^{+0.09}_{-0.09}$	1.67	$0.23^{+0.02}_{-0.01}$
Relaxed Only	17	$0.95^{+0.17}_{-0.20}$	$1.38^{+0.27}_{-0.38}$	$0.28^{+0.09}_{-0.04}$	17	$0.95^{+0.20}_{-0.19}$	1.67	$0.34^{+0.05}_{-0.08}$
Disturbed Only	17	$0.87^{+0.11}_{-0.13}$	$1.13^{+0.16}_{-0.20}$	$0.21^{+0.05}_{-0.05}$	17	$0.80^{+0.14}_{-0.09}$	1.67	$0.23^{+0.03}_{-0.02}$
				Y-T_X				
REFLEX-DXL	11	$1.03^{+0.19}_{-0.13}$	$2.14^{+0.60}_{-0.78}$	$0.16^{+0.06}_{-0.04}$	11	$1.02^{+0.14}_{-0.13}$	2.50	$0.16^{+0.05}_{-0.05}$
All Clusters	42	$0.93^{+0.08}_{-0.09}$	$3.13^{+0.29}_{-0.34}$	$0.18^{+0.05}_{-0.03}$	42	$0.91^{+0.10}_{-0.09}$	2.50	$0.20^{+0.07}_{-0.02}$
Relaxed Only	20	$1.02^{+0.13}_{-0.18}$	$3.45^{+0.76}_{-0.49}$	$0.16^{+0.09}_{-0.04}$	20	$0.97^{+0.15}_{-0.18}$	2.50	$0.26^{+0.05}_{-0.06}$
Disturbed Only	19	$0.96^{+0.11}_{-0.11}$	$2.72^{+0.46}_{-0.42}$	$0.14^{+0.06}_{-0.03}$	19	$0.97^{+0.11}_{-0.10}$	2.50	$0.15^{+0.05}_{-0.04}$

[a]: The values of A presented in this table are in units of 10^{-4}.

4.6.1 Other Studies with APEXSZ

In addition to the three studies carried out with the APEXSZ dataset, we have also published results on the A2204 cluster, non-parametric modeling of galaxy clusters, and high-ℓ temperature power spectrum of the CMB.

High-ℓ Temperature Power Spectrum

The wide FOV, resolution, and sensitivity of APEXSZ at the time of its deployment provided the best constraints on the temperature fluctuations at small angular scales ($\sim 1'$). This study improved the constraints on anisotropy power at 150 GHz between the multipole range of $3000 < \ell < 10{,}000$ to be below 105 μK^2 at 95% CL [69]. At these angular scales it is expected that bright sub-millimeter galaxies and to a lesser extent secondary SZE anisotropies to contribute power at these angular scales. The study subtracted the expected SZE power spectrum and masked all known bright sources to compute the residual power, which we primarily attribute to bright sub-millimeter galaxies. In addition this study provided an additional constraint on $\sigma_8 < 1.18$ at 95% confidence by simultaneously fitting the SZE power spectrum with a Poisson distribution of point sources. Finally we compare a BLAST survey of this same patch at 600 GHz and conclude the spectral index ($S \sim \nu^\beta$) of $\beta = 2.6^{+0.4}_{-0.2}$ for dusty galaxies.

Non Parametric Modeling

Although parametric modeling provides a framework for comparing many clusters at the same time, it will always suffer from the systematic uncertainties and in

some cases the inability of a model to accurately extract the underlying cluster properties. By studying the high signal to noise detections of A2204 and A2163 made by APEXSZ, the collaboration was able to derive the radial temperature profile of the hot intra cluster gas out to a radius of r_{500} and beyond [9]. The study employed a non-parametric (aside from an assumption of spherical symmetry) de-projection method. The method was employed for both a relaxed (A2204) and a merger (A2163) system to demonstrate the difference in the ICM dynamics of these two types of systems. The study concludes that the gas temperature will decrease at the outskirts of the clusters. Furthermore the entropy as measured by APEXSZ within the central 100 kpc of the cluster can be used to determine the dynamical state of the galaxy clusters. Using the profiles measured using these methods we find that the total mass profile (assuming hydrostatic equilibrium) to be consistent with X-ray and weak lensing data.

A2163

Abel 2163 is massive galaxy cluster undergoing going a merger similar to the Bullet Cluster. A detailed multi-wavelength study of this merger system was performed using the data from APEXSZ (at 150 GHz) and LABOCA (at 345 GHz) [57]. A simple non-parametric de-projection of the radial temperature profile is used to measure the radial density of the hot ICM to measure the line of sigh bulk velocity and comptonization, which is consistent with published X-ray data. This study showed that simple joint SZE and X-ray analysis using the de-projection technique can be used for a wide range of dynamical cluster states.

4.7 Summary

APEXSZ underwent a successful observation campaign between 2005-2010. During that time APEXSZ observed 42 clusters, including the famous Bullet Cluster, and small patch of the CMB. It has published results on the dynamics of the Bullet cluster and A2163, high-ℓ temperature power spectrum of the CMB, a non-parametric modeling of clusters, and a robust scaling between Y_{500} and 3 X-ray derived proxies for cluster mass from literature.

It's rich dataset is still being analyzed to provide additional scaling relations between optical weak lensing data and a uniform X-ray analysis. Furthermore, it was the technological pathfinder for large arrays of superconducting TES bolometers readout using a frequency multiplexing scheme, which provided the foundation for SPT-SZ, ASTE, and EBEX.

Chapter 5

The E and B Experiment

The E and B Experiment (EBEX) is a long-duration balloon-borne 1.5m Gregorian-Mizuguchi-Dragone telescope experiment designed to make precision measurements of the polarization of the Cosmic Microwave Background (CMB) and the Cosmic Foreground. It observes the cosmos with ∼1000 detectors spread over three frequency bands centered on 150, 250, and 410 GHz with $8'$ at all frequencies. The project has flown its payload twice since first receiving funding in 2005. The first flight was an engineering flight launched from Fort Sumner, New Mexico in 2009. The second flight was a long-duration CMB observation flight launched from the Long Duration Balloon Facility (LDBF) in the austral summer of 2012-2013 [47, 71]. During the long-duration flight, EBEX observed roughly one sixth of the sky over an 11 day flight.

5.1 Science Goals

By the Austral Summer of 2012-2013 much high-quality CMB temperature anisotropy data had been collected and analyzed by wide a variety of experiments [5, 32, 74, 77, 82]. As such the primary goal of EBEX is to make a precision measurements of the polarization and of the CMB over a wide range of angular scales ($80 < \ell < 1000$). At large angular scales ($\sim 1^\circ$), EBEX is sensitive to B-mode polarization produced by primordial gravitational waves during inflation and at small angular scales ($\sim 10'$), EBEX is sensitive to B-mode polarization produced by gravitational lensing. These measurements can probe the energy scale of inflation as well as the growth of large scale structure throughout the universe's 13.7 billion year history. However, these measurements prove to be difficult since the magnitude of these signatures is predicted to be roughly 1 part in 10^7 of the temperature of the CMB.

Polarization Signature of the Primordial Gravitational Wave Background

The primary focus of EBEX and most other CMB polarization experiments is to detect the signature of the primordial gravitational wave background produced by the extremely rapid expansion of the very early universe known as inflation. Gravitational waves create quadrupole temperature anisotropies in the early universe

which impart both an E and B mode signatures onto the CMB. B-mode polarization anisotropy produced by inflation will peak at an angular scale of $\sim 1^{\circ}(\ell \sim 100)$, which was the size of the cosmic horizon at the time of inflation. A detection of excess B-mode polarization at this angular scale is considered 'smoking gun' evidence as inflation is the only known mechanism to produce B-mode anisotropy at these angular scales. The amplitude of the primordial gravitational wave background is parameterized by the tensor-to-scalar ration, r, whose value is proportional to the fourth root of the energy scale of inflation. *Therefore a high signal-to-noise measurement of the B-mode polarization constrains the energy scale of inflation and the fundamental physics that govern the universe.* If $r = 0.15$, detection of the primordial gravitational wave background requires measuring the polarization of the CMB to a depth of $\sim$100 nK over 400 square degrees [4].

Gravitationally Lensed B-mode Polarization

E-mode polarization created by monopole temperature anisotropies in the universe can be modulated into B-modes by large gravitational wells of intervening matter between the earth and the surface of last scattering. This signature is expected to peak at $10'$ scale where there is the growth of large scale structure peaks and is therefore distinguishable from the B-mode signature from primordial gravitational waves. The magnitude of the E to B mode mixing by gravitational lensing is highly sensitive to the large scale structure of the universe. As such measuring this signal probes the growth of structure which depends cosmological parameters such as the sum of the neutrino masses and the dark energy equation of state.

Characterize the Polarized Emission of Dust

Finally, EBEX provides a unique opportunity to measure the amplitude and polarization of the cosmic foreground, which is expected to be dominated by polarized emission from the hot dust in our own galaxy at frequencies above 150 GHz and synchrotron radiation at frequencies below 150 GHz. At the present moment the magnitude of the polarization of these foreground sources are poorly measured and could be a source of significant confusion of CMB polarization measurements [4]. The balloon-borne platform allows EBEX to observe at frequencies that are unavailable to ground experiments but are highly valuable probes of polarized emission of thermal dust from our own galaxy. The band centered on 250 and 410 GHz provide the ability to measure the spectral index of this emission, which is used to subtract out any contamination at 150 GHz.

5.2 Ballooning in Antarctica

Antarctica during the austral summer provides the ideal conditions for launching long-duration balloon-born experiments. For these reasons NASA has contract the

Columbia Space Science Balloon Facility (CSBF) to help launch science payloads from the LDBF, which is located in Willy Field seven miles outside of McMurdo Station Antarctica. NASA and CSBF have determined that ballooning in Antarctica in the austral summer is ideal for long duration flights.

5.2.1 McMurdo Station and LDB

McMurdo station is a location on Ross Island off the cost of Antarctica almost directly south of New Zealand. It is sponsored by the Unites States Antarctic Program and provides support for a wide variety of science year round. It is also location next to Scott Base, which is sponsored by New Zealand and similarly provides support to scientists. The LDBF was established in 1961 and has been used to launch science payloads since it's inception. Typically it supports three science payloads per year. LDB provides all of the necessary infrastructure required to integrate, test, prepare, and launch science payloads and support scientist. There are two large high bays with high capacity crane systems, massive helium storage, 2 high capacity mylar balloons per experiment, access to liquid cryogenics. Launches are executed from a large open 'launch pad' location about 1 km away from the high bays.

Once experiments declare 'flight ready' they are placed into a launch queue by CSBF. CSBF then closely monitors the weather to ensure that there are safe conditions for launch. Typically they require wind speeds to be stable and below 10 miles per hour. A photo of EBEX just before launch is shown in Figure 6.4.

5.2.2 Atmospheric Windows and Loading

Experiments which observe from the ground must look through the atmosphere in order to make observation. As such astronomers have searched for locations which have stable and highly transmissive atmospheric conditions, which generally only exist at high altitudes. The Chajnantor Plateau in Northern Chile and the South Pole provide the best condition for observing the cosmos in the mm/sub-mm regime on earth as both location are very dry (the Atacama and Antarctic deserts, respectively) and high altitude (16,500 and 10,000 ft above sea level, respectively). However, these locations still have to deal with significant atmospheric contamination in their data analysis [30, 64, 76].

Long duration scientific balloon payloads typically fly at altitudes between 110,000 and 120,000 feet in the stratosphere of earth, where the density of the atmosphere has fallen off considerably. This substantially reduces the optical load and allows the detectors to be optimized with much lower intrinsic noise (see Chapter 2) and has excellent atmospheric transmission at much shorter wavelengths.

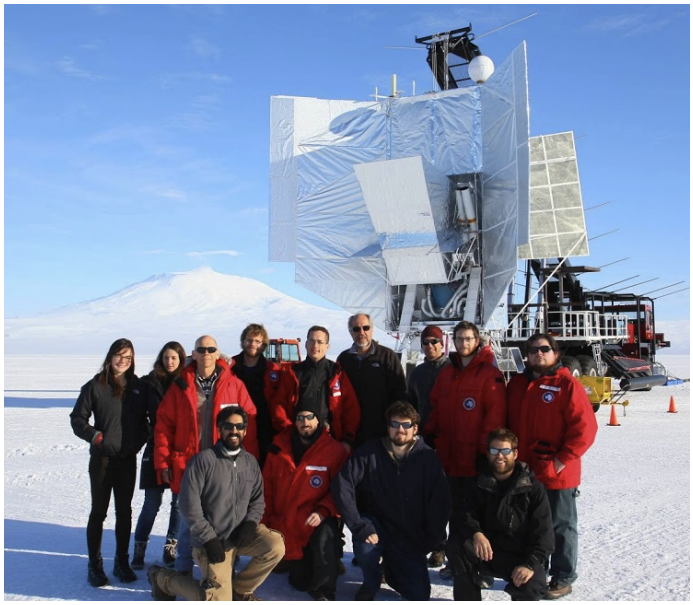

Figure 5.1: A photo of EBEX and some its core collaborators (from left to right: Kate Raach, Joy Didier, Shaul Hanany, Asad Aboobaker, Kevin MacDermid, Francois Aubain, Seth Hillbrand, Michele Limon, Kyle Zilic, Jeffrey Klein, Daniel Chapman, Benjamin Westbrook, and Michael Milligan) at Willy Field just before EBEX launched on December 29th, 2012

Atmospheric Loading

In addition to providing access to higher frequency windows a high altitude environment significantly reduces the optical loading on the detectors. A lower optical load on the detectors can drastically improve the noise performance on a individual detector basis, because there is significantly less noise contribution from the atmosphere, the voltage bias readout noise, and thermal carrier noise. These conditions mean that with a comparable detector count EBEX can achieve map noise levels with just 12 days of data as ground based experiments can achieve with 1 to 2 years of observations.

Atmospheric Windows

The first aspect of the highly transmissive atmosphere in a balloon environment EBEX takes advantage of the ability to observe at higher frequencies that are possible to observe on the ground. This give EBEX the unique advantage of measuring the polarization of the dusty foreground present in the EBEX observation path. The EBEX bands plotted against the atmospheric windows are show in Figure 5.2. By

placing bands at 250 and 410 GHz, EBEX can help constrain the spectral index of the thermal polarized dust and can provide accurate foreground models which can contaminate the CMB signal. Modeling and subtracting the foregrounds accurately is essential to recovering and accurately characterizing the polarization signals present in the 150 GHz channels (which most sensitive to the CMB). Atmospheric transmission simulations using the *am* software package from the Harvard-Smithsonian Center for Astrophysics for the South Pole, the Chancellor Plateau, and the LDB Facility high altitude locations are show in figures 5.2

5.2.3 Circumpolar Jet Stream

The final advantage of launching science payloads from Antarctica is the strong and consistent circumpolar jet streams that flow roughly concentrically around the south pole. The jet stream carries the balloon payload along roughly the same path in each line. Figure 5.2 shows the flight path of the long duration flight for EBEX Payloads typically complete a single lap in 10 to 25 days. The flight path for the EBEX LDB 2012-2013 flight is shown in Figure 5.3. This is essential to recovering the payload and the data from the experiment. Once the experiment returns back the ice shelf, CSBF does a controlled decent followed by a deployment of a parachute to drop the payload as close to McMurdo station as possible. A small team then takes twin-otter planes to the landing site to recover the most essential portions of the experiment. A photo of the recovery effort is show in Figure 5.3.

5.2.4 Constant sun and low diurnal temperature variations

Long durations payloads are only launched during the Austral summer. This is primarily because the summer in Antarctica also provides access to the sun 24 hours per day, which is essential to long duration payloads because they rely on solar panels to generate the electricity used to power the control, readout, and computer systems. At latitudes $\leq$ -75°, there is constant sun from November to February. Long duration payload experiments are typically designed to fly such that there is sun/back side and a anti-sun/front side. The solar panels are mounted on the back side and can continuously produce power during flight. Baffling and other shielding protect the primary mirror from coupling unwanted light from the sun and earth to the detectors.

We also must consider diurnal temperature variation for long-duration payload ballooning. As the temperature varies with the day-night cycle it cause the helium in the balloon to expand and contract, which will push a small amount of He out of the open bottom of the balloon The constant sun also reduces that amplitude of diurnal temperature variations which naturally arise from the day night cycle, which is helps keep the pay loads at high altitudes for longer periods of time. Payloads can stay a float for up to 2 months depending on the weight of the payload and the size

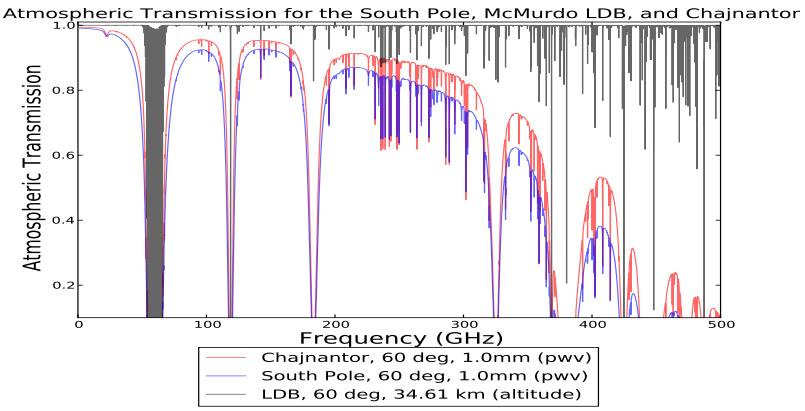

Atmospheric Transmission Comparison

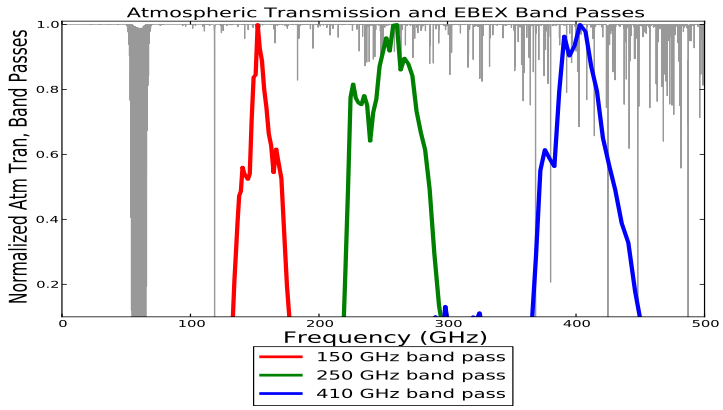

EBEX Bands and Atmospheric Transmission

Figure 5.2: **Top:** A comparison of atmospheric transmission for the South Pole (blue), Chajnantor Plateau (red), and a balloon pay load floating at 34.61 km (LDB Facility based high altitude balloon) sites. The high altitude balloon environment provides excellent transmission up to a 500 GHz compared to ground based sights which may be limited to observing frequencies at or below 320 GHz. **Bottom:** The EBEX bands over-plotted with the transmission of the atmosphere at 34.61 km above McMurdo station during the Austral Summer. Compared to the two best ground observation location on earth (Figure 5.2) we see significantly better transmission and optical loading for a high-altitude balloon.

of the balloon.

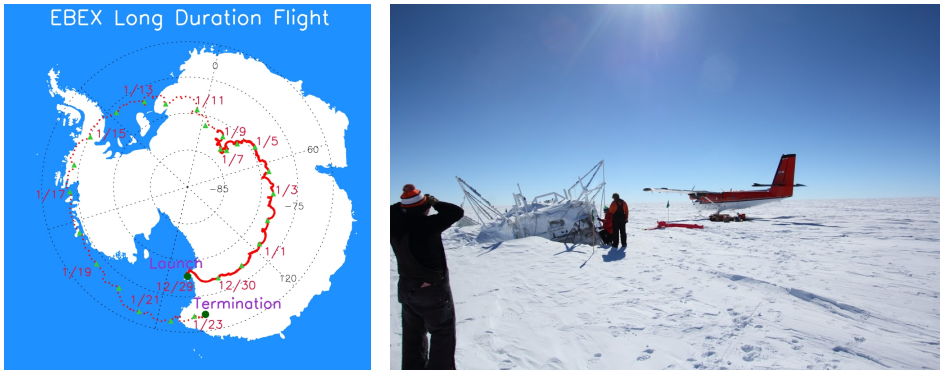

Figure 5.3: **Left:** The EBEX LDB 2012-2013 flight path. The bold lines indicate times when the cryostat was cold and we were taking data and the dashed lines indicate the time the payload was at altitude while riding the circumpolar jet stream to return to the recovery plateau a few hundred miles from McMurdo Station. **Right:** Photograph of the EBEX payload recovery effort taken by Asad Aboobaker. The cryostat landed on January 23rd and was recovered on January 30th, 2013.

Observe a Region with Low Galactic Dust

The spin axis of the earth, which defines the right ascension and declination coordinates, is roughly perpendicular to the plane of the galaxy. Long duration balloon experiments launched from Antarctic have access to low-dust (foreground) sky in the anti-sun direction. EBEX chose a patch of sky which is expected to have low foregrounds and good overlap with IRAS, PLANCK, QUIET, QUAD, BOOMERANG, and other CMB experiments. However, due to a failure in one of the pointing motor control systems, we used a fall back strategy that covered a much larger portion of the sky and have data on both high and low noise dust portions of the sky.

Recently BICEP2 published a detectiong of primordial B-modes in one of these low-dust regions [12, 4]. The fall back scan strategy has significant overlap with the BICEP2 patch is currently undergoing careful analysis by the EBEX team. Before EBEX many measurements of the polarization of the CMB had been made, but were only able to detect the so called E-mode polarization of the CMB, which is highly correlated with temperature anisotropies and is significantly higher in amplitude than the B-mode polarization.

In addition to the As such the community has spent much care and effort to design experiments with unprecedented sensitivity to polarization. The E and B EXperiment (EBEX) takes a novel approach to this challenge.

5.2.5 Scan Strategies: Primary and Fall Back

The primary scan strategy of EBEX was originally designed to observe the minimum patch size to resolve primordial B-modes while achieve sufficient map sensitivity to detect B-modes whose amplitude is 100s of nK given an 11 to 12 day flight. In addition the coverage is optimized to produce the largest possible area with uniform map depth. A plot showing the proposed scan strategy is shown in Figure 5.4.

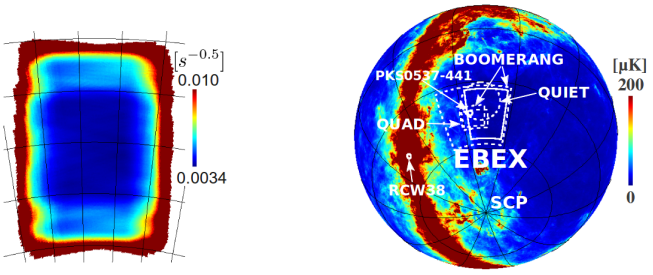

Figure 5.4: **Left:** A simulated map of the EBEX hit map sensitivity given the proposed scan strategy for an 11 day flight. The color bar is reported in units of $1/\sqrt{\text{time}}$ and is directly proportional to map sensitivity. The scan is optimized to maximize the area with uniform coverage and depth. However, due to the 6° FOV of the instrument there will always be a smaller sampling at the edges of the scanned region. **Right:** The white contour shows the location of the hit map shown in the left figure, which has good overlap with the BOOMERang, QUAD, and QUIET experiments (shown in white, dashed lines). In addition two bright calibrators, RCW38 and PKS0537-441 are highlighted with white circles.

Fall Back Scan Strategy

During the long-duration flight, EBEX experienced an unexpected failure in the pivot motor which controls the azimuth pointing of the experiment. We implemented a fall back scan strategy to let the gondola spin slowly in azimuth at a constant elevation. Due to sky rotation and the location of the gondola this strategy yield a 6000 square degree patch in a declination strip from -140 to -160°. Figure 5.5 shows the approximate hit map from the flight and typical azimuth pointing data.

5.3 EBEX Gondola and Payload

The 'payload' refers to the everything that is carried into the upper atmosphere by the high altitude balloon. A CAD drawing and photograph of the payload is shown in Figure 5.6. This figure highlights features of the power systems, readout electronics, baffling and shielding, mirrors, pointing sensors, and pointing control mechanisms. In addition, the cryostat can be seen sitting inside the inner frame

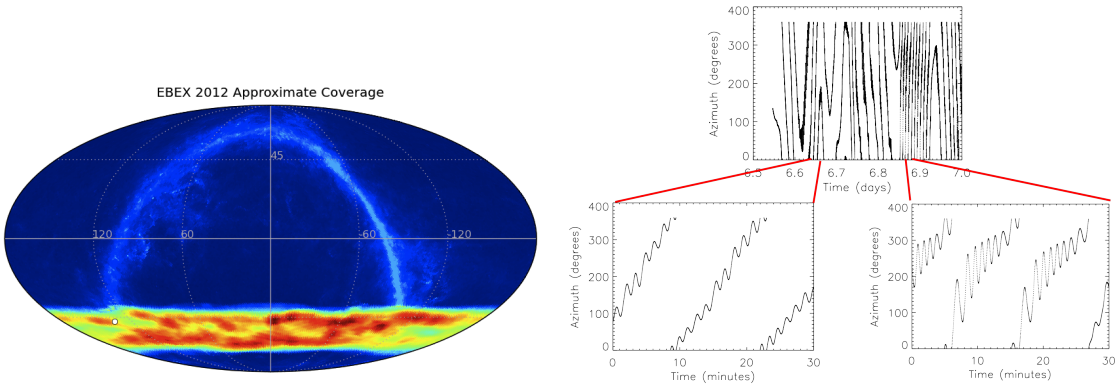

Figure 5.5: **Left:** A hit map of the EBEX coverage from the 2012-2013 flight. **Right:** Typical azimuth pointing data for the EBEX LDB flight. We lost explicit control of the azimuth pointing during flight. The fall back strategy scans kept the elevation constant as the azimuth continuously rotated with gentle oscillations on top of the global rotation.

of the gondola. The final weight of the payload before launch was 6,350 pounds and is currently the heaviest science payload to fly on a long duration high altitude balloon.

The experiment can be divided into two principal sub-systems, (1) Cryostat and Detectors and (2) Gondola and Pointing, each of which have many of their own complex subsystems, which were spearheaded by EBEX's many collaborators. The Attitude Control System (ACS), which includes all of the systems for pointing control and reconstruction was done at Columbia University. The bolometer readout (BRO) system and bolometer tuning software was spearheaded by McGill University. Design and construction of the cryostat and optical systems was largely done at the University of Minnesota. In addition to these subsystems the Liquid Cooling System (LCS) used to dissipate heat from the electronics was largely handled by Brown University. The thermal and optical filters as well as the anti-reflections coatings for the HWP and lenses came from work based out of Cardiff University. The development and fabrication of the cryogenic detectors was lead by UC Berkeley. I was principally responsible for the design and fabrication of the focal plane for the experiment. Each of the sub-systems (with the exception of detector fabrication, see Chapter 3) is described in detail in this chapter.

The EBEX mission was an engineering success. Not only did it advanced technologies that had been developed by a variety of previous balloon and ground based experiments [44, 77, 18], it was the first experiment to make observations of the CMB with continuously rotating HWP supported on a 4K superconducting magnetic bear-

ing, 16x frequency domain multiplexing factor, and a kilo-pixel array transition edge sensors on a balloon platform.

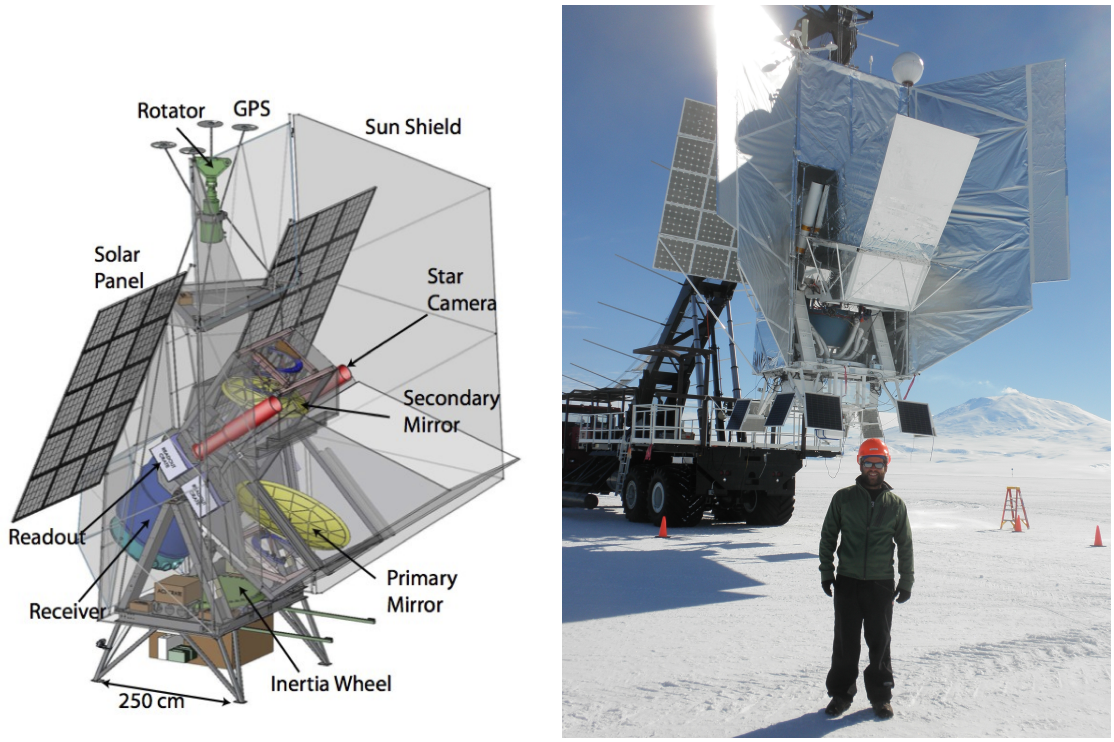

Figure 5.6: **Left Panel:** A SolidWorks model of the EBEX payload displays its major elements. Radiation from the sky is coupled to the receiver with the primary and secondary mirrors. An inertial wheel and pivot motor control the azimuth motion and a linear actuator (not shown) controls the elevation of the inner frame. Solar panels and batteries provide electrical power to all of the sub systems during flight. A large sun shield and scoop help reduce unwanted stray light coupling into the receiver. **Right Panel:** A photograph of the EBEX Payload just prior to its launch on December 2012 from McMurdo Station.

5.3.1 Power System

In order to operate the experiment remotely, the gondola must be equipped with it's own power generation equipment to power the various subsystems. In terms of power consumption we broadly divide the payload into two pieces. One of the power systems controls the BRO system, which provides bias voltages and currents to the detectors and squid amplifiers, readout boards to monitor cryostat temperatures, as well as readout and control from the HWP. The other power system controlled the

ACS (electronics, motors, and sensors), the star cameras and computers, as well as the flight control and data collection computers. The BRO system consumed about 50% more power than the rest of the electronic systems.

We designed the payload to have two sources of electrical power; solar panels and Lithium-ion batteries as back up. Each power system had it's own set of 15 solar panels covering a total of 8.6 m^2, with an average power generation of 76 W when orthogonal to the sun and operating at 110°C(no albedo). The power generated by these panels was routed to a TS-MPPT-60 charge controller which routed the power to the electronics and stacks of Lithium-ion batteries which had capacities 208 Ah and 144 Ah for the BRO and general electronics power systems respectively.

5.3.2 Pointing Control and Reconstruction System

The ACS is can be thought of as consisting of two main components: control and sensing. There many redundant sensor systems on the gondola which are used to accurately reconstructing the orientation of the telescope and the pointing of the telescope beam post flight, which are essential for reconstructing maps and polarization angles from the data.

Pointing is reconstructed post-flight by using start cameras and gyroscopes. At periodic intervals during flight two start cameras take high quality optical photographs of the sky which are capable of 'seeing' stars (even in the constant sun condition of flight). Each star camera image can be compared to an astronomical catalog and can be used to precisely measure the azimuth and elevation of the telescope at the time the image was snapped. After the image is taken the gondola and telescope will start to rotate as the scan continues. Three virtually orthogonal gyroscopes measure the angular velocity of the gondola, which can be integrate back the known location of the start cameras.

Accurately reconstructing the gondola pointing using this method requires detailed analysis and time which was unavailable during flight so we deployed several other course sensors including differential GPS, sun sensors, and magnetometers. These sensors provided real time pointing information during flight. Most of these sensors are highlighted in Figure 5.6

5.3.3 Optics

The design of the optical system for EBEX combines the research, development, and implementation of similar designs used by previous balloon (MAXIMA, MAXIPOL, Archeops) and ground-based experiments (ACBAR, POLARBEAR, APEX, SPT) [77, 44, 74]. The polarimetry is achieved with spinning half-wave plate (HWP) maintained at $4K$, which a technology originally developed for MAXIPOL [36].

A 1.5m primary mirror mounted in a Gregorian Mizuguchi-Dragone configuration provides an image of the sky at the window of the cryostat, which reduces the cross

polarization at the center of the image to be nearly zero. An imaging lens creates an additional image of the lens at the $4K$ Lyot Stop where the rotating HWP is located. This reduces noise from internal cryostat loading by ensuring that the beam's side-lobes are terminated on $1K$ surfaces and that each beam traverse the same portion of the HWP as the illumination is constant as a function of HWP position.

Once the sky image passes the Lyot Stop and HWP, a polarizing beam splitter (formed by a grid of wires) sends orthogonal polarizations to each of the two focal planes, which are mounted in horizontal and vertical positions which capture the transmission and reflection of the polarizing grid respectively. Figure 5.7

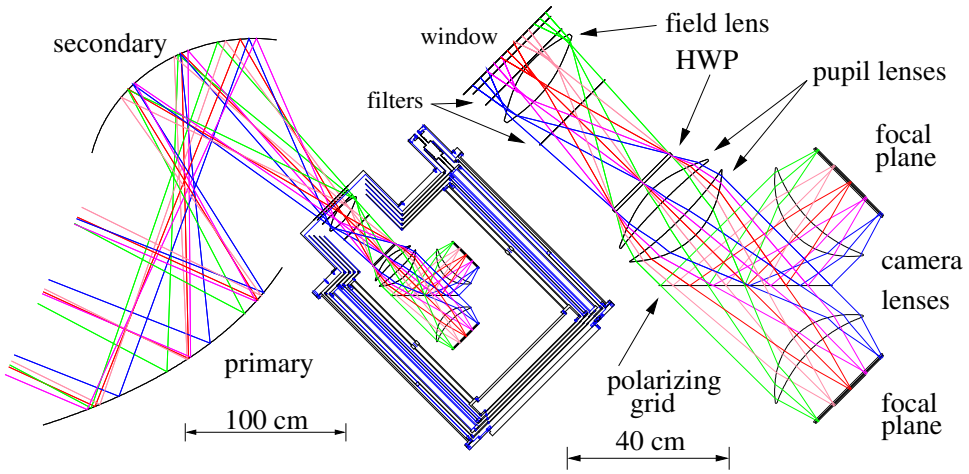

Figure 5.7: The ray tracing optics diagram for EBEX with a panel for the cold optics. The image of the sky is created at the window, HWP, and focal planes. A polarizing grid illuminates each focal plane with an independent polarization.

5.3.4 Cryostat

The cryostat is mounted to the inner frame of the Gondola as shown in Figure 5.6. The cryostat is cooled to 4K using liquid Nitrogen and liquid Helium as coolants. It is necessary to deploy liquid cryogens on a balloon payload, since there is not enough power generation to implement a closed cycle cooling system such as a pulse tube cooler (PTC), which are the preferred cooling method for ground based experiments. The optical design of the cryostat is engineered so that when it is roughly in a vertical position the window is at the top of the system, which allows gravity to hold the liquid cryogens inside of the stills.

Using common cryostat design techniques, the cryostat is cooled in stages to achieve cold 'main-plate' at 4 Kin the very center of the cryostat as shown in the Solid Works rendering of the cryostat in Figure 5.8.

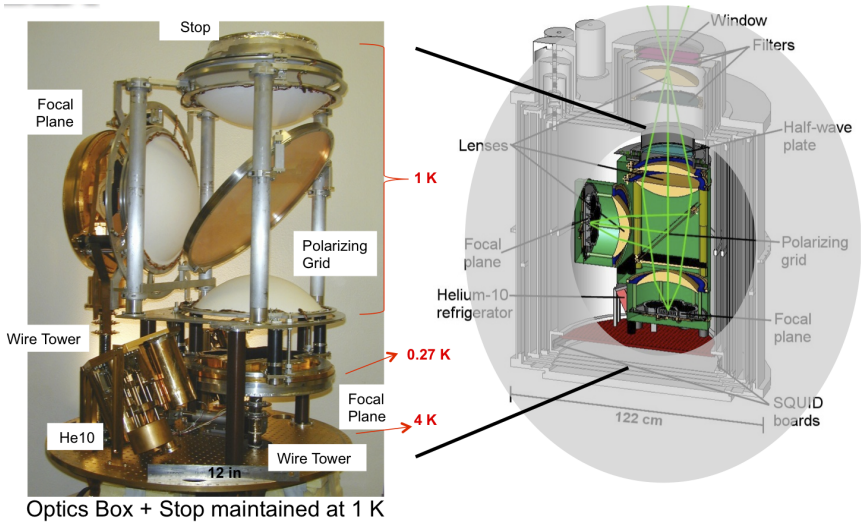

Figure 5.8: **Left:** A photo of the coldest elements in the EBEX cryostat. The optics box (lenses) are cooled to ∼800 mK using a 2 stage helium sorption fridge and the two focal planes are cooled to 275 mK using a 3 stage Helium sorption fridge. **Right:** A SolidWorks rendering of the inner-most (coldest) portions of the EBEX cryostat.

5.3.5 Bolometer Readout and Tuning System

The bolometer and SQUID amplifiers are controlled using the Digital Domain Frequency Domain Multiplexing (DfMux) readout system developed at McGill University for astronomy and cosmology applications [18]. A conceptual design of the readout system is shown in Figure 5.9. Each bolometer is represented as a variable resister in series with a LC filter, which forms a 'comb' of up to 16 detectors for each multiplexed module.

Liquid Cooling System (LCS)

Dissipation of heat generated by readout electronics is a unique challenge to balloon-borne experiments due to the lack of convective cooling and the need to consolidate space and weight. During peak operation when the SQUID amplifiers are tuned and operating and all of the bolometers in the entire focal plane are biased the total power consumed by the readout crates is 653 W (approximately 165 W per crate).

Custom heat sinks were installed on the DfMux and Mezzanine board which provided a strong thermal path from the highest power-consuming components to Oxygen Free High Conductivity (OFHC) Copper fingers which fight tightly into a radiator panel on the back of the BRO crates. Dynalene was flowed at 32 mL/s through

copper piping in the back plane and then through a series of Aluminum radiator panels which dissipate the heat via radiative heat transfer. The panels themselves are covered in a 250 µmthick layer of Fluorinated Ethylene Propylene (FEP) to increase it's emissivity in the infrared. During the long duration flight the LCS met it's design requirements and consistently kept the BRO crates well below 70°C.

Digital Frequency Domain Multiplexing System (DfMux)

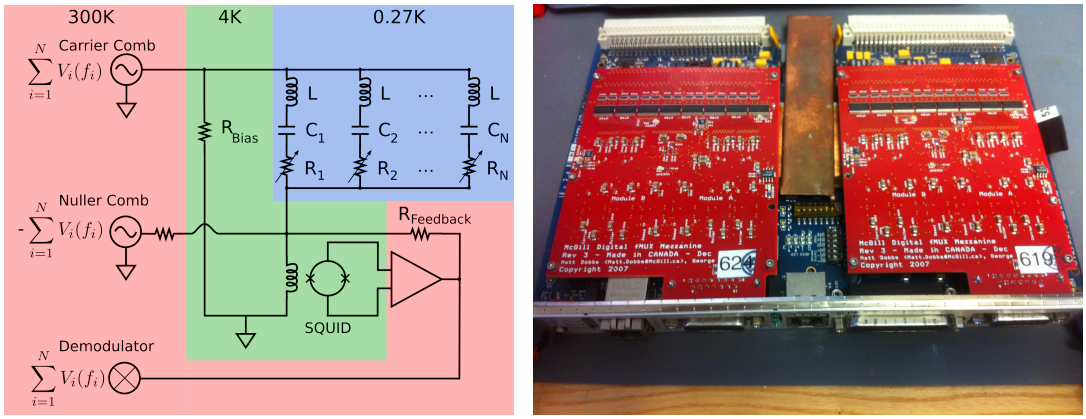

Figure 5.9: **Left:** A conceptual diagram of the frequency domain multiplexed readout circuit. The temperature of each section is indicated by its color. The bolometers are the variable resistors in the upper right, each forming part of an LRC circuit with its own unique frequency (typically between 300 and 1200 kHz). The "carrier" comb in the upper left contains a 'comb' (as seen in a network analysis) of sinusoids near centered on the resonant frequencies of each of these LCR filters (i.e. each bolometer). These sinusoids provide the AC electrical voltage bias for the bolometers. The "nulling" comb eliminates the bulk of the carrier current at the SQUID coil, to avoid non-linearities in the SQUID response. Finally, the "demodulator" separates the signal for each channel by multiplying by a sinusoid at each of the frequencies present in the carrier comb, low pass filtering and down-sampling the result. The carrier, nuller and demodulator operate at 25 MHz, the final down-sampled data rate is 190.73 Hz. **Right:** Photograph a DfMux (blue) with two Mezzanine boards, and copper thermal heat link installed, which generate the carrier, nuller, and demodulator combs shown in the red panel of Figure 5.3.5.

For each comb in the system we provide a unique frequency schedule so that each bolometer can be biased at it's own frequency allowing 16 bolometers to share a single pair of wires from 4 K to 275 mK . The voltage bias for up to 16 bolometers is provided by sinusoidal waveforms generated by DAC located at 300 K. The signals from each bolometer in the comb are summed at the SQUID input coil at 4 K. As the

resistance of each bolometer varies with the sky signal the carrier amplitude become amplitude modulated and appear in the sidebands of the carrier frequency. A nuller comb which provides the same 16 carriers but 180°out of phase with the original carrier signal will reduce the current at the input coil increasing linearity and gain, without altering the sky signal in the side bands of the resonant frequency of the LRC filters.

The actual hardware for the readout circuits are constructed on printed circuit boards (PCB) and surface mount components. Each mother boards has a FPGA capable of handling input command, executing tuning algorithms, and returning tuning information to the computer, which was essential to reducing the load on the flight computer and the overall power consumption of the experiment.

Each motherboard had two mezzanine circuit boards mounted to it which contain the ADC and DAC for the bias voltages as showing in Figure 5.3.5 (SEE Detector Theory for more information.) The mother boards are designed to have multiple boards plug into a common backplane for power, which consisted of regulated voltage at $\pm$ 6 V and $\pm$ 10 V, which is regulated down to $\pm$ 5 Vand $\pm$ 8 Von the motherboard. For the science flight we installed racks of DfMux boards into four crates (two with six boards and two with eight boards for a total of 28 boards). We label the crates BRO1, BRO2, BRO3, and BRO4 for simplicity. The power system was wired such that BROs 1 and 3 and BROs 2 and 4 each shared a common power source for their respective backplanes.

5.3.6 Focal Planes and Detectors

EBEX deployed an arrays of spider-web absorber transition edge sensors with sensitivity at 150, 250, and 410 GHz spread across two identical (in layout) focal planes. Each focal plane consists of 7 (4 150, 2 250, and 1 410 wafer per focal plane) decagonal wafers arranged in an hexagonal pattern as shown in Figure 5.10

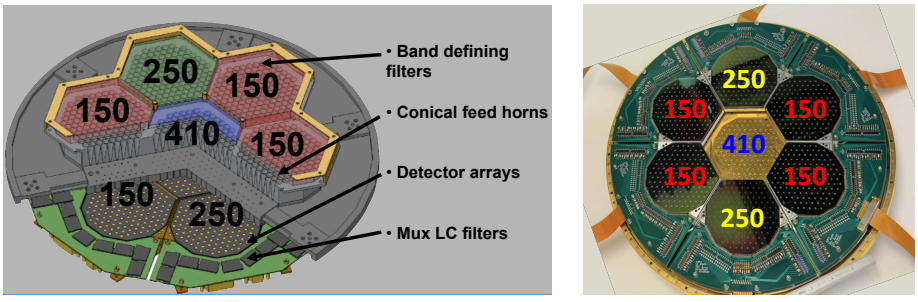

Figure 5.10: **Left:** A SolidWorks rendering of a single EBEX focal plane showing the integration cavity and LC readout circuits. **Right:** A photograph of the EBEX Focal Plane

EBEX employed a unique strategy to achieve the polarimetry by using two identical focal planes that are mounted in a horizontal and vertical positions as shown in Figure 5.8. This configuration greatly reduces the systematic error because each pixel gets an absolute measurement of the incident polarization for given HWP rotation angle. Other experiments, such as POLARBEAR and SPTpol difference the output of two orthogonal antennas to determine the polarization angle [74], which is prone to systematics arising from unequal gains between the antennas in the pair.

5.4 Preparation for the Science Flight

5.4.1 Engineering Flight Fort Sumner 2009

The EBEX team launched the experiment for a test flight on June 11, 2009 from Fort Sumner, New Mexico as an engineering and trial run as part of the lead up to the science flight in the winter of 2012-2013. The flight lasted about 14 hours, flew at altitude of 35 km, and covered a distance of about 300 miles. For this run one wafer at each frequency was flown and 64, 32, and 71 detectors were yielded at 150, 250, and 410 GHz respectively. All of the 250 and 410 GHz detectors were covered with a neutral density filter (NDF) built from MF-110 Eccosorb to allow for optical tests on the ground and a sub set of the 150 GHz also had NDF.

This provided many engineering milestones for the experiment. It was the first time that millimeter-wave TES bolometer and a SQUID based multiplexing readout were demonstrated in a space like environment and could be remotely tuned and operated from the ground station. In addition to this, this flight represents the first used of a broadband rotating HWP on a SMB. Furthermore the cryogenic and thermal performance of the cryostat was in line with pre-flight calculations. More information on the performance of the detectors, readout, cryogenics, and receiver housekeeping is available in Ilan Sagiv's dissertation [75].

5.4.2 Experiment Integration at Palestine

One of the most difficult aspects of pioneering new technology on balloon-borne platforms is designing and building the detector technology with no opportunity to test the system in it's final flight configuration. In order for the EBEX payload to be flight ready by both CSBF and internal standards it had to be taken to the CSBF site in Palestine, Texas to integrate the entire system and demonstrate that each of the sub systems is working properly. However, it is impossible to fully test the system as the conditions at float are impossible to replicate on the ground. The EBEX collaboration deployed to Palestine in the summers of 2011 and 2012 to prepare for the science flight in the Austral summer of 2012-2013.

5.4.3 Science Flight

Once the experiment passed the internal checks during the 2012 Palestine integration it was packed and shipped to McMurdo station in Antarctica. The first members of the team arrived in Mid-October to unpack and reintegrate the experiment in one of the two high bays at the LDBF. During the time leading up to launch day, the experiment was assembled and vigorously tested for integrity. The EBEX team launched the experiment for a 24 day flight during the Austral summer of 2012-2013 (see Figure 5.3), collected data for 12 days, recovered the data, essential electronics and payload. Since that time the team has been vigorously parsing, preparing, and analyzing this data.

During EBEX's science flight we were able to achieve close to nominal performance across our entire experiment. However, we do not expect to achieve the map sensitivity we predicted due to changes in the scan pattern and low duty cycle due arising from a problem with the pivot motor controller overheating. The overall experiment performance with an emphasis on the focal plane is presented in Chapter 6.

Chapter 6

Data Analysis and Flight Performance

6.1 EBEX Flight Overview

EBEX was successfully launched on December 29th, 2012 and subsequently flew around the coast of Antarctica for 24 days. The experiment collected data for the first 11.5 days before the liquid cryogens expired. All of the sub-systems deployed on EBEX performed as expected during the entire flight with the exception of the pivot motor which controls the azimuth of the experiment. The use of a fall back scan strategy compromised the experiment's ability to consistently generate solar power and impacted the effective duty cycle of data collection. Despite this, EBEX enjoyed many engineering successes. Most importantly the team successfully operated it's star cameras and other pointing sensors to accurately reconstruct pointing throughout the entire flight, operated a continuously rotating half-wave plate on a superconducting magnetic bearing for sky signal modulation, and operated a focal plane with approximately 1000 active bolometers. We are now constructing sky maps at 150, 250, and 410 GHz to study the polarization of the CMB and the cosmic foreground.

6.2 EBEX Data Overview

EBEX data set is about 1.5 TB, which is mostly time order data (TOD) from the bolometers, but also include TOD from the pointing and housekeeping system as well as discrete logs of the commands. The primary/raw data are separated into 4 distinct data types or 'vector bases:' Attitude Control System (ACS), Slow Streamer (SS or Housekeeping), Bolometer (Bolo), and half wave plate (HWP). Each vector base is written to its own set of complete dirfiles (each dirfile is referred to as a 'segment').

Throughout the flight we were unable to orient the experiment it's preferred direction with the primary mirror of the experiment staying in an anti-sun position and the solar panels staying in the co-sun position. This led to two issues which significantly impacted the EBEX duty cycle: the front side of the experiment experienced unexpected exposure to the sun and excess heating and the solar panels

were not constantly illuminated and therefore generated less power than expected. These two consequences of the fall back scan strategy required that we periodically turn of the flight computers to allow them to cool if the experiment spent too much time facing the sun, and that we only power a subset of the Bolometer Readout (BRO) crates to conserve power and ensure we could collect data while there were still cryogens.

Due to these issue with the pivot motor, the 11 day period of data collection is divided into 27 segments ranging from 1 to 24 hours long and contain a variable amount of data depending on how much of the experiment was powered during that portion of flight. During the data analysis, collaborators will build secondary data products 'on top' of the primary data, which are equal in length to the primary data, but also include some sort of post-flight processing. For example, a pointing vector base is built on top of the ACS base once the start camera and gyroscope data is analyzed and can be converted to a more convenient forms such as Right Ascension (RA) and Declination (DEC).

6.3 Data Cuts

Typically speaking, one of the first steps to analyzing large data sets for CMB experiments is to cut the data which will not contribute to the overall signal in the map. Non-contributing data exists for many reasons ranging from the bolometer not being properly tuned into its superconducting transition to the data responding poorly to the calibrator (i.e. low optical efficiency). The data cut work in this these focus on flagging periods of time where the bolometer is known to be tuned and the state of the housekeeping electronics is stable and within its nominal operating range. Analysis of more advance cuts on optical efficiency can be found in other EBEX papers and theses [47].

6.3.1 Bolometer Tuning and Retuning

Throughout the flight the EBEX team would operate the focal plane via remote commands to tune the detectors into their transition making them sensitive to light. The bolometer bias sequence is as follows. A cryogenic fridge cycle is completed such that the closed cycle refrigerator is capable of cooling the stage to its base temperature at $\sim$250mK. The bolometers are then heated above their superconducting transition temperature ($\sim$800mK) to ensure the TES is in a normal state. A large 'over-bias' voltage is applied to the TES which begins to dissipate heat in the TES. The focal plane is then cooled to its base temperature while the overbias keeps the detector at some temperature above its superconducting critical temperature. Once the focal plane is at base temperature the overbias voltage is incrementally dropped allowing the detector to slowly cool and gently drop into its transition. An algorithm will drop each detector to some fraction of it's normal resistance, which is chosen by

the EBEX operators to ensure the detector is sensitive and stable (typically 80% of $R_{\rm normal}$). If the detectors fail to be properly biased into their transitions we know that their optical efficiency will be suppressed and their response may be non-linear. Thus we chose to cut data from any bolometers which we know are not properly tuned for observation.

Tuned Time Analysis

The bolometers are tuned after each cryogenic fridge cycle which cools the focal plane to it's base temperature, because the fridge cycle disrupts the state of the SQUIDs and bolometers. In addition to fridge cycle events which require detuning the detectors we also had to remove bias when we were worried about power consumption in the readout crates. Other times we explicitly chose to overbias the detectors to improve the quality of the tune or to run atmospheric loading measurements at different telescope elevations. All of the events that change the bias state of the detectors are written to logs and algorithm returns on the flight computer, which allows us to reconstruct all of the times that a given bolometer was properly biased into it's transition. These time windows are converted to flags and written to dirfiles that align to the TOD bolometer data. Figure 6.1 and Table 6.1 summarize the integration time recovered by EBEX.

Table 6.1: A summary of the total integration time for EBEX 2012-2013 flight.

Frequency (GHz)	Optical Bolo-Hours Recovered	Yield When Readout Powered
150	26781	53%
250	19763	58%
410	5135	64%

6.3.2 SQUID jumps

The SQUID amplifiers used by EBEX rely on the fact that only integral magnetic flux quanta can permeate the loop of the SQUID illustrated in Figure 6.2. However instabilities in the temperature of the SQUID, variations in RF environment inside the cryostat, and spurious pickup by the SQUID or the bolometers can cause the SQUID to 'jump' from one integral flux quanta to the next which is undesired as it increases SQUID noise and reduces linearity.

When a SQUID flux jumps it's DC output will be offset by an integral multiple of $\pm$0.7V, which is written to disk as TOD. This TOD is then used to create a flag vector for each SQUID indicating whether or not the SQUID is a flux jumped state by flagging the times when the DC out deviates from 0 by a multiple of $\pm$0.7V. It is still possible to use data from bolometer's whose SQUID is flux-jumped, but it is

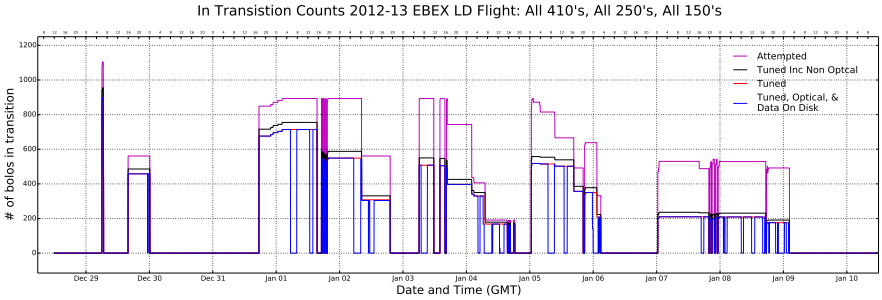

(a) Complete Timeline of EBEX Flight

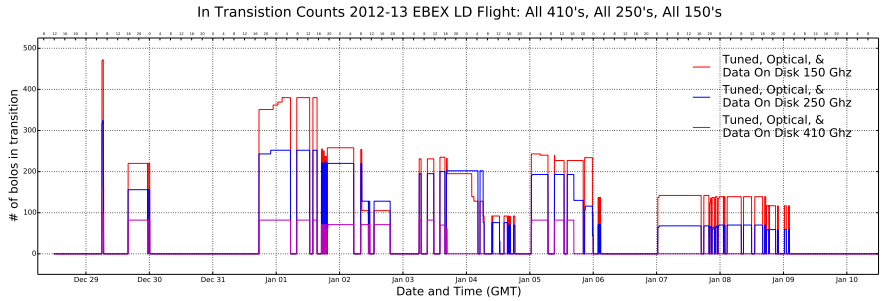

(b) 150, 250, 410 GHz Yield

Figure 6.1: **Top:** A timeline of the EBEX flight illustrating the times when our bolometers where properly tuned. The annotation tell the basic 'story' of the EBEX flight. The red and black lines indicates the times when we knew the bolometers (optical and all bolos respectively) were biased in the transition. The blue curve indicates the number of optical tuned bolos when at least one of the two flight computers was recording data. Therefore the integral of the blue line represents the total amount of bolometer data we collected during the flight. **Bottom:** A plot the recovered active time for each of the frequencies observed with EBEX. We yielded the most 150 GHz detectors. The 250 GHz detectors had the highest relative yield and the 410 GHz detectors had the smallest yield.

important to know when this occurs. A complete analysis of all of the SQUID data for flight indicates that the SQUIDs were in a flux-jumped state for less than 6% of the total observation time.

6.3.3 Timestream Glitches

It is somewhat common for bolometers to be sensitive to electrical pick up and cosmic rays which introduces sharp 'glitches' into the time ordered data. We know that these signal cannot be from the CMB because they occur two quickly given

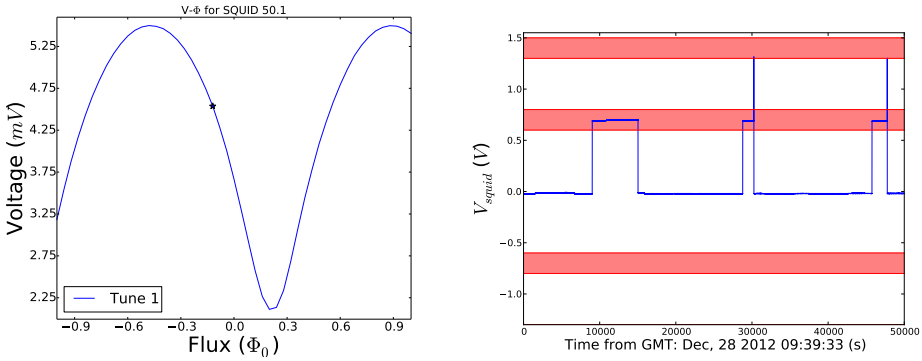

(a) Characteristic V-Φ curve of a SQUID

(b) Time Ordered SQUID data

Figure 6.2: **Left:** A single V-phi curve for a SQUID used in EBEX. The characteristic V-phi curve of the SQUID illustrating the optimal bias point (star). If the SQUID is disturbed is can potentially jump one full flux quanta to the next falling slope increasing the noise and decreasing the dynamic range of the SQUID. **Right:** Flux jumps are detected as large changes in the DC out of the SQUID. Multiples of ± 0.7V indicate a flux-jumped squid. The red regions indicate the expected output of a flux-jumped SQUID.

the bolometer's intrinsic time constant and the telescope scan speed. However, the presence of glitches in the time domain impacts the ability of algorithms to properly filter data and there for need to be removed.

Glitch Identification

EBEX accounts for glitches in the timestream by identifying them and then filling the time stream with simulated data in the time domain of the glitch so the resulting timestream is smooth and stationary. The identification algorithm works in the following way. The timestream is loaded to disk and a moving median with a 500 sample window is computed for each point in the time stream. The absolute value of the difference between each sample and the moving median (absolute deviation) is then computed at each point. Finally the median absolute deviation (MAD) is computed by taking the moving mean of the deviation within the same 500 sample window.[1] The value of the absolute deviations is compared against the median absolute deviation multiplied by a rejection factor. When the deviation exceeds the MAD times the rejection factor the sample is marked as a glitch and is other wise included in the data. Figure 6.3 illustrated how the absolute deviations, rejection

[1]For a Gaussian distribution the MAD is a factor of 1.4826 smaller than the standard deviation.

factor, and MAD determine which points are flagged by the algorithm. Once a glitch is identified, a small (0.1s) buffer is added to both sides of the glitch to ensure no spurious data is included in the final maps. Data on the left and right hand side of the glitch is used to estimate the local variance of the timestream and the flagged data is replaced with white-noise plus the baseline.

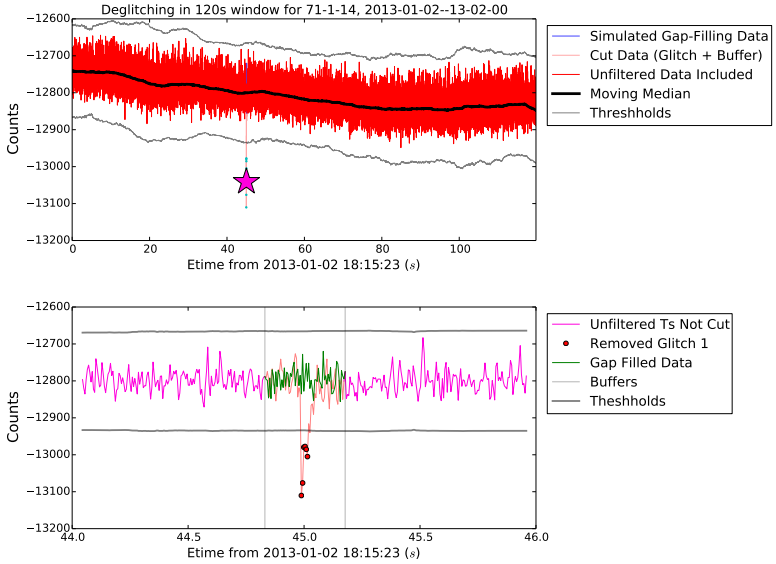

Figure 6.3: **Top:** A 120 second long timestream for a single bolo from the EBEX dataset (red) with the moving median (black) and glitch thresholds (gray) showing a clear cosmic ray glitch at t = 45s. **Bottom:** A zoom on the cosmic ray glitch at t = 45s. The red points are those flagged by the deglicther but a buffer is added to the glitch to ensure no bad data is included in data analysis. The green curve is simulated data that replaces the glitch to improve post-deglitching filtering.

6.4 Magnetic Field Pick Up in SQUIDs

Throughout the flight, the experiment would freely rotate around an azimuth axis while the orientation of the SQUID amplifiers was fixed with respect to the cryostat. As a result the relative orientation of earth's magnetic field to each SQUID as modulated by the azimuth of the experiment, which is seen in the TOD SQUID data as shown in Figure 6.4(a). The TOD data are then plotted against the gondola azimuth showing a clear sinusoid which is well fit by simple sine function as shown in Figure 6.4(b). The relative phase of the sine-wave fits are then used to recover the position of the SQUID with respect to the cryostat as shown in Figure 6.4(c).

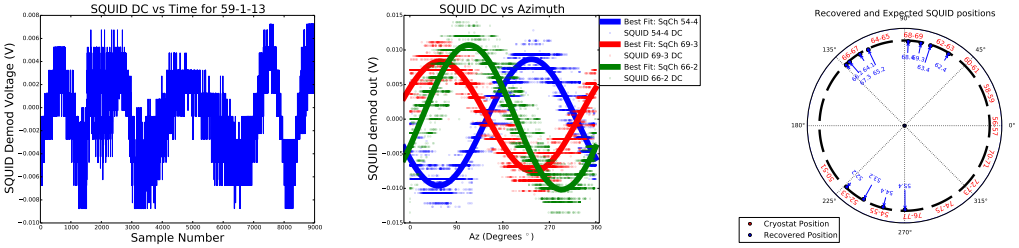

(a) TOD SQUID Data (b) SQUID DC vs Azimuth (c) Recovered SQUID Positions

Figure 6.4: **Left:** A plot of the SQUID DC voltage as function of time while the gondola was spun about it's axis and modulating the alignment of the SQUID to earth's magnetic field. **Right:** Three SQUID DC outputs plotted against gondola azimuth position. Each SQUIDs output is clearly modulated sinusoidally with azimuth. A best fit sine wave determines the phase and is used to receive the relative position of the SQUID in the cryostat. **Bottom:** A polar plot showing the expected and recovered positions of the SQUID from the magnetic field pick up. The positions of the SQUID are recovered to within 10°.

6.5 Summary

The analysis of the EBEX dataset is ongoing. Collaborators have made significant progress in the realms of signal and polarization calibration, pointing reconstruction, time domain signal processing, half-wave plate template subtraction, and map-making. These steps are being combined into a single pipeline which will start to make accurate polarization maps from our data, which will be used to estimate polarization power spectra in all three of the EBEX frequency bands. Data from the 250 and 410 GHz detectors will be of particular interesting the coming years to help understand the tension between the BICEP2 and PLANCK reports and will firm up our understanding of B-modes at large angular scales..

Chapter 7

Appendices

7.1 SZ and Point Source Flux

This calculation serves as means to translate the flux measured with the CARMA array to the SZE flux measured with APEXSZ. It assumes a spectral index of $\eta = -1$ for radio point sources and a spectral index of $\eta = 3$ for dusty IR point sources [87]. The gain factor, $G \equiv T_{\rm A}/S_\nu$, which is is defined as the ratio of APEXSZ antenna temperature, $T_{\rm A}$, and the CARMA flux, S_ν, is computed in the following manner.

Derivation

The derivation of the formula is described below. The power received from a point source with flux density S_ν (units: $erg * s^{-1} cm^{-2} Hz^{-1}$) is:

$$P_{\rm CARMA} = S_\nu * A_{\rm eff} * \Delta_\nu \tag{7.1}$$

The Nyquist power received in a single spatial mode, two polarizations received by APEX-SZ is:

$$P_{\rm APEXSZ} = 2 * k_{\rm b} * T_{\rm A} * \Delta_\nu \tag{7.2}$$

Equating this to the Nyquist power received in a single spatial mode, two polarizations, we get:[1]

$$2 * K_b * T_{\rm A} * \Delta_\nu = S_\nu * A_{\rm eff} * \Delta_\nu \tag{7.3}$$

where $T_{\rm A}$ is the RJ antenna temperature. Plugging into the definition of the gain factor we get:

$$G = T_{\rm A}/S_\nu = A_{\rm eff}/(2 * k_{\rm b}) \tag{7.4}$$

[1]Boltzmann Constant, $k_{\rm b}$, and the effective aperture, $A_{\rm eff}$, are in cgs units, (i.e. $k_{\rm b} = 1.38 \times 10^{-16}$ erg/K, and $A_{eff} \sim cm^2$)

Then to convert flux from CGS to Jy, one needs a factor of 10^{-23} in the numerator, since $1Jy = 10^{-23} erg{*}s^{-1}cm^{-2}Hz^{-1}$. Combining all of these equations, we get:

$$G = (10^{-23} * A_{\rm eff})/(2 * k_{\rm b})[K_{\rm rj}/Jy] \tag{7.5}$$

Again we note that $k_{\rm b}$ and $A_{\rm eff}$ need to be in CGS units when using this formula. Finally this is a formula for $K_{\rm rj}$ and we would like the formula to convert between Jy and $K_{\rm cmb}$. Since $K_{\rm cmb} = 1.71 K_{\rm rj}$. We simply multiply the above gain formula by 1.71. Thus we have:

$$G = (1.71 \times 10^{-23} * A_{\rm eff})/(2 * K_b) K_{\rm cmb}/Jy \tag{7.6}$$

For APEX-SZ $r_{\rm eff} = 400cm$, and $\eta_{\rm a} = 1$ (aperture efficiency for APEX-SZ). Thus,

$$A_{\rm eff} = \eta_a \times \pi r_{\rm eff}^2 = \pi \times (400cm)^2 = 5.03 \times 10^5 cm^2 \tag{7.7}$$

Thus the gain for APEX-SZ is:

$$G = 1 \times 10^{-23} \times 5.03 \times 10^5/(2 \times 1.38 \times 10^{-16}) = 0.0182[K_{\rm rj}/Jy] \tag{7.8}$$

or in CMB units:

$$\begin{aligned} G = 1.71 \times 0.0182 = 3.12 \times 10^{-2}[K_{\rm cmb}/Jy] \\ G_{\rm K2Jy} = 32.1[Jy/K_{\rm cmb}] \end{aligned} \tag{7.9}$$

Sanity Check

Sanity check: APEX telescope for heterodyne instruments, in which

$$A_{\rm eff} = A_{\rm physical} * \eta_{\rm a} = \pi * 600cm^2 * 0.60 = 6.8 * 10^5 cm^2 \tag{7.10}$$

Plugging this into our gain formula we get:

$$\begin{aligned} G = 1 \times 10^{-23} * 6.8 \times 10^5/(2 * 1.38 \times 10^{-16}) = 0.0246[K_{\rm rj}/Jy] \\ G = 1.71 \times 0.0246 = 4.21 \times 10^{-2}[K_{\rm cmb}/Jy] \end{aligned} \tag{7.11}$$

Inverted, this is 41 Jy/K_{rj}, which agrees with the APEX telescope website (http://www.apex-telescope.org/telescope/efficiency/).

Point Source Flux at 150 GHz

Now that we can convert between flux units (Jy) and temperature ($K_{\rm cmb}$). We can assume that flux fall (or rises) with frequency raised to some spectral index η. For synchrotron radiation, $\eta \approx -1$ and for dusty thermal sources $\eta \approx 3$.

$$S = S_0 \nu^{\eta} \tag{7.12}$$

Thus to calculate the flux at 150 GHz, given the flux at 90 GHz (or vice versa) we simply take the ratio of the flux at each frequency, then cross multiply:

$$S_{150}/S_{90} = S_0 150^{\eta}/S_0 90^{\eta} = (150/90)^{\eta} \tag{7.13}$$

which implies,

$$S_{90} = S_{150} \times (90/150)^{\eta} \tag{7.14}$$

Example Calculation for a 400 μK cluster (e.g. A2537)

Thus if we want to understand what kind of radio PS that would affect a given cluster. We want a formula which expresses a point source flux limit, $S_{\rm thresh,90}$, as a function of expected SZ decrement. To get this, we first convert the expected and/or measured (by APEX-SZ) decrement convert it to flux units at 150 GHz. Then we multiply it by 2.5%, which is the established threshold for 'significant' point sources.

$$\begin{aligned} S_{\rm thresh150} &= 0.025 \times Dec_{\rm expected}(\mu K_{\rm cmb}) \times 10^{-}6 \times G \\ &= 0.025 \times 32.1 \times 10^{-}6 \times Dec_{\rm expected} = 8.03 \times 10^{-7} \times Dec_{\rm expected}[Jy] \end{aligned} \tag{7.15}$$

$$S_{\rm thresh150} = 8.03 \times 10^{-7} \times Dec_{\rm expected}[Jy] \tag{7.16}$$

A cluster with a 400 $uK_{\rm cmb}$ decrement would have 2.5% flux threshold of $3.21 \times 10^{-}4$ Jy. In other words a point source emitting 0.32 mJy at 150 GHz, could cancel 2.5% of the decrement. Then we would consider what kind of point source this would be at 90 GHz by scaling this flux down to 90 GHz.

$$S_{\rm thresh90} = S_{\rm thresh150} \times (90/150)^{\eta} = 3.2 \times 10^{-}4 \times (90/150)^{-}1 = 0.53 mJY \tag{7.17}$$

$$S_{\rm thresh230} = S_{\rm thresh150} \times (230/150)^{\eta} = 3.2 \times 10^{-}4 \times (230/150)^{3} = 1.15 mJY \tag{7.18}$$

This implies that a 0.53 mJY synchrotron radio point source at 90 GHz or a 1.15 mJY source at 230 GHz would cancel a 10 μK_{cmb} decrement at 150 GHz.

7.2 Detailed Bolometer Comparisons

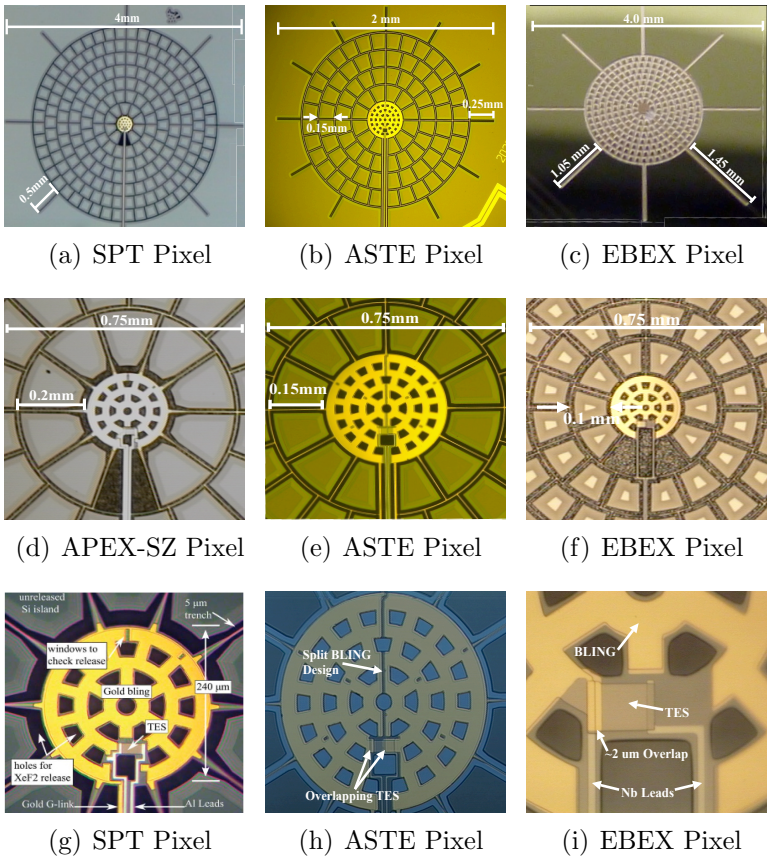

(a) SPT Pixel (b) ASTE Pixel (c) EBEX Pixel

(d) APEX-SZ Pixel (e) ASTE Pixel (f) EBEX Pixel

(g) SPT Pixel (h) ASTE Pixel (i) EBEX Pixel

Figure 7.1: (Color Online) Photographs of SPT, ASTE, and EBEX spider-web TES highlighting the differences in the web grid spacing (a-c), BLING and TES coupling (d-f), and LSN support legs (g-i) for each design. In the EBEX and ASTE designs the grid spacings are 0.1mm and 0.15mm compared to a grid spacing of 0.2 mm used by APEX-SZ and SPT. The APEX-SZ and SPT designs have eight 0.5mm long legs, seven of which are 6 µm and one which is 28 µm wide. The ASTE design has 14 0.25mm long legs, twelve of which are 6µm wide, two of which are 11 µm wide, and one of which is 18µm wide. The EBEX 150 GHz design has seven 1.05mm long, 6µm wide legs and one 1.5mm long, 17µm wide leg. The original APEX-SZ and SPT designs had no overlap between the BLING and the TES, EBEX has the gold from the Au Web, which also serves as part of its BLING, overlap the TES by ∼2 µm on one side, and ASTE has the BLING overlap the TES by ∼2 µm on both sides.

7.3 Antenna Coupled Transition Edge Sensor Bolometers

Although it is not the focus of this work, many of the upcoming CMB experiment employ antenna coupled bolometers (in lieu of spider-web coupled bolometer), which have the advantage of being able to sense multiple frequencies in a single spatial pixel [6, 58, 59, 81]. Typically speaking two orthogonal antennas are placed at the center of the pixel. The incoming radiation excites the electromagnetic modes of the antenna a feeds this power to a micro strip line, which has a band pass filter which defines the frequency response, and is terminated on a resistor which is in tight thermal contact with the TES, which senses the power. This technology is used by all of the CMB polarization experiments except for EBEX. This technology saves precious cryogenic space and allows experiments to observe the cosmos with many thousands of background limited bolometers [11, 85].

The next generation of CMB-pol experiments with support from UC Berkeley will deploy Sinuous Antenna Multi-chroic Pixels (SAMPs) developed in the thesis work of Aritoki Suzuki [81]. POLARBEAR2 plans to deploy di-chroic SAMP arrays at 90 and 150 GHz , while SPT-3G and EBEX6K plan to deploy tri-chroic SAMP arrays at 90, 150, and 220 GHz. A photograph of a sinuous antenna coupled bolometer is shown in Figure 7.2.

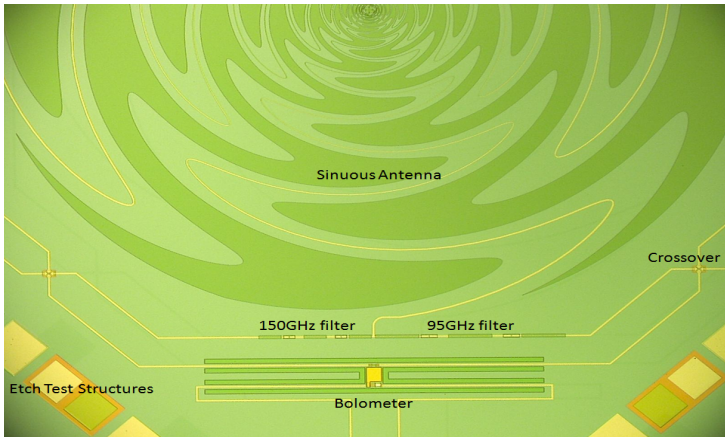

Figure 7.2: A photograph of a sinuous antenna bolometer showing the antenna, band-defining filters, transmission lines, and bolometer.

7.4 Photon Statistics Calculations

7.4.1 Expected Photon Occupation Number

To understand the optical loading we consider the common statistical treatment of photons. A photon at with frequency ν will have an energy equal to $E = h\nu$,

where h is PLANCK's constant. Consider a system of photons with a frequency ν in thermal equilibrium with a bath temperature, T. We can use the partition function of this system to compute the average occupation number n_ν of a photons, which allows us to compute the total energy of the system.

The calculation goes as follows. We start by considering all of the possible energy levels that are present in this system. At this point will will consider only a single polarization for the photons and will not make any adjustments for detector illumination. The system has energy levels (states) defined by the number of photons, n=0, 1, 2.... The energy of each available state (i.e. having n photons) is simply given by $e_n = nh\nu$. This allows straight forward evaluation of the partition function, Z, as shown in Equation 7.19[2], k_b is Boltzmann's Constant.

$$Z = \sum_n e^{(-e_n/k_\mathrm{b}T)} = \sum_n e^{(-nh\nu/k_\mathrm{b}T)} = \sum_n [e^{(-h\nu/k_\mathrm{b}T)}]^n \tag{7.19a}$$

$$Z = \frac{1}{1 - e^{(-h\nu/k_\mathrm{b}T)}} \tag{7.19b}$$

This allows us to compute the 'occupancy' of this mode (frequency) at temperature T (i.e. statistically speaking how many photons do we expect to find with that frequency?). We can write the probability, $P(n)$, that the system contains n photons by taking the ratio of the Boltzmann factor for n photons, $e^{(-nh\nu/k_\mathrm{b}T)}$, to the partition function, Z.[3] The probability that the system has n photons is given by Equation 7.20.

$$\mathscr{P}(n) = e^{-nh\nu/k_\mathrm{b}T}/Z \tag{7.20}$$

We then calculate the average number of photons in that mode by summing overall the possible number of photons multiplied by the n photons. We also calculate the average number squared of photons in the same way (see Equations 7.21 and 7.22).

[2]We recognize the right most term in Equation 7.19a as a geometric power series with $r = e^{(-h\nu/k_\mathrm{b}T)} < 1$. $\sum_n^\infty r^n = 1/(1-r)$ when $r < 1$.

[3]This is a standard way of calculating the probability that a system is in some state and is covered in many Statistical and Thermal textbooks.

$$\langle n_\nu \rangle \equiv \sum_n n\mathscr{P}(n) = \sum_n \frac{1}{Z} n e^{-nh\nu/k_\mathrm{b}T}, \chi \equiv h\nu/k_\mathrm{b}T$$

$$= \frac{1}{Z}\sum_n -\frac{d}{d\chi}e^{-n\chi}$$

$$= -\frac{1}{Z}\frac{d}{d\chi}\sum_n e^{-n\chi} = -\frac{1}{Z}\frac{dZ}{d\chi} = -\frac{1}{Z}\frac{d}{d\chi}[\frac{1}{1-e^{(-\chi)}}] \tag{7.21}$$

$$= -\frac{1}{Z}\frac{-e^{(-\chi)}}{[1-e^{(-\chi)}]^2} = \frac{1}{Z}Z^2 e^{(-\chi)} = Ze^{(-\chi)} = \frac{e^{(-\chi)}}{1-e^{(-\chi)}} = \frac{1}{e^{(\chi)}+1}$$

$$\langle n_\nu \rangle = \frac{1}{e^{(h\nu/k_\mathrm{b}T)}-1}$$

$$\langle n_\nu^2 \rangle \equiv \sum_n n^2 P(n) = \sum_n \frac{1}{Z} n^2 e^{-nh\nu/k_\mathrm{b}T}, \chi \equiv h\nu/k_\mathrm{b}T$$

$$= -\frac{1}{Z}\sum_n \frac{d^2}{d\chi^2}e^{-n\chi}$$

$$= \frac{1}{Z}\frac{d^2}{d\chi^2}\sum_n e^{n\chi} = -\frac{1}{Z}\frac{d^2 Z}{d\chi^2} = -\frac{1}{Z}\frac{d^2}{d\chi^2}[\frac{1}{1-e^{-\chi}}] = \frac{d}{d\chi}[\frac{-e^{(-\chi)}}{1-e^{(-\chi)}}] \tag{7.22}$$

$$= \frac{1}{Z}\frac{e^{-\chi}}{(1-e^{-\chi})^2} + 2\frac{(e^{-\chi})^2}{(1-e^{-\chi})^3} = \frac{1}{Z}[Z^2 e^{-\chi} + 2Z^3(e^{-\chi})^2]$$

$$= \frac{e^{-\chi}}{1-e^{-\chi}} + 2[\frac{e^{-\chi}}{1-e^{-\chi}}]^2 = \frac{1}{e^{\chi}-1} + 2[\frac{1}{e^{\chi}-1}]^2$$

$$= \langle n_\nu \rangle + 2\langle n_\nu \rangle^2$$

Details of Thermal Carrier Noise Calculation

$$NEP_{\mathrm{g}} = \sqrt{4k_{\mathrm{b}}T_{\mathrm{c}}^2\gamma\frac{dP_{\mathrm{sat}}}{dT}} \tag{7.23a}$$

$$= \sqrt{4k_{\mathrm{b}}T_{\mathrm{c}}^2\gamma[k_0\frac{A_{\mathrm{cross}}}{l}T_c^n]} = \sqrt{4k_{\mathrm{b}}T_{\mathrm{bath}}\frac{T_{\mathrm{c}}}{T_{\mathrm{bath}}}\gamma[k_0\frac{A_{\mathrm{cross}}}{l}T_c^{n+1}]} \tag{7.23b}$$

$$= \sqrt{4k_{\mathrm{b}}T_{\mathrm{bath}}}\sqrt{\frac{T_{\mathrm{c}}}{T_{\mathrm{bath}}}\gamma(n+1)[k_0\frac{A_{\mathrm{cross}}}{l(n+1)}T_c^{n+1}]} \tag{7.23c}$$

$$= \sqrt{4k_{\mathrm{b}}T_{\mathrm{bath}}}\sqrt{\frac{T_{\mathrm{c}}}{T_{\mathrm{bath}}}\gamma(n+1)[\frac{P_{\mathrm{sat}}}{1-(\frac{T_{\mathrm{bath}}}{T_{\mathrm{c}}})^{n+1}}]} \tag{7.23d}$$

$$= \sqrt{4k_{\mathrm{b}}T_{\mathrm{bath}}P_{\mathrm{sat}}}\sqrt{(\frac{T_{\mathrm{c}}}{T_{\mathrm{bath}}})[\frac{n+1}{1-(\frac{T_{\mathrm{bath}}}{T_{\mathrm{c}}})^{n+1}}]\gamma} \tag{7.23e}$$

$$= \sqrt{4k_{\mathrm{b}}T_{\mathrm{bath}}P_{\mathrm{sat}}}\sqrt{(\frac{T_{\mathrm{c}}}{T_{\mathrm{bath}}})[\frac{n+1}{1-(\frac{T_{\mathrm{bath}}}{T_{\mathrm{c}}})^{n+1}}]\frac{n+1}{2n+3}\frac{1-(\frac{T_{\mathrm{bath}}}{T_{\mathrm{c}}})^{2n+3}}{1-(\frac{T_{\mathrm{bath}}}{T_{\mathrm{c}}})^{n+1}}} \tag{7.23f}$$

$$= \sqrt{4k_{\mathrm{b}}T_{\mathrm{bath}}P_{\mathrm{sat}}}\sqrt{\frac{(n+1)^2}{2n+3}(\frac{T_{\mathrm{c}}}{T_{\mathrm{bath}}})\frac{1-(\frac{T_{\mathrm{bath}}}{T_{\mathrm{c}}})^{2n+3}}{(1-(\frac{T_{\mathrm{bath}}}{T_{\mathrm{c}}})^{n+1})^2}} \tag{7.23g}$$

$$= \sqrt{4k_{\mathrm{b}}T_{\mathrm{bath}}P_{\mathrm{sat}}}\sqrt{\frac{(n+1)^2}{2n+3}(\frac{T_{\mathrm{bath}}}{T_{\mathrm{c}}})^{-1}(\frac{(\frac{T_{\mathrm{bath}}}{T_{\mathrm{c}}})^{2n+3}}{(\frac{T_{\mathrm{bath}}}{T_{\mathrm{c}}})^{2(n+1)}})\frac{(\frac{T_{\mathrm{c}}}{T_{\mathrm{bath}}})^{2n+3}-1}{((\frac{T_{\mathrm{c}}}{T_{\mathrm{bath}}})^{n+1}-1)^2}} \tag{7.23h}$$

$$= \sqrt{4k_{\mathrm{b}}T_{\mathrm{bath}}P_{\mathrm{sat}}}\sqrt{\frac{(n+1)^2}{2n+3}(\frac{T_{\mathrm{bath}}}{T_{\mathrm{c}}})^{-1+2n+3-2(n+1)}\frac{(\frac{T_{\mathrm{c}}}{T_{\mathrm{bath}}})^{2n+3}-1}{((\frac{T_{\mathrm{c}}}{T_{\mathrm{bath}}})^{n+1}-1)^2}} \tag{7.23i}$$

$$= \sqrt{4k_{\mathrm{b}}T_{\mathrm{bath}}P_{\mathrm{sat}}}\sqrt{\frac{(n+1)^2}{2n+3}\frac{(\frac{T_{\mathrm{c}}}{T_{\mathrm{bath}}})^{2n+3}-1}{((\frac{T_{\mathrm{c}}}{T_{\mathrm{bath}}})^{n+1}-1)^2}} \tag{7.23j}$$

7.5 Useful Cosmological Formulas, Constants, and Orders of Magnitude

Table 7.1: Measures of Distance

Name	Formula(e)	Measure of
Proper Distance	$d_p(t) = a(t)r(x)$	Integration along co-moving coordinates choosing t = now
Luminosity Distance	$d_L(t) \equiv (\frac{L}{4\pi f})^{\frac{1}{2}} = a(t)^{-1}S_k(r) = S_k(r)(1+z)$	Flux of standard candle to get distance
Distance Modulus	$d_L(t) \equiv (\frac{L}{4\pi f})^{\frac{1}{2}} = a(t)^{-1}S_k(r) = S_k(r)(1+z)$	Flux of standard candle to get distance
Angular Diameter Distance	$d_A(t) \equiv l/\theta = \frac{S_k(r)}{(1+z)} = a(t)S_k(r)$	Subtending angle of a standard yardstick
Over Density Radius	$r_n^3 \equiv \frac{M_{rn}}{\frac{4}{3}\pi\rho_c n}$	Radius at which the density exceeds ρ_c by a factor of n

We have replace $x = S_k(r)$, which is a general form for all three universes (closed, flat, open)

$$a(t) = \begin{cases} R_0 sin^{-1}(x/R_0) & : \kappa = +1 \\ x & : \kappa = 0 \\ R_0 sinh^{-1}(x/R_0) & : \kappa = -1 \end{cases}$$

$$x = S_k(r) = \begin{cases} Rsin(r/R) & : \kappa = +1 \\ r & : \kappa = 0 \\ Rsinh(r/R) & : \kappa = -1 \end{cases}$$

Table 7.2: Cluster Modeling Formulas

Name	Spherical-β Model	Arnaud Profile
Electron Density / Pressure	$n_e(r) = n_{e0}(1 + \frac{r^2}{r_c^2})^{-3\beta/2}$	$P_e(r) = \frac{P_0}{(r/r_s)^\gamma[1+(r/r_s)^\alpha]^{(\beta-\gamma)/\alpha}}$
SZ Profile	$\Delta T = \Delta T_0(1 + \frac{\theta^2}{\theta_c^2})^{(1-3\beta)/2}$	—
X-Ray Flux Profile	$S_x = S_0(1 + \frac{\theta^2}{\theta_c^2})^{(1-6\beta)/2}$	—

Table 7.3: Cosmological Parameters

Quantity	Value in MKS	Other Units
Hubble Constant (today)	100h $\frac{km}{sMpc}$	$h = 0.6780 \pm 0.77$
Critical Density, $\rho_{\text{crit}} = \frac{3H^2}{8\pi G}$	$10^{-26}\frac{kg}{m^3}$	$10\ \frac{\text{HydrogenAtoms}}{m^3}$
Baryon Density, $\Omega_b h^2$	0.02214± 0.00024	$\rho_b = \Omega_b \rho_{crit}$
Cold Dark Matter Density, $\Omega_{cdm} h^2$	0.1187 ± 0.0017	$\rho_{cdm} = \Omega_{cdm} \rho_{crit}$
Dark Energy Density, Ω_Λ	0.692 ± 0.010	$\rho_\Lambda = \Omega_\Lambda \rho_{crit}$
Mass Density, Ω_M	0.2559 ± 0.026	$\Omega_M = \Omega_b + \Omega_{cdm}$
σ_8 ($\delta_{\text{rms,mass}}$ on a 8Mpc scale)	0.826 ± 0.012	–
n_s (Scalar spectral index)	0.9608 ± 0.0054	–
τ (Reionization optical depth)	0.092 ± 0.013	–
w (equation of state for Dark Energy)	-1.10 ± 0.14	–
Temperature of CMB (Cosmic Microwave Background)	2.725 K	–
Temperature of CNB (Cosmic Neutrino Background)	1.92 K	–

Table 7.4: Generally Useful Numbers, Constants

Quantity	Value in MKS	Other Units
Hubble Constant (today)	100h $\frac{km}{sMpc}$	$h = 0.710 \pm 0.025$ (WMAP)
Speed of Light	2.9979×10^8 m/s	2.9979×10^8 m/s
PLANCK Constant ($\hbar$)	$1.05 \times 10^{-34}\frac{kgm^2}{s}$	6.582×10^{-16}eVs
Light Year	$9.46 \times 10^{15} m$	0.305 pc
Parsec	$3.0857 \times 10^{16} m$	3.26 light-yr
Solar Mass	$1.98892 \times 10^{30} kg$	$1 M_\odot$

Table 7.5: Useful Orders of Magnitude

Quantity	Value in MKS	Other Units
Age of the Universe	$13.75 \pm 0.011 \times 10^{10}$ yrs	13.75 billion yrs
Size of the Observable Universe	13.75 light yrs	1.3×10^{26}m
End of Greatness Scale	100 Mpc	3×10^{8}light-years
Size of Galaxy Clusters	2-10 Mpc	$6 - 30 \times 10^{22}$m
Virial Radius and r_{500}	$r_{500} \approx 0.5 - 0.67 r_{vir}$	–
Mass of Galaxy Clusters	$\sim 10^{14} - 10^{15} M_{\odot}$	$\sim 10^{44} - 10^{45}$ kg
T_{Cluster} (T_{e^-})	$\sim 10^{7} - 10^{8} K$	$\sim 1 - 10$keV
Angular Extent of Galaxy Clusters	$0.5 - 5'$	–
Number of Galaxies in a Galaxy Cluster	50 - 1000	–
Number of Stars in a Galaxy	$10^{7} - 10^{14}$ Stars	–
Number of Galaxies in Observable Universe	170 billion	–
Critical Density, $\rho_{\text{crit}} = \frac{3H^2}{8\pi G}$	$10^{-26} \frac{kg}{m^3}$	$10 \frac{HydrogenAtoms}{m^3}$
Inflation expansion factor	$\frac{R_{end}}{R_{start}} \geq 10^{28} \approx e^{65}$	$\frac{r_{\text{marble}}(\sim\text{cm})}{<<r_{\text{proton}}(<<\text{fm})}$

Bibliography

[1] K. N. Abazajian et al. "Neutrino Physics from the Cosmic Microwave Background and Large Scale Structure". In: *ArXiv e-prints* (Sept. 2013). arXiv: 1309.5383.

[2] G. E. Addison, G. Hinshaw, and M. Halpern. "Cosmological constraints from baryon acoustic oscillations and clustering of large-scale structure". In: *mnras* 436 (Dec. 2013), pp. 1674–1683. DOI: 10.1093/mnras/stt1687. arXiv: 1304.6984 [astro-ph.CO].

[3] P. A. R. Ade et al. "A review of metal mesh filters". In: Society of Photo-Optical Instrumentation Engineers (SPIE) Conference Series 6275 (July 2006). DOI: 10.1117/12.673162.

[4] P. A. R. Ade et al. "Detection of B-Mode Polarization at Degree Angular Scales by BICEP2". In: *Physical Review Letters* 112.24, 241101 (June 2014), p. 241101. DOI: 10.1103/PhysRevLett.112.241101. arXiv: 1403.3985.

[5] P.A.R. Ade et al. "PLANCK 2013 results. I. Overview of products and scientific results". In: (2013). DOI: 10.1051/0004-6361/201321529. arXiv: 1303.5062 [astro-ph.CO].

[6] K. S. Arnold. "Design and Deployment of the POLARBEAR Cosmic Microwave Background Polarization Experiment". PhD thesis. University of California, Berkeley, 2010.

[7] F. Aubin. "Detector readout electronics for EBEX: a balloon-borne cosmic microwave background polarimeter". PhD thesis. McGill University, 2014.

[8] J.E. Austermann et al. "SPTpol: an instrument for CMB polarization measurements with the South Pole Telescope". In: *Proc.SPIE Int.Soc.Opt.Eng.* 8452 (2012), 84520E. arXiv: 1210.4970 [astro-ph.IM].

[9] K. Basu et al. "Non-parametric modeling of the intra-cluster gas using APEX-SZ bolometer imaging data". In: *AAP* 519, A29 (Sept. 2010), A29. DOI: 10.1051/0004-6361/200913334. arXiv: 0911.3905 [astro-ph.CO].

[10] A.N. Bender et al. "Galaxy cluster scaling relations measured with APEX-SZ". In: (2014). arXiv: 1404.7103 [astro-ph.CO].

[11] B. A. Benson et al. "SPT-3G: A Next-Generation Cosmic Microwave Background Polarization Experiment on the South Pole Telescope". In: *ArXiv e-prints* (July 2014). arXiv: 1407.2973 [astro-ph.IM].

[12] BICEP2 Collaboration et al. "BICEP2 II: Experiment and Three-Year Data Set". In: *ArXiv e-prints* (Mar. 2014). arXiv: 1403.4302.

[13] F. Brümmer, V. Domcke, and V. Sanz. "GUT-scale inflation with sizeable tensor modes". In: *jcap* 8, 066 (Aug. 2014), p. 66. DOI: 10.1088/1475-7516/2014/08/066. arXiv: 1405.4868 [hep-ph].

[14] E. Calabrese et al. "Precision epoch of reionization studies with next-generation CMB experiments". In: *jcap* 8, 010 (Aug. 2014), p. 10. DOI: 10.1088/1475-7516/2014/08/010. arXiv: 1406.4794.

[15] P.J.B. Clarricoats and A.D. Olver. *Corrugated Horns for Microwave Antennas*. IEE electromagnetic waves series. P. Peregrinus, 1984. ISBN: 9780863410031. URL: http://books.google.com/books?id=Ddl2qyn7qW8C.

[16] M. Cortes, A. R. Liddle, and D. Parkinson. "Tensors, BICEP2, prior dependence, and dust". In: *ArXiv e-prints* (Sept. 2014). arXiv: 1409.6530.

[17] Sudeep Das et al. "The Atacama Cosmology Telescope: temperature and gravitational lensing power spectrum measurements from three seasons of data". In: *JCAP* 1404 (2014), p. 014. DOI: 10.1088/1475-7516/2014/04/014. arXiv: 1301.1037 [astro-ph.CO].

[18] M. Dobbs, E. Bissonnette, and H. Spieler. "Digital Frequency Domain Multiplexer for Millimeter-Wavelength Telescopes". In: *IEEE Transactions on Nuclear Science* 55 (2008), pp. 21–26. DOI: 10.1109/TNS.2007.911601. arXiv: 0708.2762 [physics.ins-det].

[19] Scott Dodelson. *Modern Cosmology*. Academic Press. ISBN: 9780122191411. Academic Press.

[20] R. Durrer. "The theory of CMB anisotropies". In: *Journal of Physical Studies* 5 (2001), pp. 177–215. eprint: astro-ph/0109522.

[21] D. P. Finkbeiner, M. Davis, and D. J. Schlegel. "Extrapolation of Galactic Dust Emission at 100 Microns to Cosmic Microwave Background Radiation Frequencies Using FIRAS". In: *apj* 524 (Oct. 1999), pp. 867–886. DOI: 10.1086/307852. eprint: astro-ph/9905128.

[22] D. J. Fixsen et al. "The Cosmic Microwave Background Spectrum from the Full COBE FIRAS Data Set". In: *apj* 473 (Dec. 1996), p. 576. DOI: 10.1086/178173. eprint: astro-ph/9605054.

[23] E. M. George et al. “A measurement of secondary cosmic microwave background anisotropies from the 2500-square-degree SPT-SZ survey”. In: *ArXiv e-prints* (Aug. 2014). arXiv: 1408.3161.

[24] E.M. George et al. “Performance and on-sky optical characterization of the SPTpol instrument”. In: *Proc.SPIE Int.Soc.Opt.Eng.* 8452 (2012), 84521F. DOI: 10.1117/12.925586. arXiv: 1210.4971 [astro-ph.IM].

[25] J. M. Gildemeister, Adrian T. Lee, and P. L. Richards. “A fully lithographed voltage-biased superconducting spiderweb bolometer”. In: *Applied Physics Letters* 74.6 (1999), pp. 868–870. DOI: http://dx.doi.org/10.1063/1.123393. URL: http://scitation.aip.org/content/aip/journal/apl/74/6/10.1063/1.123393.

[26] Jan Gildemeister. “Voltage-Biased Superconducting Bolometer for Infrared and mm-Waves”. PhD thesis. University of California, Berkeley, Dec. 2005.

[27] Alan H. Guth. “Inflationary universe: A possible solution to the horizon and flatness problems”. In: *Phys. Rev. D* 23 (2 Jan. 1981), pp. 347–356. DOI: 10.1103/PhysRevD.23.347. URL: http://link.aps.org/doi/10.1103/PhysRevD.23.347.

[28] Z. Haiman, J. J. Mohr, and G. P. Holder. “Constraints on Cosmological Parameters from Future Galaxy Cluster Surveys”. In: *ApJ* 553 (June 2001), pp. 545–561. DOI: 10.1086/320939. eprint: astro-ph/0002336.

[29] E. E. Haller, K. M. Itoh, and J. W. Beeman. “Neutron Transmutation Depot (NTD) Germanium Thermistors for Submillimetre Bolometer Applications”. In: *Submillimetre and Far-Infrared Space Instrumentation*. Ed. by E. J. Rolfe and G. Pilbratt. Vol. 388. ESA Special Publication. Dec. 1996, p. 115.

[30] N.W. Halverson et al. “Sunyaev-Zel’dovich Effect Observations of the Bullet Cluster (1E 0657-56) with APEX-SZ”. In: *Astrophys.J.* 701 (2009), pp. 42–51. DOI: 10.1088/0004-637X/701/1/42. arXiv: 0807.4208 [astro-ph].

[31] D. Hanson et al. “Detection of B-mode Polarization in the Cosmic Microwave Background with Data from the South Pole Telescope”. In: *Phys.Rev.Lett.* 111.14 (2013), p. 141301. DOI: 10.1103/PhysRevLett.111.141301. arXiv: 1307.5830 [astro-ph.CO].

[32] G. Hinshaw et al. “Nine-year Wilkinson Microwave Anisotropy Probe (WMAP) Observations: Cosmological Parameter Results”. In: *ApJ* 208, 19 (Oct. 2013), p. 19. DOI: 10.1088/0067-0049/208/2/19. arXiv: 1212.5226 [astro-ph.CO].

[33] A. Hirota et al. “Development of TES Bolometer Camera for ASTE Telescope: II. Performance of Detector Arrays”. In: *Applied Superconductivity, IEEE Transactions on* 23.3 (June 2013), pp. 2101305–2101305. ISSN: 1051-8223. DOI: 10.1109/TASC.2013.2247791.

[34] Johannes Hubmayr et al. “Design and characterization of TES bolometers and SQUID readout electronics for a balloon-borne application”. In: (2009). arXiv: 0908.1997 [astro-ph.IM].

[35] K.D. Irwin and G.C. Hilton. “Transition-Edge Sensors”. English. In: *Cryogenic Particle Detection*. Ed. by Christian Enss. Vol. 99. Topics in Applied Physics. Springer Berlin Heidelberg, 2005, pp. 63–150. ISBN: 978-3-540-20113-7. DOI: 10.1007/10933596_3. URL: http://dx.doi.org/10.1007/10933596_3.

[36] B. R. Johnson et al. “MAXIPOL: a balloon-borne experiment for measuring the polarization anisotropy of the cosmic microwave background radiation”. In: 47 (Dec. 2003), pp. 1067–1075. DOI: 10.1016/j.newar.2003.09.034. eprint: astro-ph/0308259.

[37] Nick Kaiser. “Evolution and clustering of rich clusters”. In: *Monthly Notices of the Royal Astronomical Society* 222.2 (1986), pp. 323–345. DOI: 10.1093/mnras/222.2.323. URL: http://mnras.oxfordjournals.org/content/222/2/323.abstract.

[38] C. Kittel and H. Kroemer. *Thermal Physics*. W. H. Freeman, 1980. ISBN: 9780716710882. URL: http://books.google.com/books?id=c0R79nyOoNMC.

[39] JamesW. Lamb. “Miscellaneous data on materials for millimetre and submillimetre optics”. English. In: *International Journal of Infrared and Millimeter Waves* 17.12 (1996), pp. 1997–2034. ISSN: 0195-9271. DOI: 10.1007/BF02069487. URL: http://dx.doi.org/10.1007/BF02069487.

[40] A. Lange et al. “The BOOMERANG experiment”. English. In: *Space Science Reviews* 74.1-2 (1995), pp. 145–150. ISSN: 0038-6308. DOI: 10.1007/BF00751263. URL: http://dx.doi.org/10.1007/BF00751263.

[41] S.P. Langley. *The "bolometer"*. The Society, 1881. URL: http://books.google.com/books?id=W%5C_03AQAAIAAJ.

[42] M. Lattanzi, N. Carlevaro, and G. Montani. “Gravitational instability of the primordial plasma: Anisotropic evolution of structure seeds”. In: *Physics Letters B* 718 (Dec. 2012), pp. 255–264. DOI: 10.1016/j.physletb.2012.10.067. arXiv: 1107.3394 [astro-ph.CO].

[43] Adrian T. Lee et al. “A superconducting bolometer with strong electrothermal feedback”. In: *Applied Physics Letters* 69.12 (1996), pp. 1801–1803. DOI: 10.1063/1.117491. URL: http://scitation.aip.org/content/aip/journal/apl/69/12/10.1063/1.117491.

[44] A.T. Lee et al. “MAXIMA: An Experiment to measure temperature anisotropy in the cosmic microwave background”. In: *AIP Conf.Proc.* 476 (1999), pp. 224–236. arXiv: astro-ph/9903249 [astro-ph].

[45] A. Linde. “Inflationary Cosmology”. In: *Inflationary Cosmology*. Ed. by M. Lemoine, J. Martin, and P. Peter. Vol. 738. Lecture Notes in Physics, Berlin Springer Verlag. 2008, p. 1. DOI: 10.1007/978-3-540-74353-8_1. arXiv: 0705.0164 [hep-th].

[46] K. D. Lozanov and M. A. Amin. “The end of inflation, oscillons and matter-antimatter asymmetry”. In: *ArXiv e-prints* (Aug. 2014). arXiv: 1408.1811 [hep-ph].

[47] K. MacDermid. “Development and Performance of the Detectors and Readout of the EBEX Balloon-Borne CMB Polarimeter”. PhD thesis. McGill University, 2014.

[48] K. MacDermid et al. “The performance of the bolometer array and readout system during the 2012/2013 flight of the E and B experiment (EBEX)”. In: *ArXiv e-prints* (July 2014). arXiv: 1407.6894 [astro-ph.IM].

[49] John C. Mather. “Bolometer noise: nonequilibrium theory”. In: *Appl. Opt.* 21.6 (Mar. 1982), pp. 1125–1129. DOI: 10.1364/AO.21.001125. URL: http://ao.osa.org/abstract.cfm?URI=ao-21-6-1125.

[50] P. D. Mauskopf et al. “Composite infrared bolometers with Si3N4 micromesh absorbers”. In: *Appl. Opt.* 36.4 (Feb. 1997), pp. 765–771. DOI: 10.1364/AO.36.000765. URL: http://ao.osa.org/abstract.cfm?URI=ao-36-4-765.

[51] Jared Mehl. “Cosmological Studies Of The Sunyaev-Zel’dovich Effect With The APEX-SZ Instrument”. PhD thesis. University of California, Berkeley, May 2009.

[52] D. E. Morrissey and M. J. Ramsey-Musolf. “Electroweak baryogenesis”. In: *New Journal of Physics* 14.12, 125003 (Dec. 2012), p. 125003. DOI: 10.1088/1367-2630/14/12/125003. arXiv: 1206.2942 [hep-ph].

[53] M. J. Mortonson and U. Seljak. “A joint analysis of PLANCK and BICEP2 B modes including dust polarization uncertainty”. In: *ArXiv e-prints* (May 2014). arXiv: 1405.5857.

[54] D. O. Muhleman and G. L. Berge. "Observations of Mars, Uranus, Neptune, Io, Europa, Ganymede, and Callisto at a wavelength of 2.66 MM". In: *icarus* 92 (Aug. 1991), pp. 263–272. DOI: 10.1016/0019-1035(91)90050-4.

[55] M. Myers. "Antenna-coupled Superconducting Bolometers for Observations of the Cosmic Microwave Background Polarization". PhD thesis. University of California, Berkeley, 2010.

[56] S. Nojiri, S. D. Odintsov, and H. Stefanic. "Transition from a matter-dominated era to a dark energy universe". In: *prd* 74.8, 086009 (Oct. 2006), p. 086009. DOI: 10.1103/PhysRevD.74.086009. eprint: hep-th/0608168.

[57] M. Nord et al. "Multi-frequency imaging of the galaxy cluster Abell 2163 using the Sunyaev-Zel'dovich effect". In: *AAP* 506 (Nov. 2009), pp. 623–636. DOI: 10.1051/0004-6361/200911746. arXiv: 0902.2131 [astro-ph.CO].

[58] R. O'Brient. "Development and Performance of the Detectors and Readout of the EBEX Balloon-Borne CMB Polarimeter". PhD thesis. McGill University, 2014.

[59] R. O'Brient et al. "A dual-polarized broadband planar antenna and channelizing filter bank for millimeter wavelengths". In: *Applied Physics Letters* 102.6, 063506 (Feb. 2013), p. 063506. DOI: 10.1063/1.4791692. arXiv: 1302.0325 [astro-ph.IM].

[60] T. Oshima et al. "Development of TES Bolometer Camera for ASTE Telescope: I. Bolometer Design". In: *Applied Superconductivity, IEEE Transactions on* 23.3 (June 2013), pp. 2101004–2101004. ISSN: 1051-8223. DOI: 10.1109/TASC.2013.2240751.

[61] J. R. Pardo, J. Cernicharo, and E. Serabyn. "Atmospheric transmission at microwaves (ATM): an improved model for millimeter/submillimeter applications". In: *IEEE Transactions on Antennas and Propagation* 49 (Dec. 2001), pp. 1683–1694. DOI: 10.1109/8.982447.

[62] A. A. Penzias and R. W. Wilson. "A Measurement of Excess Antenna Temperature at 4080 Mc/s." In: *apj* 142 (July 1965), pp. 419–421. DOI: 10.1086/148307.

[63] S. Perlmutter et al. "Cosmology From Type IA Supernovae: Measurements, Calibration Techniques, and Implications". In: *American Astronomical Society Meeting Abstracts*. Vol. 29. Bulletin of the American Astronomical Society. Dec. 1997, p. 1351. eprint: astro-ph/9812473.

[64] T. Plagge et al. "Sunyaev-Zel'dovich Cluster Profiles Measured with the South Pole Telescope". In: *ApJ* 716 (June 2010), pp. 1118–1135. DOI: 10.1088/0004-637X/716/2/1118. arXiv: 0911.2444 [astro-ph.CO].

[65] PLANCK Collaboration et al. "PLANCK 2013 results. VI. High Frequency Instrument data processing". In: *ArXiv e-prints* (Mar. 2013). arXiv: 1303.5067.

[66] PLANCK Collaboration et al. "PLANCK intermediate results. XIX. An overview of the polarized thermal emission from Galactic dust". In: *ArXiv e-prints* (May 2014). arXiv: 1405.0871.

[67] PLANCK Collaboration et al. "PLANCK intermediate results. XXX. The angular power spectrum of polarized dust emission at intermediate and high Galactic latitudes". In: *ArXiv e-prints* (Sept. 2014). arXiv: 1409.5738.

[68] S. J. E. Radford. "Observing Conditions for Submillimeter Astronomy". In: *Revista Mexicana de Astronomia y Astrofisica Conference Series*. Vol. 41. Nov. 2011, pp. 87–90. arXiv: 1107.5633 [astro-ph.IM].

[69] C. L. Reichardt et al. "Constraints on the High-ell Power Spectrum of Millimeter-Wave Anisotropies from APEX-SZ". In: *ApJ* 701 (Aug. 2009), pp. 1958–1964. DOI: 10.1088/0004-637X/701/2/1958. arXiv: 0904.3939 [astro-ph.CO].

[70] B. Reichborn-Kjennerud. "Building and Flying the E and B Experiment to Measure the Polarization of the Cosmic Microwave Background". PhD thesis. Columbia University, 2010.

[71] B. Reichborn-Kjennerud et al. "EBEX: a balloon-borne CMB polarization experiment". In: *Society of Photo-Optical Instrumentation Engineers (SPIE) Conference Series*. Vol. 7741. Society of Photo-Optical Instrumentation Engineers (SPIE) Conference Series. July 2010. DOI: 10.1117/12.857138. arXiv: 1007.3672 [astro-ph.CO].

[72] P. L. Richards. "Bolometers for infrared and millimeter waves". In: *Journal of Applied Physics* 76 (July 1994), pp. 1–24. DOI: 10.1063/1.357128.

[73] D. J. Rudy et al. "Mars - VLA observations of the northern hemisphere and the north polar region at wavelengths of 2 and 6 CM". In: *icarus* 71 (July 1987), pp. 159–177. DOI: 10.1016/0019-1035(87)90170-9.

[74] John E. Ruhl et al. "The South Pole Telescope". In: *Proc.SPIE Int.Soc.Opt.Eng.* 5498 (2004), p. 11. DOI: 10.1117/12.552473. arXiv: astro-ph/0411122 [astro-ph].

[75] I. S. Sagiv. "The EBEX Cryostat and Supporting Electronics". PhD thesis. University of Minnesota, 2011.

[76] J. Sayers et al. "Sunyaev-Zel'dovich-measured Pressure Profiles from the Bolocam X-Ray/SZ Galaxy Cluster Sample". In: *ApJ* 768, 177 (May 2013), p. 177. DOI: 10.1088/0004-637X/768/2/177. arXiv: 1211.1632 [astro-ph.CO].

[77] D. Schwan et al. "Millimeter-wave bolometer array receiver for the Atacama pathfinder experiment Sunyaev-Zel'dovich (APEX-SZ) instrument". In: *Rev.Sci.Instrum.* 82 (2011), p. 091301. DOI: 10.1063/1.3637460. arXiv: 1008.0342 [astro-ph.IM].

[78] E. Senaha. "Overview of Electroweak Baryogenesis". In: *ArXiv e-prints* (May 2013). arXiv: 1305.1563 [hep-ph].

[79] E. Shirokoff. "The South Pole Telescope bolometer array and the measurement of secondary Cosmic Microwave Background anisotropy at small angular scales". PhD thesis. University of California, Berkeley, 2011.

[80] R. A. Sunyaev and Y. B. Zeldovich. "Small-Scale Fluctuations of Relic Radiation". In: *apss* 7 (Apr. 1970), pp. 3–19. DOI: 10.1007/BF00653471.

[81] Aritoki Suzuki. "Multichroic Bolometeric Detector Architecture for Cosmic Microwave Background Polarimetry Experiments". PhD thesis. University of California, Berkeley, Dec. 2013.

[82] D. S. Swetz et al. "Overview of the Atacama Cosmology Telescope: Receiver, Instrumentation, and Telescope Systems". In: *ApJ* 194, 41 (June 2011), p. 41. DOI: 10.1088/0067-0049/194/2/41. arXiv: 1007.0290 [astro-ph.IM].

[83] The POLARBEAR Collaboration et al. "A Measurement of the Cosmic Microwave Background B-Mode Polarization Power Spectrum at Sub-Degree Scales with POLARBEAR". In: *ArXiv e-prints* (Mar. 2014). arXiv: 1403.2369 [astro-ph.CO].

[84] M. Tinkham. *Introduction to Superconductivity: Second Edition*. Dover Books on Physics. Dover Publications, 2004. ISBN: 9780486435039. URL: http://books.google.com/books?id=k6AO9nRYbioC.

[85] Takayuki Tomaru et al. *The POLARBEAR-2 experiment*. 2012. DOI: 10.1117/12.926158. URL: http://dx.doi.org/10.1117/12.926158.

[86] J. E. Vaillancourt. "Polarized Emission from Interstellar Dust". In: *EAS Publications Series*. Ed. by M.-A. Miville-Deschênes and F. Boulanger. Vol. 23. EAS Publications Series. 2007, pp. 147–164. DOI: 10.1051/eas:2007010. eprint: astro-ph/0609033.

[87] J. D. Vieira et al. "Extragalactic Millimeter-wave Sources in South Pole Telescope Survey Data: Source Counts, Catalog, and Statistics for an 87 Square-degree Field". In: *ApJ* 719 (Aug. 2010), pp. 763–783. DOI: 10.1088/0004-637X/719/1/763. arXiv: 0912.2338 [astro-ph.CO].

[88] J. Weller, R. A. Battye, and R. Kneissl. "Constraining Dark Energy with Sunyaev-Zel'dovich Cluster Surveys". In: *Physical Review Letters* 88.23, 231301 (June 2002), p. 231301. DOI: 10.1103/PhysRevLett.88.231301. eprint: astro-ph/0110353.

[89] B. Westbrook et al. "Design Evolution of the Spiderweb TES Bolometer for Cosmology Applications". English. In: *Journal of Low Temperature Physics* 167.5-6 (2012), pp. 885–891. ISSN: 0022-2291. DOI: 10.1007/s10909-012-0528-4. URL: http://dx.doi.org/10.1007/s10909-012-0528-4.

[90] B. Westbrook et al. "Further Optimization of the APEX-SZ TES Bolometer Array". In: *American Institute of Physics Conference Series*. Ed. by B. Young, B. Cabrera, and A. Miller. Vol. 1185. American Institute of Physics Conference Series. Dec. 2009, pp. 363–366. DOI: 10.1063/1.3292353.

[91] S. Zaroubi. "The Epoch of Reionization". In: *Astrophysics and Space Science Library*. Ed. by T. Wiklind, B. Mobasher, and V. Bromm. Vol. 396. Astrophysics and Space Science Library. 2013, p. 45. DOI: 10.1007/978-3-642-32362-1_2. arXiv: 1206.0267 [astro-ph.CO].